General Disclaimer

One or more of the Following Statements may affect this Document

- This document has been reproduced from the best copy furnished by the organizational source. It is being released in the interest of making available as much information as possible.

- This document may contain data, which exceeds the sheet parameters. It was furnished in this condition by the organizational source and is the best copy available.

- This document may contain tone-on-tone or color graphs, charts and/or pictures, which have been reproduced in black and white.

- This document is paginated as submitted by the original source.

- Portions of this document are not fully legible due to the historical nature of some of the material. However, it is the best reproduction available from the original submission.

CR-151122

APOLLO-SOYUZ DOPPLER-TRACKING EXPERIMENT MA-089

Final Report
Contract NAS9-13837

by

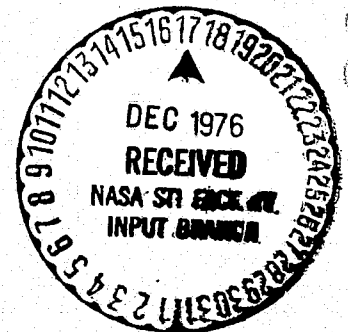Staff, Smithsonian Astrophysical Observatory

Princial Investigator: G. C. Weiffenbach
Coinvestigators: M. D. Grossi
P. W. Shores

October 1976

Smithsonian Institution
Astrophysical Observatory
Cambridge, Massachusetts   02138

DEC 1976
RECEIVED
NASA STI
INPUT

The Smithsonian Astrophysical Observatory
and the Harvard College Observatory
are members of the
Center for Astrophysics

APOLLO-SOYUZ DOPPLER-TRACKING EXPERIMENT MA-089

Final Report
Contract NAS9-13837

by

Staff, Smithsonian Astrophysical Observatory

Princial Investigator: G. C. Weiffenbach
Coinvestigators: M. D. Grossi
P. W. Shores

October 1976

TABLE OF CONTENTS

iii

TABLE OF CONTENTS

APOLLO-SOYUZ DOPPLER-TRACKING EXPERIMENT MA-089[*]

by
Staff, Smithsonian Astrophysical Observatory

ABSTRACT

The Doppler-tracking experiment was designed to test the feasibility of improved mapping of the Earth's gravity field by the low-low satellite-to-satellite tracking method and to observe variations in the electron density of the ionosphere between the two spacecraft. Data were taken between 1:01 and 14:37 GMT on July 24, 1975. Baseline data taken earlier, while the docking module was still attached to the command and service module, indicated that the equipment operated satisfactorily.

The ionospheric data contained in the difference between the Doppler signals at the two frequencies are of excellent quality, resulting in valuable satellite-to-satellite observations, never made before, of wave phenomena in the ionosphere. The gravity data were corrupted by an unexpectedly high noise level of as-yet-undetermined origin, with periods greater than 150 seconds, that prevented unambiguous identification of gravity-anomaly signatures.

---

[*]Principal Investigator: G. C. Weiffenbach

Coinvestigators: M. D. Grossi and P. W. Shores

1

1. INTRODUCTION

Interest has recently focused on mass density anomalies with scale sizes of 100 to 700 kilometers in the upper mantle of the Earth. It is likely that these anomalies play an important role in the physics of the mantle and plate tectonics and in the reconstruction of important aspects of the Earth's evolution, such as continental drift. Small-scale anomalies near the surface of the Earth have been studied for many years by surface gravimetry; and large-scale anomalies, greater than 2000 kilometers, have been investigated for almost 20 years by observing artificial-satellite orbit perturbations. The spacecraft-to-spacecraft Doppler Tracking Experiment (MA-089) conducted by the Smithsonian Astrophysical Observatory (SAO) on board the Apollo-Soyuz Test Project (ASTP) mission was designed to determine gravity features having an intermediate horizontal scale of 250 to 1000 kilometers. The ASTP mission was particularly suitable for this experiment because it provided two platforms with a controlled separation within the same orbit at an altitude low enough for enhanced sensitivity to these short-wavelength gravity anomalies.

The experiment consisted of measuring, by means of a phase-coherent dual-frequency, very-high-frequency link, the relative velocity, or Doppler shift, between the docking module (DM) and the command and service module (CSM). Both orbiting at a height of 220 kilometers, these two modules had an initial separation of 310 kilometers, which increased to 430 kilometers by the end of the data take. From their relative-velocity data, localized anomalies in the Earth's

gravitational field should be measured with a threshold sensitivity of better than 0.15 mm/sec^2 (15 milligals). The geometric range rate induced by the ionosphere was removed by the dual-frequency (162- and 324-megahertz) correction.

A secondary goal of the experiment was to measure changes in the integrated electron concentration and other ionospheric properties along a radio path between the CSM and the DM and between the DM and the ground.

Since the time available for our experiment was limited to 12 hours, complete global coverage was not expected to be possible; therefore, our experiment was meant to serve solely as a feasibility demonstration.

2. THEORY

2.1 Measuring the Earth's Gravity Field

The structure of the Earth's gravity field has been of considerable scientific interest for some time because it provides one of the few available clues to the internal distribution of mass in the Earth. The recent development of the plate-tectonics hypothesis has placed added emphasis on the need for information on those particular features in the gravity field that have horizontal wavelengths of 100 to 700 kilometers.

Evidence from studies of seismic-wave propagation shows that the outer portion of the Earth consists of (1) a high-velocity zone, the lithosphere, which generally includes the crust and uppermost mantle, has significant strength, and is some 50 to 80 kilometers thick under the oceans and somewhat thicker under the continents; (2) a low-velocity zone, the asthenosphere, which is a layer of low effective strength on a geologic time scale and extends from the base of the lithosphere to a depth of several hundred kilometers; and (3) the lower remaining portion of the mantle, the mesosphere, which may have strength and is relatively passive in tectonic processes.

The plate-tectonics concept is based on the observation that large blocks or plates of the rigid lithosphere, some thousands of kilometers in horizontal extent, appear to be moving ("floating" on the yielding asthenosphere) with

respect to one another at average long-term rates of the order of 1 to 15 cm/yr (ref. 1). One manifestation of this plate motion is continental drift. Most large earthquakes, volcanic activity, mountain building, and tsunami generation, plus some terrestrial mineral resources, are located at the boundaries of the lithospheric plates. In fact, nearly all large-scale geological and geophysical phenomena occurring on the Earth's surface appear to be intimately related to this global pattern of plate motions. Thus, the subject of plate tectonics is of considerable scientific and practical interest.

However, no satisfactory theory of the mechanism(s) producing plate motion is available. It is very probable that both thermal convection and chemical convection in the asthenosphere are involved in some way, and most current theories include one or both processes. In any event, there is little question that knowledge of the density field in the upper portion of the Earth, to a depth of 700 kilometers or so, would be of considerable importance in determining the basic mechanisms underlying plate motion.

The distribution of mass within the Earth uniquely determines the external gravity field. Hence, measurements of the latter contain information on the density field (although it should be noted that the external field does not define the unique internal mass distribution). As a rough rule of thumb, a density anomaly within the Earth will produce a lateral variation in the external gravity field whose scale is comparable to the depth of the anomaly. Thus, the density field within the upper mantle at depths of the order of 100 to 700 kilometers will generally be reflected in horizontal variations of the gravity field with wavelengths of 100 to 700 kilometers. This suggests that

measurements of intermediate-wavelength (100- to 1000-kilometer) features in the gravity field will be fundamental to advancing our understanding of plate tectonics.

The intermediate-wavelength structure of the Earth's gravity field is of interest for another reason. The surface of the ocean contains topographic signatures of current systems, eddies, storm surges, tsunamis, barometric loading, etc., all of which are of considerable practical importance. There is great interest in developing methods for maintaining frequent surveillance of these phenomena over the world's ocean. One very promising approach is to map the topography of the ocean with satellite-borne radar altimeters. Indeed, the Geos 3 spacecraft, launched by the National Aeronautics and Space Administration (NASA) in April 1975, has such an altimeter.

However, the mean-sea-level surface also contains the topographic imprint of the Earth's gravity field — i.e., the geoid. Geoid undulations must be mapped and removed from the measured ocean topography before it will be possible to identify the signatures of oceanographic parameters uniquely. All the oceanic features listed above have topographic structures with significant lateral components in the range 100 to 1000 kilometers. The estimated geoid accuracy needed for this purpose is 10 centimeters in geoid height.

Measuring the Earth's gravity field has been a continuing occupation of geodesists for many years. The traditional method has been to use gravimeters at fixed locations in land areas and on board ships, submarines, and more

recently, aircraft. This method provides accurate measurements of the detailed structure of the gravity field, particularly on land. However, surface gravimetry has several deficiencies: the cost and time involved in covering large geographic areas (particularly in rough terrain), the reduced accuracy of gravimeters on mobile platforms, and the loss in accuracy of large-scale gravity variations synthesized from gravimeter data.

More recently, the structure of the gravity field has been calculated via orbital dynamics from accurate tracking of artificial satellites. Since satellite orbits are uniquely determined by the forces acting on the satellite and since gravity is by far the dominant force, the gravitational force can be inferred from the observed orbits and an appropriate orbit theory. This orbital-dynamics approach has been used successfully to measure the large-scale structure of the gravity field with considerable accuracy.

However, orbital dynamics is not suitable for obtaining intermediate- or short-wavelength gravity-field features. Specifically, spherical-harmonic terms of degree higher than 20 are impractical, both because of the rapidly increasing complexity of the theory and its computer mechanization and because of the need for larger and larger numbers of satellites in different orbits. Thus, this method is restricted, for practical reasons, to gravity features with horizontal wavelengths greater than 2000 kilometers.

2.2 The Gravity Field from Satellite-to-Satellite Velocity Measurements

There is another method employing artificial satellites that can be used to measure intermediate-sized gravity features. Employed in SAO's Doppler Tracking Experiment, it is based on calculating the gravitational force acting on a spacecraft directly from changes in its measured velocity. This is shown in simplistic form in Figure 1, which pictures a satellite in orbit about the Earth with a density assumed homogeneous except for an excess mass M at some point under the orbit. As the satellite approaches M, the added gravitational force exerted by M will accelerate the satellite. As the satellite moves away from M, the corresponding retarding force will reduce the satellite velocity. By measuring the time history of the velocity variation during the period when the satellite is under the influence of M, the size, position, and magnitude of the mass excess M can be deduced. This was, in fact, the approach used to discover and measure lunar mascons (ref. 2).

Of course, the actual situation for the experiment is more complex, not only because of the Earth's internal mass distribution and its effects on the satellite trajectory, but also because of the fact that the satellite's velocity must be measured from another satellite. A detailed analysis of more realistic cases has been reported by Schwarz (ref. 3). Wolf (ref. 4), Comfort (ref. 5), and Vonbun (ref. 6) have also contributed to the investigation of this method.
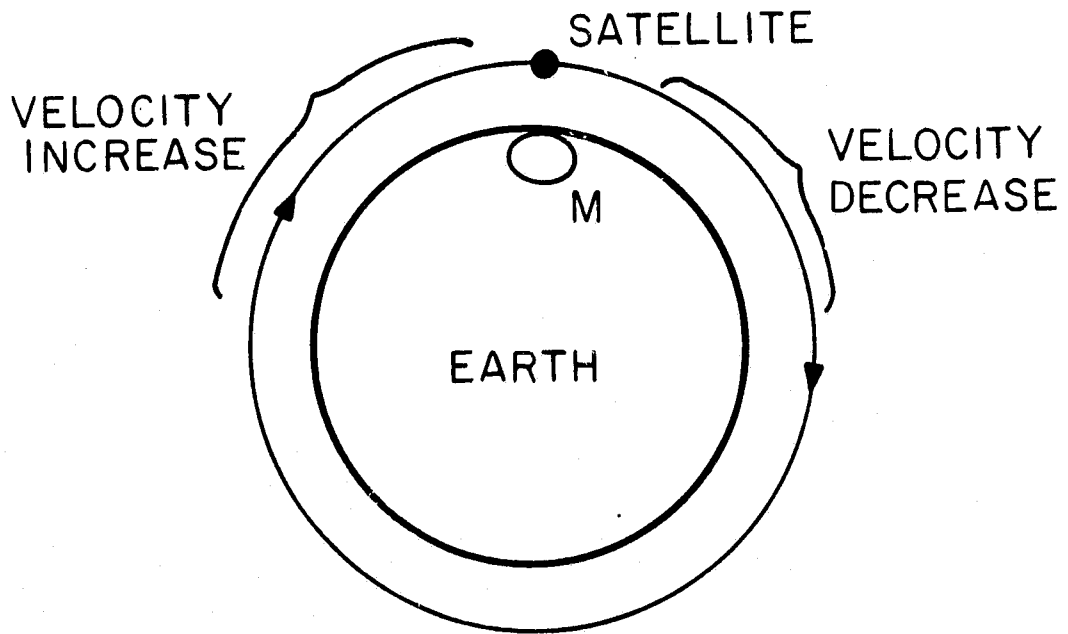
Figure 1. Gravity anomalies and velocity changes.

From surface-gravimeter data for the United States, Schwarz constructed arrays of 1° by 1°, 2° by 2°, and 5° by 5° gravity anomalies and computed the theoretical range-rate variations that would be observed between two spacecraft in orbit over these simulated gravity fields. Orbital altitudes of 200, 300, and 700 kilometers and satellite-to-satellite separations of 200 to 600 kilometers were used in various combinations. Noise was added to the computed range-rate data. Schwarz then inverted the process to determine how accurately the simulated gravity anomalies could be recovered from the computed, noisy, range-rate (Doppler) data.

The results of Schwarz's computer experiment are briefly summarized as follows:

1. The structure of the gravity field can be determined from measurements of the variations in range rate between two spacecraft in the same nominal orbit.

2. The lateral scale of the shortest wavelength gravity feature that can be so recovered is approximately equal to the orbital altitude.

3. The accuracy of the recovered gravity anomalies is of the order of 0.1 mm/sec (10 milligals), for an accuracy of 0.5 mm/sec (1 standard deviation) in range rate between spacecraft, where each measurement is averaged over 16 to 32 seconds.

4. The ephemerides of the two spacecraft need not be determined to high accuracy, orbital errors as large as 1000 meters having little effect on the solutions.

Schwarz's computer experiments suggest rather convincingly that the ASTP Doppler Tracking Experiment should produce accurate determinations of gravity anomalies with horizontal wavelengths in the range 300 to 1000 kilometers over those geographic regions where measurements are obtained. The lunar-mascon experiment confirms this conclusion even though the geometry was somewhat different, one of the "spacecraft" terminals being located on the Earth.

Useful data can be obtained when the spacecraft are within line of sight of each other, when the line between them lies above the troposphere, and when their separation is greater than 200 kilometers.

It is important to note that gravity-field information is obtained only for those particular geographic regions where the Doppler measurements are made. The scientific usefulness of the experiment thus depends on the geographic coverage.

The accelerations produced by atmospheric drag and radiation pressure on the spacecraft contribute to the measured range rates and thus constitute systematic errors in the determination of the gravity field.

The acceleration caused by radiation pressure was computed for solar flux incident on the side of the spacecraft. In this case, the area-to-mass ratio is about 0.02 cm^2/g. The pressure exerted by direct solar radiation was taken as 4.5×10^{-5} N/cm^2 (4.5×10^{-5} dyn/cm^2); therefore, the resulting acceleration is approximately 1×10^{-6} cm/sec^2, which is negligible.

The acceleration produced by atmospheric drag a was computed for the case where the spacecraft's velocity vector is parallel to its long axis, with an effective area-to-mass ratio A/m of 0.005 cm^2/g. We used the following equation:

$$a = \frac{C_d}{2} \frac{A}{m} \rho v^2 \quad , \tag{1}$$

where the drag coefficient C_d is 2, ρ is the atmospheric density, and v is the spacecraft velocity. With $\rho = 2.8 \times 10^{-13}$ g/cm^3 for an altitude of 200 kilometers, we get an acceleration of 0.0084 mm/sec^2. For the 10-second averaging time of the Doppler observations, the velocity change is thus 0.084 mm/sec for each data-sample period.

If drag accelerations are reasonably smooth, as is expected, it should be possible to separate the gravity variations satisfactorily even at a spacecraft altitude of 200 kilometers. Alternatively, the drag forces appear small enough that they can be modeled to sufficient accuracy. In any event, the drag effects are large enough that they must be computed accurately by using the measured orbital and altitude motions of both spacecraft.

2.3 Ionospheric Studies Using Satellite-to-Satellite Doppler Data

If a radiofrequency Doppler link is used between two spacecraft to obtain range-rate data, information about the electron concentration between the spacecraft can be obtained. In fact, the effects of the ionosphere must

be identified before accurate range rates can be determined. Consequently, a secondary goal of the Doppler Tracking Experiment was to analyze the resulting ionospheric information. In addition, it should be possible to probe traveling ionospheric disturbances with the satellite-to-satellite link and to detect the boundaries of turbulent regions of the ionosphere.

The analysis of ionospheric information is an extension of well-known methods (differential Doppler) of measuring the time change of the integrated electron concentration and other properties of the ionosphere along a radio path between a terminal moving in the ionosphere or above it and a station on the ground. Before artificial-satellite flights, these techniques were used in suborbital rocket flights to measure ionospheric parameters (refs. 7 and 8). Since 1957, a wealth of literature based on the use of multifrequency Doppler links between satellites and ground stations has appeared (refs. 9 to 17).

A fundamental problem in space-to-ground Doppler links is that the differential Doppler shift between two coherent, harmonically related frequencies is connected to the time derivative of the columnar electron content and not to the columnar content itself. This difficulty can be removed if simultaneous measurements are made of Faraday rotation. When Faraday rotation is not observed, the problem is underdetermined, and inversion of differential Doppler data into columnar content strongly depends on the presence of horizontal gradients in that region of the ionosphere swept through by the space-to-ground radio path while the spaceborne terminal is in motion.

The ASTP Doppler Tracking Experiment introduced a new feature, namely, measurements of horizontal gradients at a height near 220 kilometers by using a dual-frequency radio link between spacecraft in the same orbit.

In the case of a probe transmitting at frequency ω_1 through the ionosphere with a receiver on the ground,

$$\Phi_1(t) = \frac{\omega_1}{c} \int_0^{r(t)} n_1(r) \, dr \qquad (2)$$

when the spacecraft is at a height $r(t)$. The symbol Φ denotes the phase shift imparted to the transmitted signal due to passage through the ionosphere, and its time derivative is

$$\dot{\Phi}_1(t) = \frac{\omega_1}{c} \frac{d}{dt} \int_0^{r(t)} n_1(r) \, dr \; , \qquad (3)$$

where c is the velocity of light in free space and n(r) is the index of refraction at height r. The change of phase path with time is due in part to the spacecraft motion and in part to temporal changes of the index of refraction along the vertical between the spacecraft and the ground. If there are no temporal changes in the index of refraction along the path, then by assuming the spacecraft to be at height r_0 at time t_0, we have

$$\dot{\Phi}_1(t_0) = \frac{\omega_1}{c} \dot{r}(t_0) \, n_1(r_0) \quad . \tag{4}$$

If there are temporal changes, equation (2) becomes

$$\dot{\Phi}_1(t_0) = \frac{\omega_1}{c} \left[\dot{r}(t_0) \, n_1(r_0) + \int_0^{r(t)} \frac{\partial n_1(r)}{\partial t} \, dr \right] \quad , \tag{5}$$

where the term $\int_0^{r(t)} [\partial n_1(r)/\partial t] \, dr$ represents the temporal variation of the columnar refractivity in the entire vertical path between the spacecraft and the ground. The problem is underdetermined, and unless this variation is otherwise measured or becomes negligibly small, the inferring of $n_1(r_0)$ from $\dot{\Phi}_1(t_0)$ is affected by error.

When the effects of the Earth's magnetic field and the collision frequency on the index of refraction are disregarded, equation (4) can be rewritten as

$$\dot{\Phi}_1(t_0) = \frac{\omega_1}{c} \dot{r}(t_0) \left(1 - \frac{2\pi e^2 N}{m\omega_1^2} \right) \quad , \tag{6}$$

where N is the electron density and e and m are the charge and the mass of the electron, respectively; $2\pi e^2/m = 1587.6$ if N is in electrons per cubic meter and if ω_1 is in radians per second. From equation (4), we can determine the local index of refraction (and, hence, the electron density) at the spacecraft height by monitoring the received Doppler shift and by knowing, independently, the velocity of the spacecraft and the frequency radiated. With a single

15

frequency, it is necessary to know these two parameters very accurately. However, by adding a second frequency, ω_2, the equation of the differential Doppler shift in the spacecraft-to-ground link, when temporal changes are neglected, becomes

$$\delta\dot{\Phi} = \dot{\Phi}_1(t) - \frac{\omega_1}{\omega_2} \dot{\Phi}_2(t) = \frac{\omega_1}{c} \frac{d}{dt} \int_0^{r(t)} [n_1(r) - n_2(r)] \, dr = \frac{\omega_1}{c} \dot{r}(t_0) [n_1(r_0) - n_2(r_0)] \quad . \quad (7)$$

If we disregard the refractive effects of the Earth's magnetic field and the collision frequency, we get

$$\delta\dot{\Phi} = \frac{\omega_1}{c} \dot{r}(t_0) \frac{2\pi e^2 N}{m} \left(\frac{\omega_1^2 - \omega_2^2}{\omega_1^2 \omega_2^2} \right) \quad . \tag{8}$$

From equation (8), we can now deduce that the contribution to the measurement error arising from an error in estimating the link's frequencies is virtually eliminated.

We see from equation (6) that an error in frequency contributes directly to the error in $\dot{\Phi}_1(t_0)$. However, from equation (8), we find that the error in frequency must now be multiplied by the quantity $(n^2 - 1)\omega_1^{-2}$, which is usually very small. For instance, if $\omega_1/\omega_2 = n = 2$ and $\omega_1 = 2\pi \times 300 \times 10^6$ rad/sec, we have $(n^2 - 1)\omega_1^{-2} = 8.6 \times 10^{-19}$, and therefore the influence of the frequency error in the overall error of $\dot{\Phi}_1(t_0)$ is eliminated.

When the spacecraft trajectory is not vertical, other analytical expressions, which have already been developed by several authors, must be employed.

For the case in which horizontal gradients of the electron content are negligible, we can write, following Al'pert (ref. 11),

$$\delta\dot{\Phi}(t) = a_0 \left[-\frac{\dot{z}_s}{\cos \phi_s} N_s + \left(\dot{r}_s + \frac{\dot{z}_s}{\cos \phi_s} \right) \overline{N} \right] \quad , \tag{9}$$

where the velocity component $\dot{z}_s$ corresponds to the transmitter height z_s (measured along the local vertical z) and N_s is the local value of the electron concentration at that height; ϕ_s is the angle of incidence at the source measured from the local vertical. The parameter

$$\overline{N} = \frac{1}{z_s} \int_0^{z_s} N \, dz \tag{10}$$

is the mean value of the integrated electron concentration in a column having a cross section of 1 square centimeter. The coefficient a_0 is

$$a_0 = \frac{2\pi e^2}{m} \frac{\omega_1}{c} \left(\frac{1}{\omega_1^2} - \frac{1}{\omega_2^2} \right) \quad . \tag{11}$$

In Figure 2, r_s denotes the time-dependent radius vector joining the point of observation 0 to the moving source C, which is assumed to be approaching the observer and located at height z_s. The radial, horizontal, and vertical velocity components of the source are denoted, respectively, by $\dot{r}_s$ (along the line of sight), $\dot{x}_s$, $\dot{y}_s$, and $\dot{z}_s$.

In the general case, we can write for the electron concentration
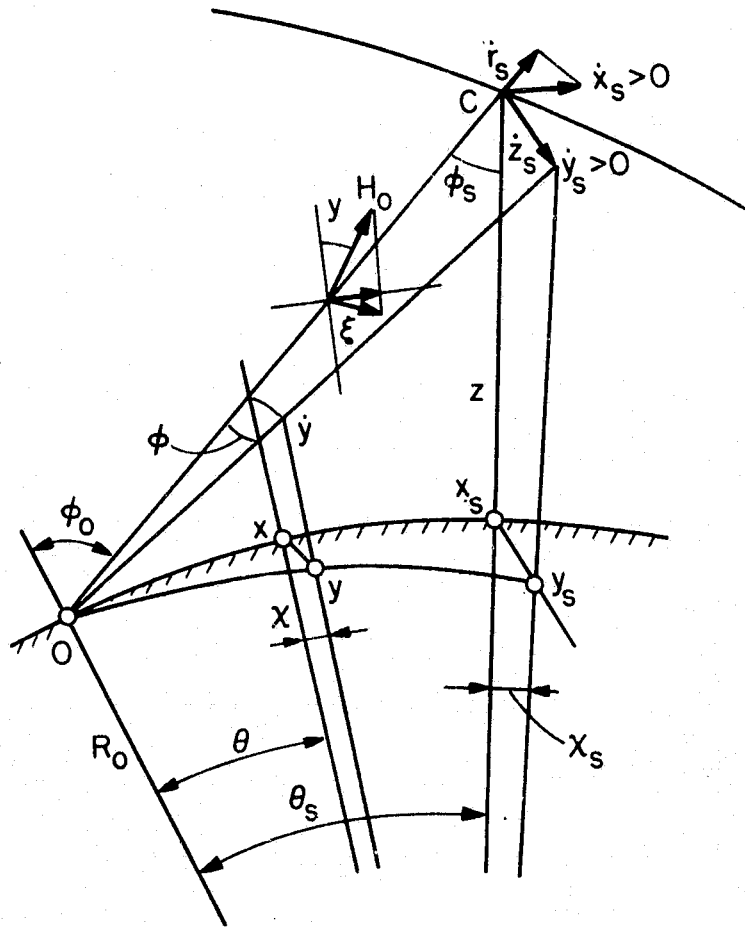
Figure 2. Nomenclature used in equations (12) through (16).

$$N = N(R, \theta, \chi, t) = N(z, x, y, t) \quad , \tag{12}$$

where (see Figure 2)

$$R = R_0 + z \quad , \quad x = R_0\theta \quad , \quad y = R_0\chi \quad , \tag{13}$$

and (z, θ, χ) is a variable coordinate in a spherical orthogonal coordinate system along the wave-propagation trajectory joining the point of observation $(0,0,0)$ and the point (z_s, θ_s, χ_s) at which the transmitter is located at time t; these points are denoted 0 and C, respectively, in Figure 2. The difference in the Doppler frequency shifts for the two coherent radio waves can then be written in the form

$$\delta\dot{\Phi}(t) = a_0 \frac{d}{dt} \int_{R_0}^{R_s(t)} N(x, y, z, t) \frac{dz}{\cos \phi(t)} \quad . \tag{14}$$

If certain conditions are satisfied, as in the Doppler Tracking Experiment, we obtain (ref. 11)

$$\delta\dot{\Phi} = a_0 \left[-N_s \frac{\dot{z}_s}{\cos \phi_s} + \overline{N}_x \left(\dot{r}_s + \frac{\dot{z}_s}{\cos \phi_s} \right) - \overline{N}_y \dot{y}_s - N_t \right] \quad . \tag{15}$$

When the further simplifying assumption is made that the medium is plane parallel (i.e., the Earth's sphericity is neglected), the various parameters of equation (15)(ref. 11) are defined as follows:

$$\overline{N}_x = \frac{1}{z_s} \int_0^{z_s} N \, dz + \frac{1}{z_s \sin \phi_0 \cos \phi_0} \int_0^{z_s} \frac{\partial N}{\partial x} z \, dz \quad ,$$

$$\overline{N}_y = \frac{1}{z_s \cos \phi_0} \int_0^{z_s} \frac{\partial N}{\partial y} z \, dz \quad ,$$

$$N_t = \frac{1}{\cos \phi_0} \int \frac{\partial N}{\partial t} \, dz \quad . \tag{16}$$

Even in the planar approximation, the problem is inadequately determined. The difficulty was, in part, alleviated in our experiment by the fact that the DM-to-CSM dual-frequency link measured the quantity $\partial N/\partial x$ (the horizontal gradients in the orbital plane) at the ASTP orbital height:

$$\delta \dot{\Phi} = \dot{\Phi}_1(t) - \frac{\omega_1}{\omega_2} \dot{\Phi}_2 = \frac{\omega_1}{c} \frac{\partial}{\partial t} \left[\int_{DM}^{CSM} n_1(x) \, dx - \int_{DM}^{CSM} n_2(x) \, dx \right] \quad . \tag{17}$$

Assuming that the two spacecraft remained at a constant separation (relative velocity = 0), we obtain

$$\delta \dot{\Phi} = \frac{\omega_1}{c} \int_{DM}^{CSM} \frac{\partial}{\partial x} [n_1(x) - n_2(x)] \frac{\partial x}{\partial t} \, dx \quad . \tag{18}$$

By neglecting the refractive effects of the Earth's magnetic field and the collision frequency, we can rewrite equation (18) as follows:

$$\delta\dot{\Phi} = \frac{\omega_1}{c}\frac{2\pi e^2}{m}\left(\frac{\omega_1^2 - \omega_2^2}{\omega_1^2 \omega_2^2}\right) \int_{DM}^{CSM} \frac{\partial N}{\partial x}\frac{\partial x}{\partial t}\, dx \quad , \tag{19}$$

where $\partial x/\partial t$ is known from orbital-mechanics considerations and $\partial N/\partial x$ can therefore be obtained from the measured values of $\delta\dot{\phi}$ in the DM-to-CSM path. Before it can be used in equation (16), however, $\partial N/\partial x$ must be known all along the vertical z. In fact, what is needed is the function $\int_0^z (\partial N/\partial x)\, z\, dz$ (and not just $\partial N/\partial x$ at the ASTP orbital height of 220 kilometers). We must therefore construct a model of $(\partial N/\partial x)\, z$ in the lower ionosphere, with the constraint of satisfying both the value measured at 220 kilometers by the DM-to-CSM link and a value equal to zero measured at the ionosphere's bottom. A linear variation of the gradient between these two values thus seems to be an acceptable assumption.

With the MA-089 experiment, we were unable to observe Faraday rotation (rotating Doppler) in either link. In the DM-to-CSM link, the receiving antenna was circularly polarized; and in the DM-to-ground link, there was no provision for recording signal strength.

2.4 Analysis of the Motion of the Docking Module about Its Center of Mass

Knowledge of the orientation of the two spacecraft is required for an exact evaluation of the forces acting on their centers of mass. Atmospheric drag

21

and radiation pressure depend on the orientation, and, in principle, the gravitational force depends to second order; but these forces are small enough that only crude orientation information is necessary. However, the observed Doppler signal measures the relative velocity of the antenna phase centers of the DM transmitter and the CSM receiver, which includes the antenna motion around the respective center of mass of these two bodies. To reconstruct the relative motion of the centers of mass, we must reconstruct the rotational motion of the DM from Doppler measurements of the relative velocity of the antenna phase center. The motion of the DM around its center of mass is described in the following.

2.4.1 The motion of the DM antenna phase center with respect to the
       DM center of mass

Let us consider a reference system $R_1(0;x,y,z)$ geometrically attached to a rigid part of the DM; for example, with the origin at the center of the flange that connects the DM to the CSM, with the x and y axes in the plane of the flange and parallel to the pitch and yaw axes, respectively, and with the z axis parallel to the roll axis (this is the system used by North American Rockwell). A second reference system $R_2(G;\xi,\eta,\zeta)$ is taken with its origin at the center of mass of the DM and with its axes coincident with the principal axes of the centroidal inertia ellipsoid. The first reference system is known but not well-defined, while the second one is well-defined but not very well known. A third reference system $R_3(0*;x',y',z')$ has its origin at the computed center of mass and its axes along the computed principal axes relative to the computed center of mass.

The transformation between R_1 and R_3 is known. The transformation between R_2 and R_3 is not known, but we assume that the upper limits on the vector $\underset{\sim}{O}{}^*\underset{\sim}{G}$ and on the direction cosines between (x',y',z') and (ξ,η,ζ) are known. If the angles between the R_2 and the R_3 systems are small, then to first order we can write

$$\underset{\sim}{x}' = A\xi \quad,$$

where

$$A = \begin{pmatrix} 1 & \alpha & -\beta \\ -\alpha & 1 & \gamma \\ \beta & -\gamma & 1 \end{pmatrix} \quad.$$

The true values of the moments of inertia differ from the calculated values in the R_2 system only by quantities of the second order in $\underset{\sim}{O}{}^*\underset{\sim}{G}$ and α, β, and γ, but the products of inertia differ from zero by quantities of the order of α, β, and γ. The position of the antenna of the transmitter with respect to the R_3 system was assumed to be accurately known since its position in R_1 is measured and the transformation from R_1 to R_3 is known.

While telemetry data are available on the motion of the CSM (such as gyro rate and gimbal position), the only direct information we have on the orientation of the DM is from the Doppler signals and from the photographs taken from the CSM during the first 5 minutes after separation.

2.4.2 Simulation of the motion of the DM

To simulate the motion of the DM, we have made another fundamental assumption — that the DM is a rigid body subjected only to thermal expansion and contraction. With respect to reference system R_2, we have uncertainties in 1) the initial conditions, 2) the position of the antenna center, and 3) the geometry and orientation of the radiation pattern.

In constructing the equations of motion, we considered all the torques acting on the DM and selected those that had a measurable effect.

2.4.3 Gravitational torque

In the reference system R_2 fixed to the DM, the graviational torque is given by

$$\underset{\sim}{\mathscr{T}} = \frac{3n^2a^3}{R^5} [(C - B)(\underset{\sim}{R} \cdot \underset{\sim}{j})(\underset{\sim}{R} \cdot \underset{\sim}{k}) \underset{\sim}{i} + (A - C)(\underset{\sim}{R} \cdot \underset{\sim}{k})(\underset{\sim}{R} \cdot \underset{\sim}{i}) \underset{\sim}{j}$$
$$+ (B - A)(\underset{\sim}{R} \cdot \underset{\sim}{i})(\underset{\sim}{R} \cdot \underset{\sim}{j}) \underset{\sim}{k}] \tag{20a}$$

or

$$\underset{\sim}{\mathscr{T}} = 3n^2 \left(\frac{a}{R}\right)^3 [(C - B) \mu\nu\underset{\sim}{i} + (A - C) \nu\lambda\underset{\sim}{j} + (B - A) \lambda\mu\underset{\sim}{k}] \quad , \tag{20b}$$

where n is the mean motion; a is the semimajor axis; R is the radius vector; λ, μ, and ν are the direction cosines of the unit vector directed from the

24

the DM to the center of the Earth; and A, B, and C are the principal moments
of inertia of the DM with the ordering A < B < C.

When the DM was rotating about its z axis normal to the orbital plane
(assumed fixed), then $\nu = 0$ and equation (20b) simplifies to

$$\mathscr{T} = \frac{3}{2} n^2 \left(\frac{a}{R}\right)^3 (B - A) \sin 2\Theta k \quad , \tag{21}$$

where Θ is the angle between the radius vector and the body-fixed x axis.
For a first approximation of the magnitude of the graviational torque, we used

$$A = 1.089 \times 10^{10} \text{ cgs} \quad ,$$

$$B = 2.348 \times 10^{10} \text{ cgs} \quad ,$$

$$C = 2.588 \times 10^{10} \text{ cgs} \quad ,$$

$$n \cong 2\pi/5300 \text{ rad/sec}$$

in equation (21) to obtain

$$\left|\mathscr{T}\right| \lesssim 2 \times 10^4 \text{ cgs} \quad .$$

Since the DM appeared to be tumbling about its z axis with an angular velocity
of about 5°/sec, its angular momentum is about 10^9 cgs and we have

$$\frac{|\Delta H|}{H} = \frac{\tau \Delta t}{H} \quad , \tag{22}$$

so that in 5×10^4 seconds, the angular-momentum vector could change, in principle, by a measurable amount.

A more refined analysis can be made if we assume that the motion of the DM is one of almost pure tumbling about the z axis normal to the orbital plane and that the orbit is circular and if we accept the approximation of averaging over one tumbling cycle. We then have

$$\underset{\sim}{\omega} = \omega_0 \underset{\sim}{k} \ , \qquad \underset{\sim}{H} = C\omega_0 \underset{\sim}{k} \ , \qquad \underset{\sim}{R} = R\underset{\sim}{\lambda} \ , \tag{23}$$

and

$$\underset{\sim}{\mathscr{T}} = 3n^2 \left(\frac{a}{R}\right)^3 [(C - B)(\underset{\sim}{\lambda} \cdot \underset{\sim}{j})(\underset{\sim}{\lambda} \cdot \underset{\sim}{k}) \underset{\sim}{i} + (A - C)(\underset{\sim}{\lambda} \cdot \underset{\sim}{k})(\underset{\sim}{\lambda} \cdot \underset{\sim}{i}) \underset{\sim}{j}$$

$$+ (B - A)(\underset{\sim}{\lambda} \cdot \underset{\sim}{i})(\underset{\sim}{\lambda} \cdot \underset{\sim}{j}) \underset{\sim}{k}] \ . \tag{24}$$

Defining a new coordinate system, as shown in Figure 3, we have the following relations:

$$\underset{\sim}{\lambda} = \cos\theta \cos\omega_0 t \underset{\sim}{i} + \cos\theta \sin\omega_0 t \underset{\sim}{j} + \sin\theta \underset{\sim}{k} \ ,$$

$$\underset{\sim}{u} = \frac{\underset{\sim}{\lambda} \times \underset{\sim}{k}}{\sin\theta} \ ,$$

$$\underset{\sim}{v} = \frac{\underset{\sim}{k} \times (\underset{\sim}{\lambda} \times \underset{\sim}{k})}{\sin\theta} \ ,$$

$$\underset{\sim}{i} = \sin\omega t \underset{\sim}{u} + \cos\omega t \underset{\sim}{v} \ , \tag{25}$$

$$\underset{\sim}{j} = -\cos\omega t \underset{\sim}{u} + \sin\omega t \underset{\sim}{v} \ ,$$

$$\cos\theta = \underset{\sim}{\lambda} \cdot \underset{\sim}{k} \ .$$
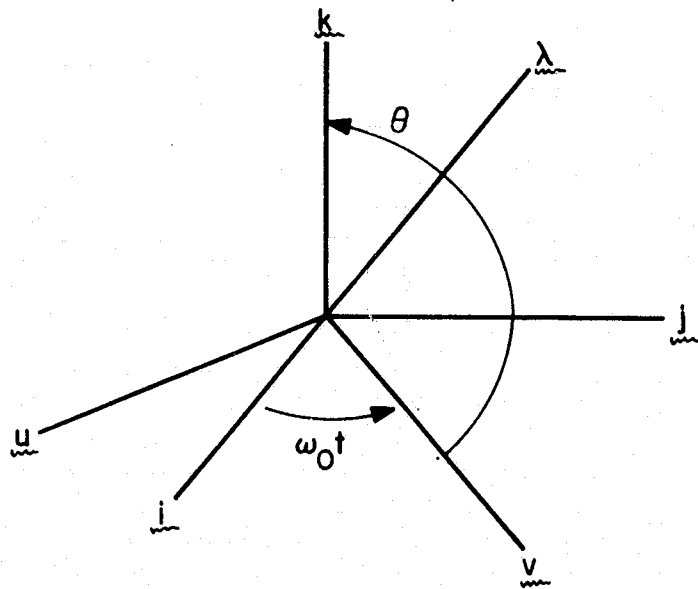
Figure 3. New coordinate system.

After substituting equations (25) into equation (24) and averaging over one tumbling cycle, we find

$$\langle \mathcal{T} \rangle = \frac{3}{2} n^2 \left(\frac{a}{R}\right)^3 \sin \Theta \cos \Theta \, (2C - B - A) \, \underset{\sim}{u} \tag{26}$$

or

$$\langle \mathcal{T} \rangle = \frac{3}{2} n^2 \left(\frac{a}{R}\right)^3 (2C - B - A)(\underset{\sim}{\lambda} \cdot \underset{\sim}{k})(\underset{\sim}{\lambda} \times \underset{\sim}{k}) \quad . \tag{27}$$

If we call $\underset{\sim}{h}$ the unit vector normal to the orbital plane and $\underset{\sim}{N}$ the unit vector along the line of nodes and assume a circular orbit, we have

$$\underset{\sim}{\lambda} = \cos nt \underset{\sim}{N} - \sin nt \underset{\sim}{h} \times \underset{\sim}{N} \quad . \tag{28}$$

We substituted equation (28) into equation (27) and averaged over one orbital period to get

$$\langle \mathcal{T} \rangle = \frac{3}{4} n^2 (2C - B - A) \, [(\underset{\sim}{N} \cdot \underset{\sim}{k})(\underset{\sim}{N} \times \underset{\sim}{k}) + (\underset{\sim}{h} \times \underset{\sim}{N}) \times \underset{\sim}{k}] \quad . \tag{29}$$

If we define the unit vector $\underset{\sim}{M}$ in the orbital plane forming an orthogonal system with $\underset{\sim}{h}$ and $\underset{\sim}{N}$, then

$$\langle \mathcal{T} \rangle = \frac{3}{4} n^2 (2C - B - A) \, [(\underset{\sim}{N} \cdot \underset{\sim}{k})(\underset{\sim}{N} \times \underset{\sim}{k}) + (\underset{\sim}{n} \cdot \underset{\sim}{k})(\underset{\sim}{n} \times \underset{\sim}{k})] \quad . \tag{30}$$

The nodal line $\underset{\sim}{N}$ regressed at about 5°3 per day; thus, even if the DM initially tumbled in the orbital plane, for which the averaged torque would

be zero, the torque grew with time during the course of the experiment. In one-half a day, $\underset{\sim}{h}$ changed by about 2°, with the maximum averaged torque increasing from zero to less than 10^3 dyn-cm. This is about 20 times less than the previous estimate and therefore is negligible. This gravitational torque does not have first-order secular effects on the tumbling rate, because it averages out in one tumbling period.

Let us now assume that the DM was tumbling about its z axis normal to the orbital plane. We want to know if the modulation of the angular velocity by the gravitational torque produced a detectable effect on the velocity of the antenna center. In this case, the equation of motion simplifies to

$$\ddot{\Theta} + \frac{3}{2} n^2 \frac{B - A}{C} \sin 2\Theta = 0 \quad , \tag{31}$$

which can be integrated once to give

$$\dot{\Theta}^2 = \dot{\Theta}_0^2 + \alpha \cos 2\Theta \quad , \tag{32}$$

where

$$\alpha = \frac{3}{2} n^2 \frac{B - A}{C} = 9 \times 10^{-7}/\text{sec}$$

and $\Theta_0 = 0$. If $\dot{\Theta}_0 = 5°/\text{sec} = 0.087$ rad/sec, then

$$\Delta\dot{\Theta} = \frac{\alpha}{\dot{\Theta}_0} = 2.88 \times 10^{-5} \text{ rad/sec} \quad .$$

If the perpendicular distance from the angular-velocity vector to the antenna center is 300 millimeters, then the modulation of the signal would be 8×10^{-3} mm/sec, which is negligible.

2.4.4 Atmospheric effects

Atmospheric drag affects the motions both of and about the center of mass of the DM, since the instantaneous resultant drag force depends on the orientation of the DM.

We considered first the motion about the center of mass and evaluated the maximum torque as follows:

$$\mathscr{T}_{max} = \frac{C_D \rho V^2 A a}{2} \quad , \tag{33}$$

where C_D is the drag coefficient, ρ is the atmospheric density, V is the velocity of the DM, A is its cross-section area, and a is the distance between the center of mass and the center of pressure. Taking a = 30 centimeters, we found

$$\mathscr{T}_{max} = (2.2 \times 10^{-13} \times 6.2 \times 10^{11} \times 7 \times 10^4 \times 30)/2$$
$$= 1.4 \times 10^5 \text{ dyn-cm} \quad , \tag{34}$$

which is not negligible. If the motion is that of tumbling about an axis normal to the orbital plane, then the torque averages to zero over a tumbling

cycle and the only effect will be a modulation of the angular velocity similar to and of the same order as the effect of the gravitational torque.

A simple analysis of the atmospheric-drag effect can be made if we assume that the motion is one of pure tumbling in the orbital plane. We have two effects: the change in the velocity of the center of mass of the DM due to the change in A over one tumble period, and the modulation of the angular velocity mentioned previously. These are discussed separately below.

To evaluate the first effect of air drag, we assumed that the orbit is circular with an altitude of 220 kilometers and that the air density is about 10^{-13} g/cm^3. The equation for the tangential acceleration is

$$\frac{dV}{dt} = - \frac{C_D \rho A(t) V^2}{2n} \quad . \tag{35}$$

We evaluated A(t) by assuming the DM to be a cylinder that is 1.5 meters in diameter and 3.5 meters long and is tumbling at 3°/sec about an axis perpendicular to its longitudinal axis. If α is the angle between the velocity vector and the longitudinal axis of the DM, then

$$A(t) = a \left| \sin \alpha \right| + b \left| \cos \alpha \right| \quad , \tag{36}$$

where

$$a = 5.25 \times 10^4 \text{ cm}^2 \quad , \qquad b = 1.79 \times 10^4 \text{ cm}^2 \quad ,$$

31

and $\alpha = \sigma t = 0.052t$. We substituted equation (36) into equation (35) and integrated, assuming that V^2 on the right-hand side is constant and that the time interval is less than or equal to one-quarter of a tumbling cycle. This gives

$$V - V_0 = - \frac{C_D \rho V^2}{2m\sigma} [a(1 - \cos \sigma t) + b \sin \sigma t] \quad .$$ (37)

Over a quarter tumbling cycle,

$$t = \frac{\pi}{2\sigma} \quad ,$$

and thus,

$$\Delta V = - \frac{C_D \rho V^2}{2m\sigma} (a + b) = -0.04 \text{ cm/sec} \quad .$$ (38)

The average acceleration is

$$\dot{\overline{V}} = \frac{4 \Delta V}{\rho} = \frac{C_D \rho V^2 (a + b)}{m\pi} \quad ,$$ (39)

and the periodic change in V is

$$V - V_0 = \dot{\overline{V}} t \quad ,$$ (40a)

$$V_{per} = - \frac{C_D \rho V^2}{m} \left[\frac{a}{2\sigma} (1 - \cos \sigma t) + \frac{b}{2\sigma} \sin \sigma t - \frac{a + b}{\pi} t \right] \quad .$$ (40b)

We obtained the amplitude of the velocity modulation by differentiating equation (40b) and setting it equal to zero. The result,

$$\Delta V_{per} = 5 \times 10^{-2} \text{ mm/sec} \quad ,$$

is negligible.

For the second effect of air drag, we assumed that the center of pressure of the DM was at a distance d from the center of mass along the longitudinal axis. The torque is then $Fd \sin \alpha$, where F is the force of air drag. The equation of motion becomes

$$\ddot{\alpha} = \frac{C_D \rho V^2 d \sin \alpha}{2C} (a |\sin \alpha| + b |\cos \alpha|) \tag{41}$$

or

$$\ddot{\alpha} = \beta[a(1 - \cos 2\theta) + b \sin 2\theta] \tag{42}$$

during the first quarter revolution and

$$\ddot{\alpha} = \beta[a(1 - \cos 2\theta) = b \sin 2\theta] \tag{43}$$

during the second, where

$$\beta = \frac{C_D \rho V^2 d}{4G} \quad .$$

Integrating equation (42) from 0 to $\pi/2$, we have

$$\frac{\dot{\alpha}\pi}{2} = \dot{\alpha}_0 + 2\beta\left(\frac{\pi}{4} a + b\right) \tag{44a}$$

or

$$\Delta\dot{\alpha} = \frac{\beta[a(\pi/4) + b]}{\dot{\alpha}_0} \quad . \tag{44b}$$

Using the previously stated parameters and the rather extreme value of d = 30 centimeters, we found

$$\Delta\dot{\alpha} = 5 \times 10^{-5} \text{ rad/sec} \quad . \tag{45}$$

During the next quarter revolution, $\Delta\dot{\alpha}$ increased by another 5×10^{-5} rad/sec and then decreased to zero over the last quarter. The amplitude of the modulation of the angular velocity, therefore, is 5×10^{-5} rad/sec. Using 300 millimeters for the perpendicular distance between the angular-velocity vector and the antenna center, we found the modulation of the signal to be 1.5×10^{-2} mm/sec, which is negligible.

We also evaluated the secular effect of atmospheric drag on the tumbling rate ω_3. To obtain an upper limit on this function, we considered the total amount of atmosphere impinging on the DM per second, $\rho A_{av} V$, and assumed that, at the expense of the DM's angular momentum, we could impart to the impinging volume of atmosphere an angular velocity equal to that of the DM:

$$C\frac{d\omega_3}{dt} = -\rho A_{av} V\omega a^2 \quad ,$$

where a is the average radius in question. Taking 1 m as the upper limit of a, then, over the duration of the experiment (approximately 50,000 seconds), we have

$$\Delta T/T = 10^{-4} \quad ,$$

where $T = 2\pi/\omega_3$. However, from observations, we found a variation of $\Delta T = 10^{-2}T$, which clearly cannot be explained by atmospheric-drag effects alone.

2.4.5 Radiation-pressure effects

The radiation-pressure torque will have a maximum magnitude of

$$\mathscr{T}_{rp} = \frac{I}{C} Ad \quad , \tag{46}$$

where I is the solar constant, c is the speed of light, A is the area of the DM, and d is an estimate of the distance between the center of mass and the center of pressure of the DM. Using $A = 7 \times 10^4$ cm^2 and d = 30 centimeters, we get

$$\mathscr{T}_{rp} \cong 100 \text{ dyn-cm} \quad , \tag{47}$$

which is completely negligible.

2.4.6 Magnetic-torque effects

The torque produced by the Earth's magnetic field on the intrinsic dipole moment of the DM is given by

$$\mathcal{T} = \underset{\sim}{M} \times \underset{\sim}{H} \quad , \tag{48}$$

where $\underset{\sim}{M}$ is the magnetic moment of the DM and $\underset{\sim}{H}$ is the intensity of the Earth's magnetic field. If we take $\underset{\sim}{M} = 1$ amp-m^2 and $\underset{\sim}{H} = 2 \times 10^{-5}$ webers/m^2, then the magnitude of the torque will be 2×10^{-5} newton-m or 200 dyn-cm. Even if the magnetic moment has the very large value of 10 amp-m^2, the torque will be 2×10^3 dyn-cm if a reasonable estimate is used for the magnetic moment of the DM. Owing to the short time period of the experiment, the effect of this torque on the orientation of the angular-momentum vector appears to be negligible. Both the short-period effects (the tumbling frequencies) and the secular effects (which average out to a second-order effect) on the tumbling rate are also negligible in comparison to the large observed variation.

Magnetic hysteresis and eddy currents result in torques no larger than 100 dyn-cm, assuming that the electromagnetic characteristics of the DM have been modeled with a reasonable approximation. This value is 30 times smaller than the amount required to explain the fact that the tumbling period of the DM changed by 2.5 seconds every 72 seconds over the 50,000-second duration of the experiment.

2.4.7 Tumbling-rate variation due to thermal effects

For the purpose of the present discussion, let us assume that the rotation axis of the DM remained relatively close to normal to the orbital plane during the doppler experiment and that the plane and the orientation of the DM–Sun line did not change by much during the same period of time. Consequently, on the day side of the orbit, solar radiation heated the DM, making a constant angle with the rotation axis. Although a reconstruction of the orientation is fairly simple, a good determination of thermal deformation, expansion, and distortion, with a consequent change in the inertia tensor, is not easy.

For a rough evaluation of the magnitude of the effects, we consider the simple case, which may be close to reality, of homothetic thermal expansion and contraction and compute the corresponding variation in the tumbling frequency. Given reasonable values for the absorption and emission coefficients of the DM, and for its geometrical characteristics, a maximum variation of 150°C would be expected when the DM passes from sunlight to shadow, and vice versa; certainly, a minimum value would be of the order of 80°C. The time constant for these variations is of the order of a few minutes.

At this point, a very simple computation can be made on the variation of the tumbling rate. For the conservation of angular momentum, we have

$$I\omega = \text{const}$$

and therefore

$$\Delta I \cdot \omega = -\Delta\omega \cdot I \qquad \text{or} \qquad \frac{\Delta I}{I} = \frac{\Delta T}{T} \qquad .$$

Now we can write

$$I = M\rho^2 \quad ,$$

where ρ is the radius of gyration. If the variation of the DM is homothetic, the axis of maximum moment of inertia remains almost constant in direction (within the body) and therefore

$$\Delta I = 2M\rho\Delta\rho \qquad .$$

We then have

$$\frac{\Delta T}{T} = \frac{2\Delta\rho}{\rho} \qquad .$$

For a variation in temperature $\Delta\tau$ and an expansion coefficient ϵ, we get

$$\Delta\rho = \rho\epsilon\Delta\tau$$

and finally

$$\frac{\Delta T}{T} = 2\epsilon\Delta\tau \quad ,$$

which, for $\epsilon = 2.4 \times 10^{-5}\ {}^{\circ}K^{-1}$ and $\Delta\tau = 150^{\circ}$, gives

$$\frac{\Delta T}{T} = 4.8 \times 10^{-5} \times 150 = 7.2 \times 10^{-3} \qquad .$$

Since the tumbling period is 72 seconds, we have a variation in the period of 0.35 second.

2.4.8 Integration of the equations of motion

As a straightforward method, we chose to integrate the three Eulerian equations considered to be first-order differential equations in ω_1, ω_2, and ω_3, plus nine first-order auxiliary equations in the direction cosines of the body-fixed axes with respect to an inertial frame. The Eulerian equations are

$$A\dot{\omega}_1 - (B - C)\omega_2\omega_3 = \mathscr{T}_1 \quad ,$$

$$B\dot{\omega}_2 - (C - A)\omega_3\omega_1 = \mathscr{T}_2 \quad , \qquad (49)$$

$$C\dot{\omega}_3 - (A - B)\omega_1\omega_2 = \mathscr{T}_3 \quad ,$$

where $\mathscr{T}_1$, $\mathscr{T}_2$, and $\mathscr{T}_3$ are the components of the applied torque about the body-fixed axes x, y, and z, respectively. If we let $\underset{\sim}{i}$, $\underset{\sim}{j}$, and $\underset{\sim}{k}$ be the unit vectors along the body-fixed principal axes and $\underset{\sim}{I}$, $\underset{\sim}{J}$, and $\underset{\sim}{K}$ be the unit vectors of the inertial coordinate system, then the direction cosines α_i, β_i, and γ_i are as follows:

$$\underset{\sim}{I} = \alpha_1\underset{\sim}{i} + \alpha_2\underset{\sim}{j} + \alpha_3\underset{\sim}{k} \quad ,$$

$$\underset{\sim}{J} = \beta_1\underset{\sim}{i} + \beta_2\underset{\sim}{j} + \beta_3\underset{\sim}{k} \quad , \qquad (50)$$

$$\underset{\sim}{K} = \gamma_1\underset{\sim}{i} + \gamma_2\underset{\sim}{j} + \gamma_3\underset{\sim}{k} \quad .$$

Then, since $dI/dt = 0$, we have

$$\dot{\alpha}_1\underset{\sim}{i} + \alpha_1\underset{\sim}{\omega} \times \underset{\sim}{i} + \dot{\alpha}_2\underset{\sim}{j} + \alpha_2\underset{\sim}{\omega} \times \underset{\sim}{j} + \dot{\alpha}_3\underset{\sim}{k} + \underset{\sim}{\omega} \times \underset{\sim}{k} = 0 \quad . \qquad (51)$$

Expanding the cross products, we obtain the three scalar first-order differential equations:

$$\dot{\alpha}_1 = \alpha_2 \omega_3 - \alpha_3 \omega_2 \quad,$$

$$\dot{\alpha}_2 = \alpha_3 \omega_1 - \alpha_1 \omega_3 \quad, \tag{52}$$

$$\dot{\alpha}_3 = \alpha_1 \omega_2 - \alpha_2 \omega_1 \quad.$$

We can differentiate the second and third parts of equations (50) to obtain similar equations for $\dot{\beta}_i$ and $\dot{\gamma}_i$:

$$\dot{\beta}_1 = \beta_2 \omega_3 - \beta_3 \omega_2 \quad,$$

$$\dot{\beta}_2 = \beta_3 \omega_1 - \beta_1 \omega_3 \quad, \tag{53}$$

$$\dot{\beta}_3 = \beta_1 \omega_2 - \beta_2 \omega_1 \quad,$$

and

$$\dot{\gamma}_1 = \gamma_2 \omega_3 - \gamma_3 \omega_2 \quad,$$

$$\dot{\gamma}_2 = \gamma_3 \omega_1 - \gamma_1 \omega_3 \quad, \tag{54}$$

$$\dot{\gamma}_3 = \gamma_1 \omega_2 - \gamma_2 \omega_1 \quad.$$

The set of first-order differential equations, (49) and (52) through (54), can then be integrated numerically, provided that $\mathscr{T}_1$, $\mathscr{T}_2$, and $\mathscr{T}_3$ are suitably specified as functions of time or of ω_i, α_i, β_i, and γ_i.

To integrate the above equations numerically, we used only the gravitational torque. In one case, we started with the DM tumbling about its axis at $3°$/sec normal to a fixed orbital plane and duplicated the results of equation (33). In another case, using the same initial conditions, we allowed the orbital plane to precess at a rate of $5°.5$/day. After 4 hours, the amplitude of the modulation of ω_3 was unchanged, remaining about 1.8×10^{-5} rad/sec, and the modulations of ω_1 and ω_2, while increasing secularly, were less than 5×10^{-7} rad/sec. The effects of gravitational torque are therefore negligible. The same must be true for the effects of the other torques considered above.

In reality, we found while analyzing the data (see Section 6.3.3) that the tumble period changed from 70.5 to 71.9 seconds, a phenomenon that remains unexplained. Several possibilities were examined, but none has any observational support. Among them is the possible variation of the inertia tensor of the DM. This variation might result in part from secular effects due to an increase in mean temperature, whose periodic component explains reasonably well the variation of the tumbling rate when the DM moved from sunlight to shadow. Other possibilities include the motion of unsecured items inside the DM that might have been subjected to the field of forces, such as centrifugal, established in the DM. These centrifugal forces, combined with the periodic thermal variation, may increase the moment of inertia about the tumbling axis, thus causing a decrease in the tumbling rate. Although some perplexity remains in this aspect of the problem, it appears from the data that the fundamental characteristics of the motion can be described accurately enough, at least in a first approximation, by assuming, as we did, that the motion of the DM is that of a rigid body free of torque during properly limited intervals of time. To gain insight on the observational data, we treat this case as a first approximation in the following subsection.

2.4.9 DM motion about the center of mass with the DM considered as a rigid body free of torque

We assumed here the usual notation for the Eulerian angle and refer to the well-known analytical treatment of the motion of a torque-free rigid body. The inertial frame is taken with the z axis along the angular-momentum vector, which is constant in orientation since the motion is free of external torques. The fundamental period of the motion of the DM is the tumbling period, since the motion in the zero approximation was a tumbling motion about an axis almost normal to the orbital plane. This fundamental period is the period of the Eulerian angle $\phi + \psi$.

We have the following relations:

$$\omega_3 = \dot{\phi} \cos \theta + \dot{\psi} \tag{55}$$

and

$$\dot{\phi} + \dot{\psi} = \omega_3 + (1 - \cos \theta) \, \dot{\phi} \quad . \tag{56}$$

If we call M the modulus of the angular momentum, we have

$$\dot{\phi} = \frac{M(A\omega_1^2 + B\omega_2^2)}{A^2\omega_1^2 + B^2\omega_2^2} = \frac{M(A\omega_1^2 + B\omega_1^2)}{M^2 \sin^2 \theta} \tag{57}$$

and obtain, after algebraic manipulation,

$$\dot{\phi} + \dot{\psi} = \frac{(M/A) \ [\cos \theta + (C/D)]}{1 + \cos \theta} \quad , \tag{58}$$

where

$$D = M^2/2E \quad ; \tag{59}$$

M, D, and E are constants since the motion is torque free. The following formulas are also pertinent to the development:

$$k^2 = \frac{(B - A)(C - D)}{(C - B)(D - A)} \quad , \tag{60}$$

$$k'^2 = 1 - k^2 \quad , \qquad q \cong \frac{1}{2} \frac{1 - k'^{1/2}}{1 + k'^{1/2}} \quad , \qquad \left(\frac{2K}{\pi}\right)^{1/2} \cong 1 + 2q \ ,$$

where k^2 is the modified elliptic function and K is the complete elliptic integral. We then have

$$\cos \theta = \left[\frac{C(D - A)}{D(C - A)}\right]^{1/2} dn \ \mu t \quad , \tag{61}$$

where

$$\mu = \frac{\pi}{2K} \frac{M}{I_3} \left[\frac{C(C - B)(D - A)}{DAB}\right]^{1/2} \quad . \tag{62}$$

Finally, we can write

$$\dot{\phi} + \dot{\psi} = \frac{M}{C} \left[1 + \frac{C - D}{D(1 + \cos\theta)} \right] \quad . \tag{63}$$

Equation (63) shows that the quantity $\dot{\phi} + \dot{\psi}$ is a constant plus a small variable even for reasonably large values of θ. The mean angular velocity for small k^2 is then

$$\overline{\dot{\phi} + \dot{\psi}} = \frac{M}{C} \left[1 + \frac{(C - D)/D}{1 + \overline{\cos\theta}} \right] \quad , \tag{64}$$

where

$$\overline{\cos\theta} = \frac{1}{2} (\cos\theta_{max} + \cos\theta_{min}) \tag{65}$$

and

$$\overline{\cos\theta}_{min} = \left[\frac{C(D - A)}{D(C - A)} \right]^{1/2} \quad , $$

$$\overline{\cos\theta}_{max} = \left[\frac{C(D - B)}{D(C - B)} \right]^{1/2} \quad . \tag{66}$$

An alternative representation would be

$$\overline{\cos\theta} = \frac{\pi}{2K} \cos\theta_{min} \quad . \tag{67}$$

Finally, for the amplitudes of the two components ω_1 and ω_2, we have the following expressions:

$$\omega_{10} = M \left[\frac{C - D}{DA(C - A)} \right]^{1/2} \quad , \quad \omega_{20} = M \left[\frac{C - D}{DB(C - B)} \right]^{1/2}$$

(68)

$$\omega_1 = \omega_{10} (\cos \mu t + q \cos 3\mu t) \quad , \quad \omega_2 = \omega_{20} (\sin \mu t + q \sin 3\mu t) \quad .$$

All the above relations represent the dynamics of a torque-free non-symmetric rigid body. Next we proceeded to find the relevant kinematic formulas. We call $\underset{\sim}{R}$ the vector GC, where G is the actual center of gravity and C the center of phase of the DM antenna; the unit vector along the line of sight from the DM to the CSM is given by λ. We introduce the following notation:

$$\underset{\sim}{R} = \begin{pmatrix} \ell_1 \xi + \ell_2 \eta + \ell_3 \zeta \\ m_1 \xi + m_2 \eta + m_3 \zeta \\ n_1 \xi + n_2 \eta + n_3 \zeta \end{pmatrix} \quad ,$$

$$\underset{\sim}{\lambda} = \begin{pmatrix} \cos(nt + \varepsilon) \cos I \\ \sin(nt + \varepsilon) \cos I \\ \sin I \end{pmatrix} \quad ,$$

(69)

where ξ, η, and ζ are the coordinates of C with respect to the reference frame R_1 fixed in the body (i.e., the centroidal mean moment-of-inertia axis frame); ℓ_i, m_i, and n_i are the direction cosines of reference system R_1 with respect to system R_2 with the ζ axis parallel to the angular-momentum vector; I is the inclination of the orbital plane of the two spacecraft with respect to R_2; and n is the average mean motion of both the DM and the CSM.

The two vehicles did not have the same mean motion; in fact, the DM drifted away from the CSM from 300 to 420 kilometers during the experiment. This secular drift was due in part to the small eccentricity of the orbit, to the gravity-field harmonics, to the different area-to-mass ratios of the two spacecraft, and, possibly, to atmospheric-density variations along the orbit, both known and unknown. To take this secular drift into account, we write

$$n = n^* + \nu \quad , \tag{70}$$

where

$$\nu = \frac{1 \text{ arcsec}}{50000} \times \frac{1}{2} \times \frac{1.20}{6600} \, {}^\circ/\text{sec} \cong 10^{-5} \, {}^\circ/\text{sec} \quad , \tag{71}$$

while

$$n \cong 7 \times 10^{-2} \, {}^\circ/\text{sec} \quad .$$

At this point, for a first approximation, we assume the angle I to be small, and therefore the angular-momentum vector is almost normal to the orbital plane, as planned. We call ρ^* the contribution to the observed direction between the center of phase of the DM transmitting antenna and that of the receiving antenna. We have

$$\underset{\sim}{\lambda} = \begin{pmatrix} \cos \, (nt + \varepsilon) \\ \sin \, (nt + \varepsilon) \\ I \end{pmatrix} . \tag{72}$$

We treat the contributions to ρ^* and $\dot{\rho}^*$ due to ξ, η, and ζ separately and assume that the center of phase is on the ζ axis. For the contribution of

46

ρ_{ζ}^{*} to ρ^{*}, we have the following expression:

$$\rho_{\zeta}^{*} = \zeta[\ell_3 \cos(nt + \epsilon) + m_3 \sin(nt + \epsilon) + In_3] \quad . \tag{73}$$

Since

$$\ell_3 = \sin\theta \sin\phi = \sin(\phi + \psi) \sin\theta \cos\phi - \cos(\phi + \psi) \sin\theta \sin\psi$$

$$= \sin(\phi + \psi) \frac{I_2}{M} \omega_2 - \cos(\phi + \psi) \frac{I_1}{M} \omega_1 \quad , \tag{74}$$

we can use equations (68) for ω_1 and ω_2 and neglect terms in q (which, as we discuss later, should be of the order of 0.01), with the result

$$\ell_3 = I_2 \frac{\omega_{20}}{M} \sin(\phi + \psi) \sin \mu t = I_1 \frac{\omega_{10}}{M} \cos(\phi + \psi) \cos \mu t \quad . \tag{75}$$

After some simplifying manipulation, we arrive at

$$\dot{\ell}_3 = \frac{P + Q}{2} \sin(\phi + \psi + \mu t) + \frac{P - Q}{2} \sin(\phi + \psi - \mu t) \quad , \tag{76}$$

where

$$\frac{P + Q}{2} = \frac{\dot{\phi} + \dot{\psi} + \mu}{2} \left(\frac{C - D}{D}\right)^{1/2} \left[\left(\frac{A}{C - A}\right)^{1/2} + \left(\frac{B}{C - B}\right)^{1/2}\right] \quad ,$$

$$\frac{P - Q}{2} = \frac{\dot{\phi} + \dot{\psi} - \mu}{2} \left(\frac{C - D}{D}\right)^{1/2} \left[\left(\frac{A}{C - A}\right)^{1/2} - \left(\frac{B}{C - B}\right)^{1/2}\right] \quad . \tag{77}$$

Similarly, we have

$$\dot{m}_3 = -\frac{P + Q}{2} \cos(\phi + \psi + \mu t) - \frac{P - Q}{2} \cos(\phi + \psi - \mu t) \quad , \qquad (78)$$

and finally,

$$\dot{n}_3 = \frac{d}{dt} \cos\theta = \left[\frac{C(D - A)}{D(C - A)}\right]^{1/2} \frac{d}{dt} \, dn\, \mu t \quad . \qquad (79)$$

By derivation from equation (73), we have

$$\dot{\rho}_\zeta^* = \zeta \left\{ \dot{\ell}_3 \cos(nt + \varepsilon) + \dot{m}_3 \sin(nt + \varepsilon) + I\dot{n}_3 \right.$$

$$\left. -n[\ell_1 \sin(nt + \varepsilon) - m_3 \cos(nt + \varepsilon)] \right\} \quad . \qquad (80)$$

From equations (76) through (79), we see that $\dot{\rho}_\zeta^*$ has three components, with frequencies of $\overline{\dot{\phi} + \dot{\psi}} + \mu - n$, $\overline{\dot{\phi} + \dot{\psi}} - \mu - n$, and μ, respectively. We can assume that $\overline{\dot{\phi} + \dot{\psi}}$ is equal to $\omega_{30} = \omega_0$, which is constant. Introducing the following notation:

$$\eta^* = \frac{C - D}{D} \quad , \qquad \dot{n}_1 = \left(\frac{A}{C - A}\right)^{1/2} \quad , \qquad \eta_2 = \left(\frac{B}{C - B}\right)^{1/2} \qquad (81)$$

and neglecting small quantities, we get

48

$$a(\omega_0 + \mu - n) = \zeta(\omega_0 + \mu - n) \sqrt{n^*}(\eta_2 + \eta_1) \quad ,$$

$$a(\omega_0 - \mu - n) = \zeta(\omega_0 - \mu - n) \sqrt{n^*}(\eta_2 - \eta_1) \quad , \tag{82}$$

$$a(\mu) = \zeta I \left[\frac{C(D - A)}{D(C - A)} \right]^{1/2} \frac{d}{dt} \, dn \, \mu t \quad .$$

Since I should be less than a few degrees, the μ component should also be small. The largest observed component is $\omega_0 + \mu - n$. We can use equations (82) to determine D, since we have a good estimate of ζ. Then equation (63) gives a good estimate of M, as $\omega_0 = \overline{\dot{\phi} + \dot{\psi}}$ is also pretty well known. We also could have obtained M from equation (62), since we know the frequency $\omega_0 + \mu - n$ and therefore μ, but because η_2 is not very well known, the two values of M would probably not agree.

Rewriting equation (62) in the form

$$\mu = \frac{\pi}{2K} \frac{M}{C} \frac{1}{\eta_2} \left[\frac{C(D - A)}{DA} \right]^{1/2} \tag{83}$$

and using the well-observed ratio μ/ω_0, we can solve for η_2:

$$\eta_2 = \frac{(\pi/2K)[C(D - A)/DA]^{1/2}}{\mu \Omega_0 \{1 + [\epsilon(1 + \overline{\cos \theta})]\}} \quad . \tag{84}$$

We then iterate, using equations (82) and (84), until the solution converges to final values for D and B. For example, using $\omega_0 = 2\pi/72.5$, A = 1089 kg m^2, B = 2348 kg m^2, C = 2588 kg m^2, ζ= 813 millimeters, $\omega_0 + \mu - n = 2\pi/53.9666$ per second, and $\mu/\omega_0 = 0.33879$, we find D = 2557 kg m^2 and B = 2372 kg m^2 after three iterations. We also find k^2 = 0.1255, q = 0.00838, $\sqrt{n^*}$= 0.1101,

$\theta_{min} = 5°.4$, $\theta_{max} = 21°.4$, $\mu = 2\pi/214$ per second, and $\omega_0 - \mu - n = 2\pi/108.88$ per second.

A good check on the observations is given by considering the ratio of the amplitudes from equations (82) at the frequencies $2\pi/108$ and $2\pi/54$. The computed ratio for equations (82) is 3.5, while the observed is 3.8. Considering the observational uncertainty in the component at 108 seconds, the agreement is satisfactory.

Next we consider the component $\dot{\rho}^*_\xi$ of $\dot{\rho}^*$ due to a ξ component of $\underset{\sim}{R}$. We have

$$\rho^*_\xi = \xi \left[\ell_1 \cos (nt + \varepsilon) + m_1 \sin (nt + \varepsilon) + n_1 I \right] \quad . \qquad (85)$$

As a first approximation,

$$\ell_1 = \cos (\phi + \psi) + O(n^*) , \qquad m_1 = \sin (\phi + \psi) + O(n^*) ,$$
$$n_1 = \theta \sin \psi \quad . \qquad\qquad (86)$$

Neglecting small quantities, we obtain

$$\rho^*_\xi = \xi(\omega_0 - n) \cos (\omega_0 - n) t \quad . \qquad (87)$$

Knowing the amplitude of the harmonic component of the tumbling period, we can obtain information on the value of ξ. If all the components with a period of 72.5 seconds, for example, are due to the ξ component (or better, to $\sqrt{\xi^2 + n^2}$, which probably reduces to ξ because $n \ll \xi$), then, from an

observed amplitude of 5.66 mm/sec, we get ξ = 65 millimeters, which seems reasonable. It appears that terms of other frequencies due to the rotational motion of the DM should be negligible if this rigid-body torque-free model reproduces the actual system motion.

Higher harmonics of the tumbling frequency were observed to have substantial amplitudes — in particular, at two and three times the tumbling frequency. The obvious explanation is that the phase pattern of the antenna was the main contributor to this phenomenon. An estimate based on scale-model measurements of the antenna pattern performed at Johnson Space Center supports this explanation of the origin of these harmonics. Naturally, the contribution of this factor to the fundamental frequency cannot be distinguished from the contribution due to geometrical displacement of the center of phase from the z axis.

2.4.10 Effects of the radiation phase pattern

Let us consider the phase pattern represented as a function $\Phi(\alpha,\delta)$ of right ascension and declination in the R_2 system:

$$\Phi(\alpha,\delta) = \sum_r \left[a_r(\delta) \sin r\alpha + b_r(\delta) \cos r\alpha \right] \quad . \tag{88}$$

The contribution to the phase variation along the line of sight is given by

$$\frac{d\Phi}{dt} = \frac{\partial\Phi}{\partial\alpha} \frac{d\alpha}{dt} + \frac{\partial\Phi}{\partial\delta} \frac{d\delta}{dt} \quad . \tag{89}$$

Now, if we let λ_x, λ_y, and λ_z be the components of the unit vector in the R_1 reference system, then for small I and θ, we have

$$\lambda_x = \cos (\phi + \psi - nt - \varepsilon) \quad ,$$

$$\lambda_y = -\sin (\phi + \psi - nt + \varepsilon) \quad , \tag{90}$$

$$\lambda_z = \theta \sin (\psi - nt - \varepsilon) + I \quad .$$

Then,

$$\cos \delta \cos \alpha = \lambda_x \quad , \qquad \cos \delta \sin \alpha = \lambda_y \quad , \qquad \sin \delta = \lambda_z \tag{91}$$

and

$$\frac{d\alpha}{dt} = \frac{\dot{\lambda}_y \cos \alpha - \dot{\lambda}_x \sin \alpha}{\cos \delta} \quad , \tag{92}$$

$$\frac{d\delta}{dt} = \dot{\lambda}_z \sin \delta - (\dot{\lambda}_x \cos \alpha + \dot{\lambda}_y \sin \alpha) \cos \delta \quad .$$

From equations (90) and (91), we find that δ and α are periodic functions with periods of μ - n and ω_0 - n, respectively.

If we assume that $a_r(\delta)$ and $b_r(\delta)$ are linear functions of δ in the relatively narrow interval of variability that we have, we can use the following notation:

$$a_r(\delta) = a_r^0 + a_r^1\delta \quad , \qquad b_r(\delta) = b_r^0 + b_r^1\delta \quad . \tag{93}$$

From equation (88), we then have

$$\frac{\partial \Phi}{\partial \alpha} = r \sum_r \left[(a_r^0 + a_r^1\delta) \cos r\alpha - (b_r^0 + b_r^1\delta) \sin r\alpha \right] \quad ,$$

$$\frac{\partial \Phi}{\partial \delta} = \sum_r (a_r^1 \sin r\alpha + b_r^1 \cos r\alpha) \quad . \tag{94}$$

By combining equation (94) with equation (92) and substituting them into equation (89), we get additional periodic terms with periods of $\omega_0 - n$, $\omega_0 - \mu - n$, $\omega_0 + \mu - n$, $2(\omega_0 - n)$, $3(\omega_0 - n)$, $\mu - n$, etc., which are amplitude-dependent on the magnitude of the coefficients. This simple analysis explains the presence of the frequency terms $2(\omega_0 - n)$, $3(\omega_0 - n)$, and $\mu - n$.

Finally, it should be pointed out that since $\mu \approx \omega_0/3$, many of the combination frequencies coincide. A careful analysis of the phase diagram may lead to a more precise determination of the frequencies and amplitudes of the main components due to this effect. Certainly, the 36- and 24-second components, as well as the 208-second component, are clearly evident in the power spectrum, although with different reliability in relation to amplitude and with different broadenings of the frequency band.

2.4.11 Conclusions

It is clear from the analyses illustrated herein how important it is to reconstruct accurately the motion of the DM about its center of mass and the shape and orientation of the antenna radiation phase pattern in order

to remove from the raw Doppler data those components that are not gravity-field related. The Doppler accuracy required implies such a detailed reconstruction that even the DM's thermal behavior and its relative lack of rigidity, perhaps due to somewhat loosely clamped parts in its interior, have a substantial effect, capable of jeopardizing the gravity experiment.

The harmonic components that were removed from the raw Doppler spectrum unfortunately fell within the spectral band of the gravity-anomaly-induced signals. Although their removal was fully justified by the fact that they were found to be due to the DM rotational motion, by removing these components we partially affected the detectability of gravity anomalies. Another peculiar occurrence, which is due to the geometry of the DM, is the fact that the precessional period of the DM is almost exactly equal to three times the tumbling period.

3. EQUIPMENT

3.1 Introduction

Several pieces of equipment were built for this experiment. A dual-frequency transmitter (Figure 4) and monopole antenna were mounted on the DM; the service module carried a receiver and signal processor (Figure 5), along with a circularly polarized dual-frequency antenna; in the CSM with the astronauts was a pair of small tape recorders that stored the data for postflight analysis.

Special tape-reading equipment was used during prelaunch system tests and for reading the data from the flight tapes. In the latter application, the tape reader was controlled by, and fed data to, a standard commercial minicomputer.

3.2 Transmitter

The transmitter, weighing about 7 kilograms, consisted of a highly stable crystal oscillator, frequency multipliers, amplifiers, and a diplexer, the last of which combined the two frequencies for transmission from a single antenna. A block diagram of the transmitter is shown in Figure 6. To save battery power for the operational phase of the experiment, the transmitter was powered directly from the spacecraft during the 50-hour warmup period required by the oscillator. The frequency of the oscillator was set for 5.06 megahertz. Its excellent

BATTERY

DUAL
FREQUENCY
MULTIPLIER

CRYSTAL
OSCILLATOR
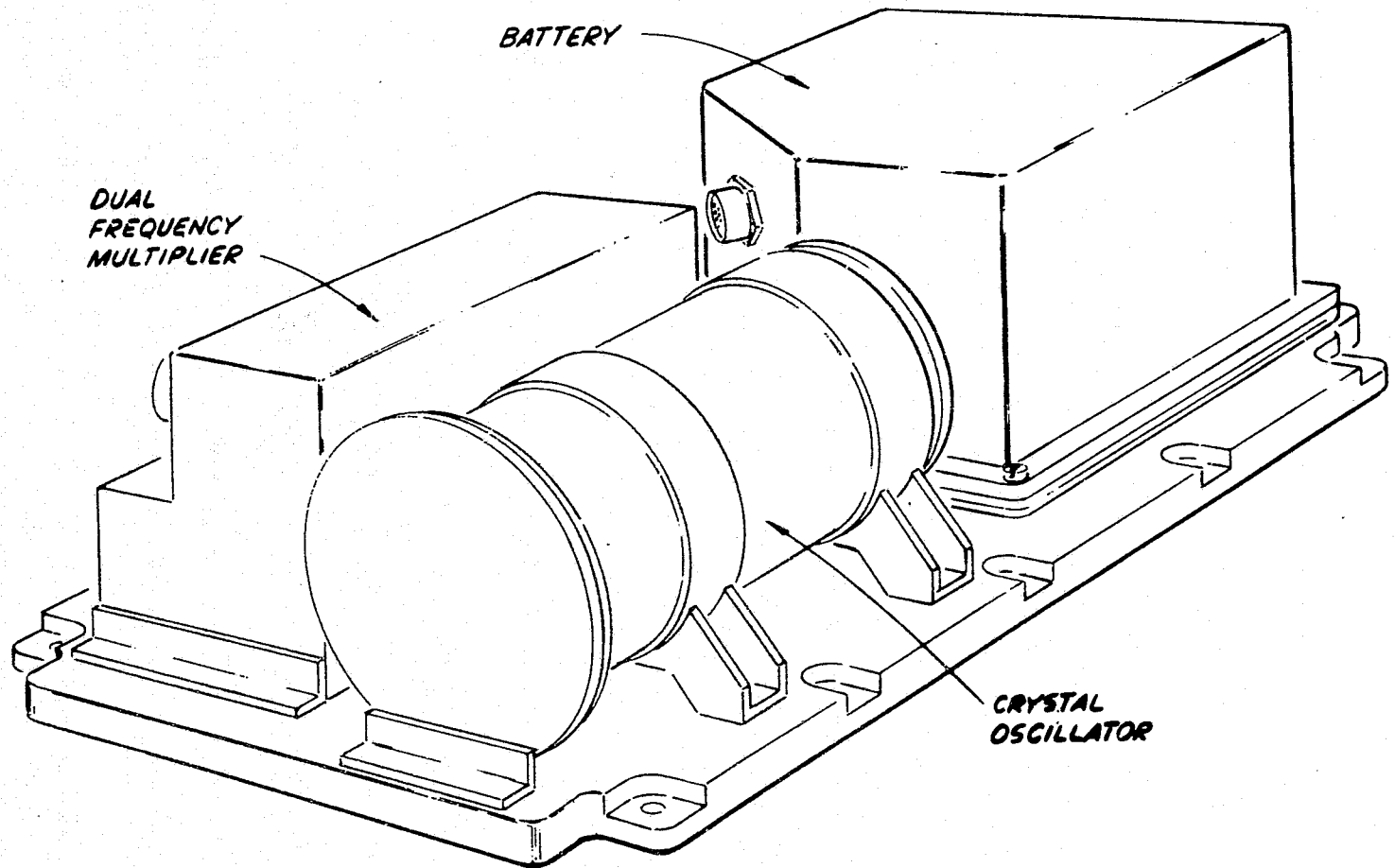
Figure 4. Artist's sketch of the transmitter.

RECEIVER
ELECTRONICS

CRYSTAL
OSCILLATOR

COLD RAILS &
MOUNTING BRACKET
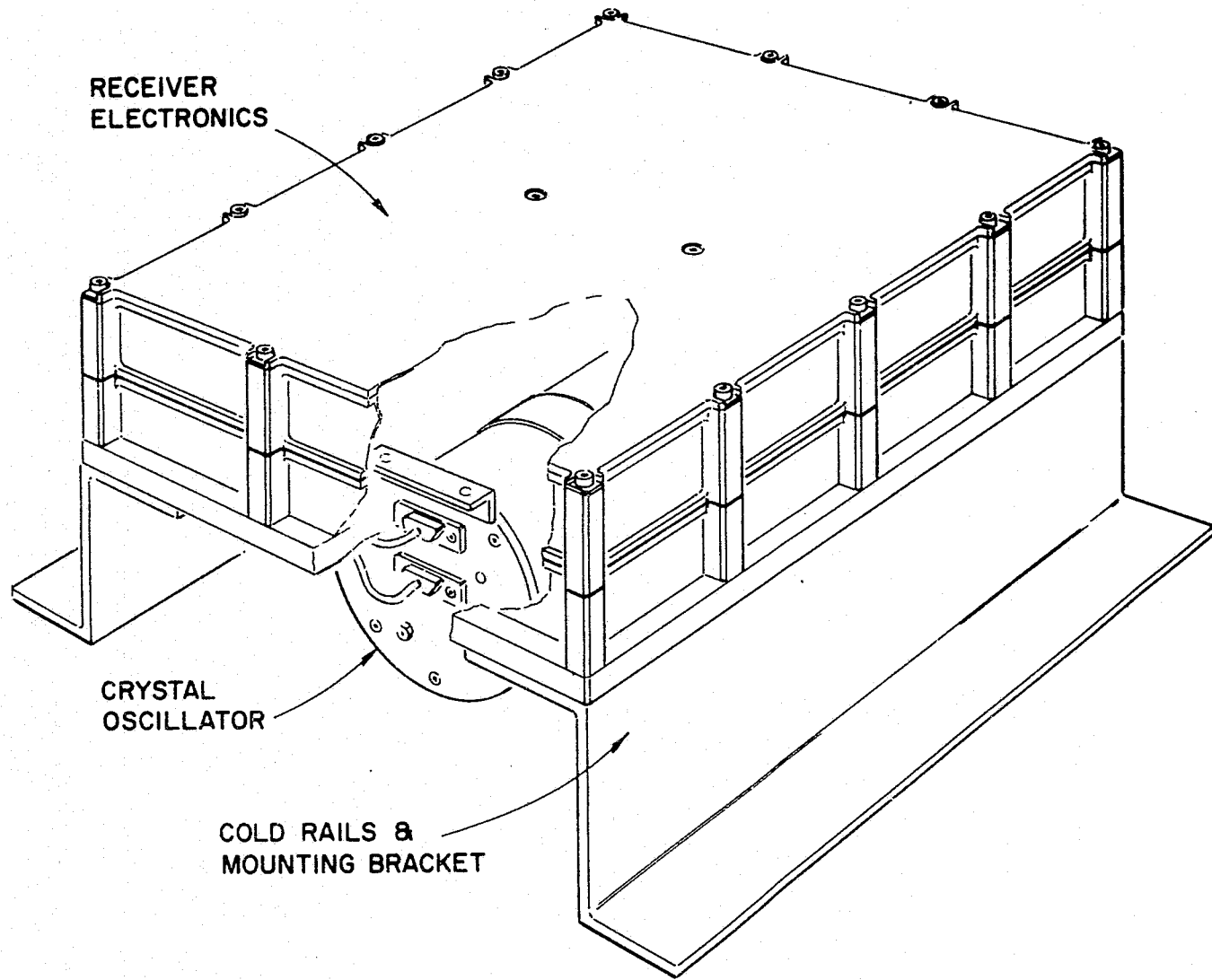
Figure 5. Artist's sketch of the receiver.
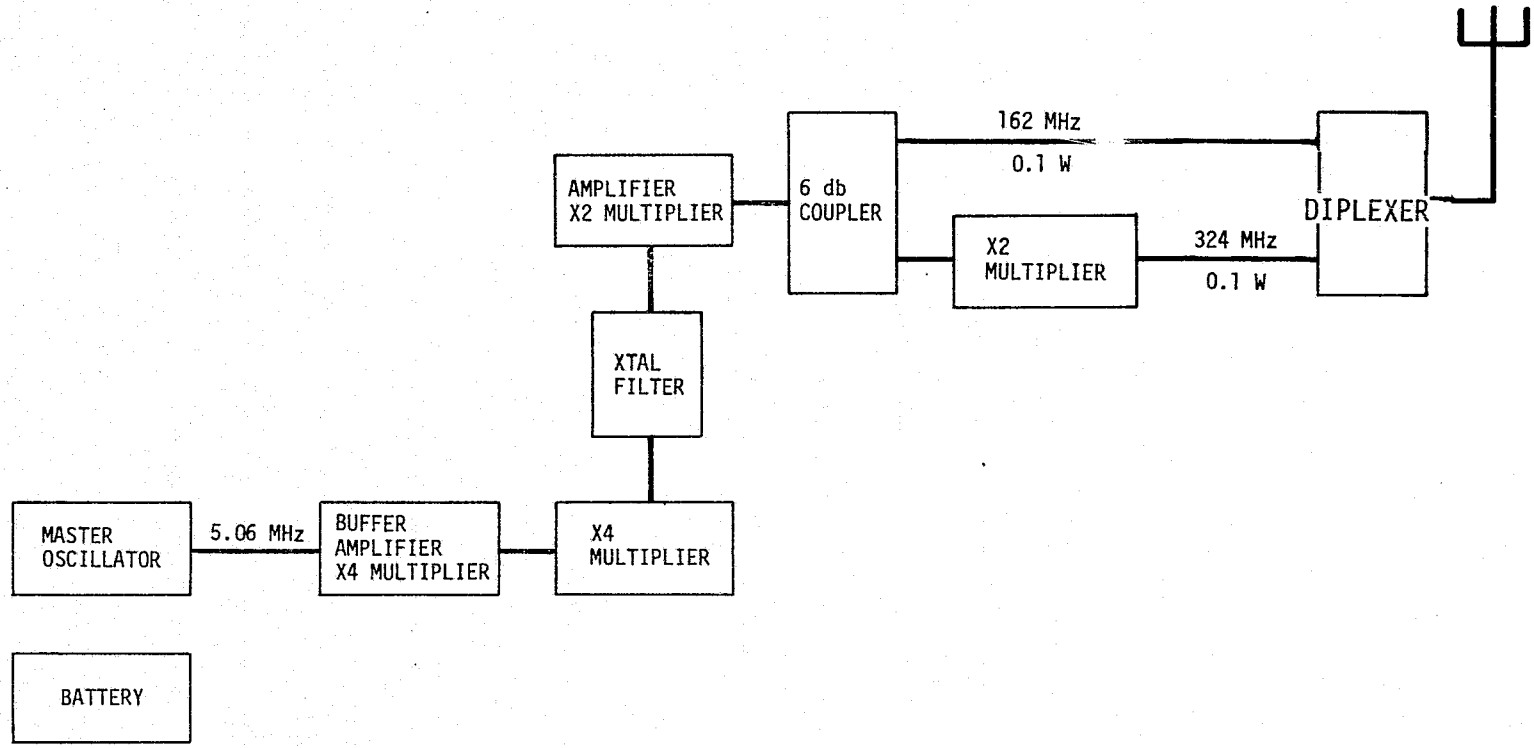
Figure 6.   Block diagram of the transmitter.

stability (1.5 parts in 10^{12} over both 10- and 100-second averaging intervals), as can be seen in Figure 7, was preserved by carefully insulating it from environmental changes over a temperature range of 0 to 100°F. A single multiplier chain multiplied, amplified, and filtered the oscillator output and drove a power divider. One of the power-divider outputs drove the 162-megahertz input of a diplexer; the second was frequency-doubled and was used to feed the 324-megahertz diplexer input. The diplexer provided input isolation and filtering. At least 100 milliwatts of output power was delivered to the dual-frequency antenna at each of the two frequencies.

3.3 Receiver and Signal Processor

The receiver, which also weighed about 7 kilograms, is shown in block-diagram form in Figure 8. It provided the processor with Doppler output compatible with transistor-to-transistor logic for each input frequency, retaining the frequency and phase variations of the 162- and 324-megahertz inputs through the use of second-order phase-lock loops. Thus, the receiver outputs were actually bandpass-filtered and constant-amplitude replicas of the input signals, translated from 164 and 324 megahertz to 1 kilohertz. The choice of 1 kilohertz as the center frequency for the processor represented a compromise between a desire for high accuracy (requiring a low frequency) and the need to avoid the ambiguity that could result if the Doppler signal shifted this frequency negatively by more than 1 kilohertz. Since the maximum anticipated Doppler shift was of the order of 350 hertz, a 1-kilohertz center frequency left an adequate margin without significantly degrading the attainable measurement accuracies.
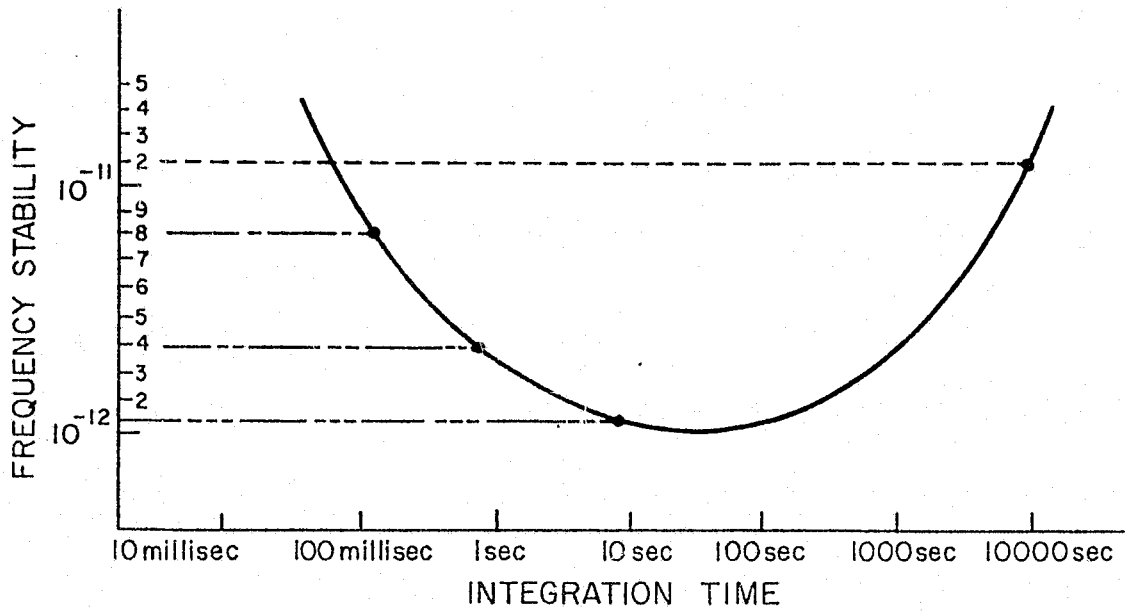
Figure 7. Curve of the stability of the oscillator used in the ASTP
Doppler-tracking experiment.

61
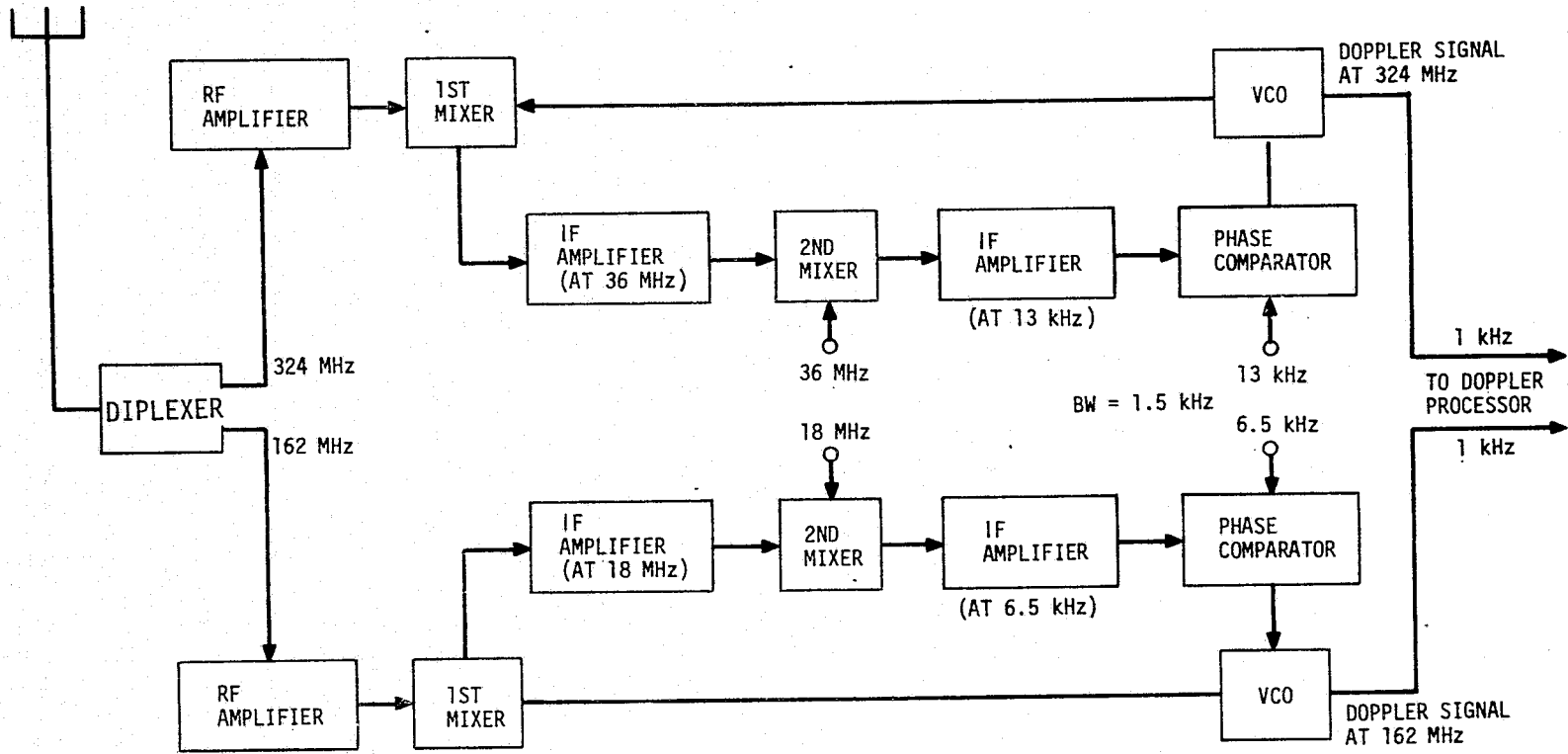
Figure 8. Block diagram of the receiver.

The receiver was powered internally by means of dc-to-dc converters, regulators, and filter circuitry. Less than 50 watts of spacecraft power was needed to operate both the receiver and the tape recorder.

Both the transmitting and the receiving antennas were dual-frequency units. The former was a vertical monopole that acted as a quarter-wave antenna at 162 and at 324 megahertz. At 324 megahertz, an inductor near the midpoint of the antenna isolated the top section from the bottom, while at 162 megahertz, the inductor acted as a small loading coil. The receiving antenna was about 1 meter square and was contoured to fit against the side of the service module. This antenna was a strip-line conformal array, using tuned stubs to couple its sections at 162 megahertz and to isolate the sections at 324 megahertz.

A 5.0-megahertz reference-frequency input to the synthesizer and the timing reference for the Doppler processor were supplied by an oscillator that was identical, except for its frequency, to that in the transmitter. The synthesizer, whose output frequencies, derived by frequency multiplication and division, were phase coherent with the reference, provided all local-oscillator injections and phase-detector references. When required, bandpass filters were used to obtain outputs of sufficient spectral purity.

A diplexer at the receiver input divided the single input from the dual-frequency antenna into two channels. A preamplifier and a mixer followed the diplexer. These stages had a noise figure of less than 8 decibels and a first intermediate-frequency (IF) image-rejection capability of greater than 60 decibels. For each channel, at least 60 decibels of second IF image rejection was achieved by means of a crystal filter. The first IF included two automatic-gain-

controlled stages, and the second, four active filters with amplitude limiting at each stage. The second IF amplifier was followed by sine and cosine phase detectors and filters, the first developing the loop filter voltage fed to the voltage-controlled oscillator (VCO) and the second providing both the automatic-gain-control voltage for the first IF and a lock/out-of-lock signal to the Doppler processor. The VCO module output fed to the first mixer was derived by multiplying and filtering the output of a crystal VCO having a frequency of 22.5 megahertz.

When an out-of-lock signal was received, the processor responded by supplying the phase-detector module with one signal to change the phase-lock-loop bandwidth from 5 to 100 hertz and another to inject a sweep voltage into the loop. The difference between the sweep (± 5 and ± 2.5 kilohertz at 324 or 162 megahertz, respectively) and the expected Doppler shift allowed for changes in the oscillator's central-voltage-to-frequency transfer characteristics. When lock was acquired, the signal voltages changed state, the sweeping voltage was removed, and the loop bandwidth was restored to 5 hertz.

The processor received Doppler-frequency information from the receiver, extracted what was desired, and recorded and stored this information simultaneously on two tape recorders in the CSM, as shown in Figure 9. The Doppler-frequency averaging interval counted by the processor is shown in Figure 10. A 10-second counter identified the time instants t_0, $t_2 = t_0 + 9.996$ seconds, $t'_0 = t_0 + 10$ seconds, $t'_2 = t_2 + 10$ seconds, etc. The points t_1 and t_3 were determined by the first positive-going zero crossing that occurred after times t_0 and t_2, respectively. For each channel, an associated vernier up/down counter
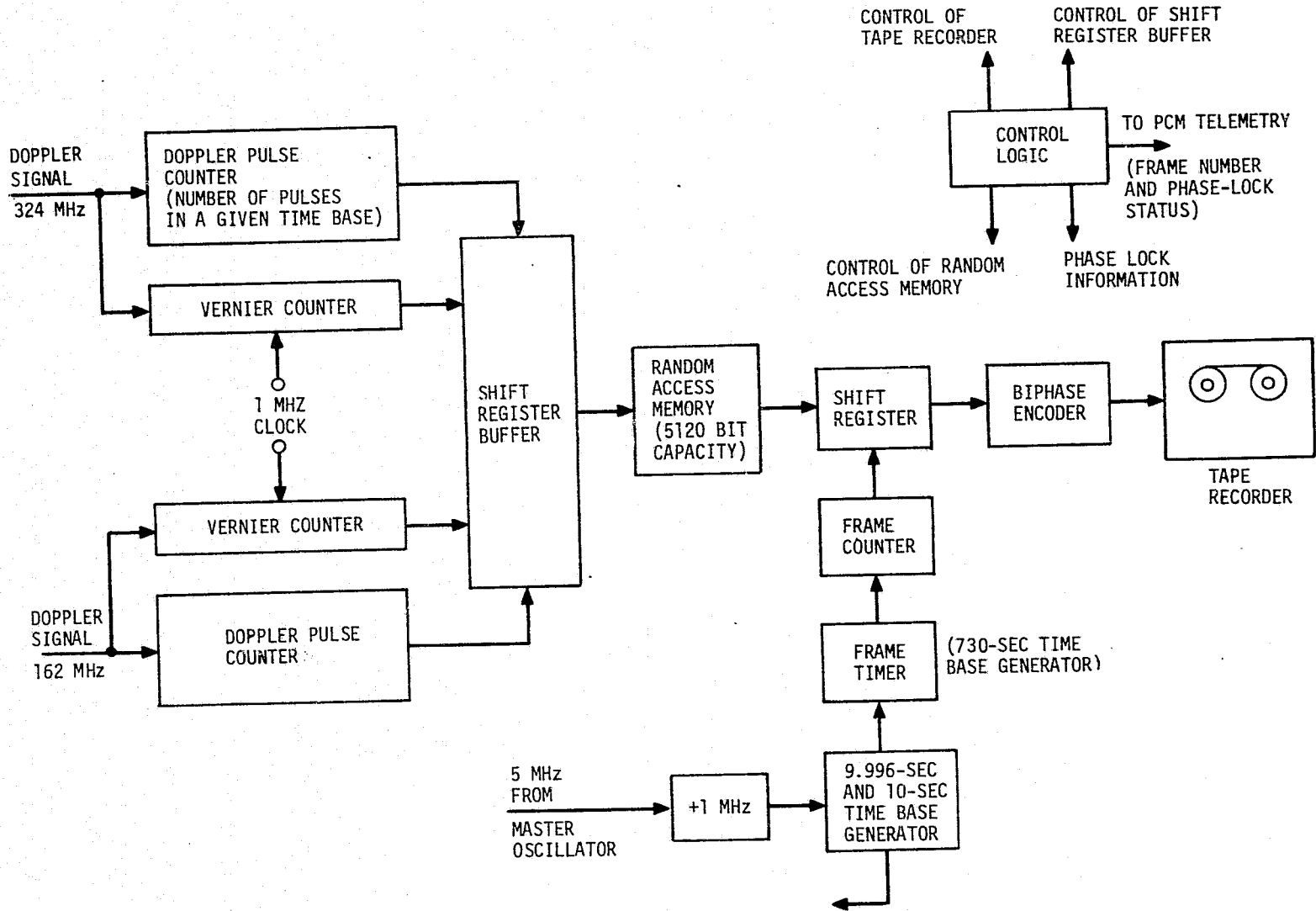
Figure 9. Block diagram of the Doppler processor.
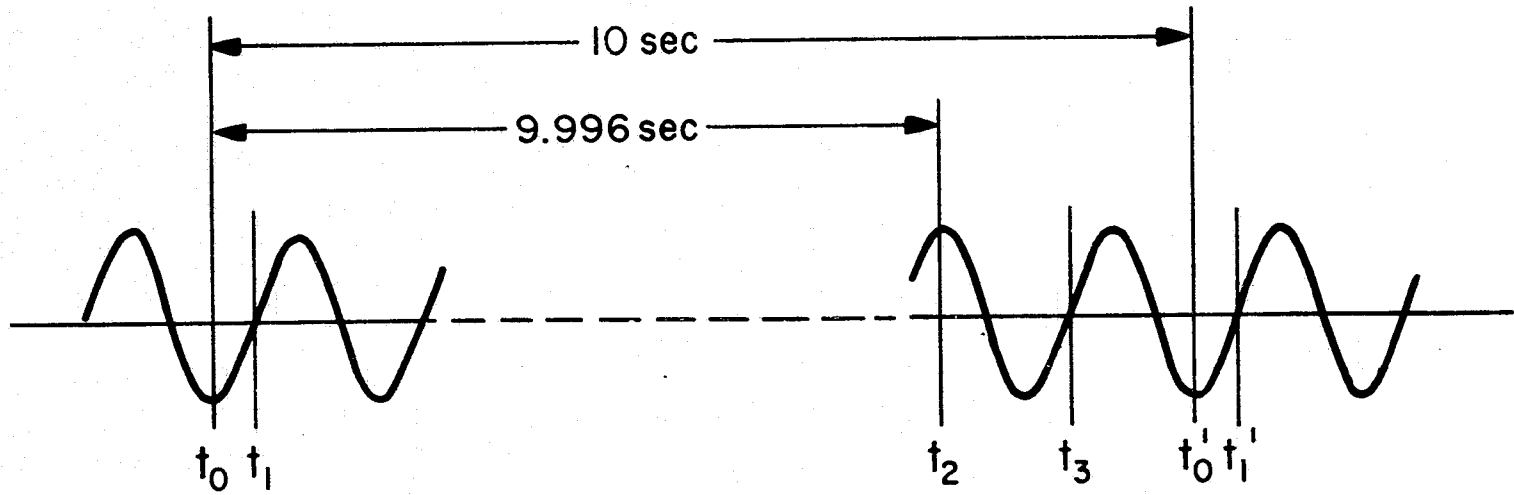
Figure 10.   Counting interval of the Doppler processor.

was enabled at time t_0 and counted the number of 1-microsecond clock pulses observed before it was disabled at time t_1. It was again enabled at time t_2, when it down-counted the number of clock pulses in the interval $t_2 - t_3$. Simultaneously, zero-crossing counters counted the number of positive-going zero crossings in the interval $t_0 - t_2$ for each channel. These time counts and zero-crossing counts constituted the raw data associated with each observation interval. The counters were reset and the whole process began again at time t_0'.

The average frequency $\hat{f}$ observed during a processor cycle was determined from these tape-recorded data by dividing the number of zero crossings Z by the observation time:

$$\hat{f} = \frac{Z}{9.996 - \Delta t} \quad , \tag{95}$$

where Δt is the contents of the vernier counter. Since the zero-crossing counters and the vernier counters were 15 and 13 bits wide, respectively, an unambiguous measurement of any Doppler frequency shift less than or equal to ± 750 hertz was ensured.

The Doppler processor also performed other functions. For example, it monitored lock/out-of-lock signals from the receiver; when an out-of-lock condition occurred, the processor reestablished lock status and loaded out-of-lock data into a format that could be detected during subsequent data reductions. In addition, the Doppler processor supplied high-channel phase-lock status information to the astronauts via a panel meter and that information plus frame numbers to telemetry. From this phase-lock status information, spacecraft maneuvers could have been directed in order to regain high-channel lock if required (we assumed that a high-frequency channel lock implied a low-frequency

66

lock because of the higher signal-to-noise ratio on the low channel). From the telemetered frame number, the tape-recorded data were correlated with the position of the CSM/DM pair relative to the Earth. In another function, data on pitch, roll, and yaw of the CSM were received by the processor and tape-recorded, enabling the effect of the CSM's motion on the Doppler shift to be compensated for during data reduction. Finally, 7-bit parity words were generated by the processor as a protection against substitution and synchronization errors.

Every 10 seconds, a data word was formated by means of a random-access memory, shift registers, a frame counter, and a microprogramed controller. This data word consisted of the number of zero crossings and the Δt values for both the low- and the high-frequency channels, plus information on roll, pitch, and yaw rates and parity. After 73 words were stored as a frame, the frame number was appended and the data were serially transferred to the tape recorders through a biphase encoder at a bit rate of 972 hertz. Approximately 5.2 seconds of recording was required per frame.

3.4 Tape-Reading Equipment

The equipment for reading the tapes consisted of a modified Nagra SN-S tape recorder, used as a tape drive and preamplifier, and a specially designed tape reader that converted the Manchester biphase signals on the data tapes into a binary bit stream for digital-computer processing. For system checkout and a quick look at selected data, the tape reader also drove a device called the serial display unit. These components are shown in Figure 11. The tape reader was
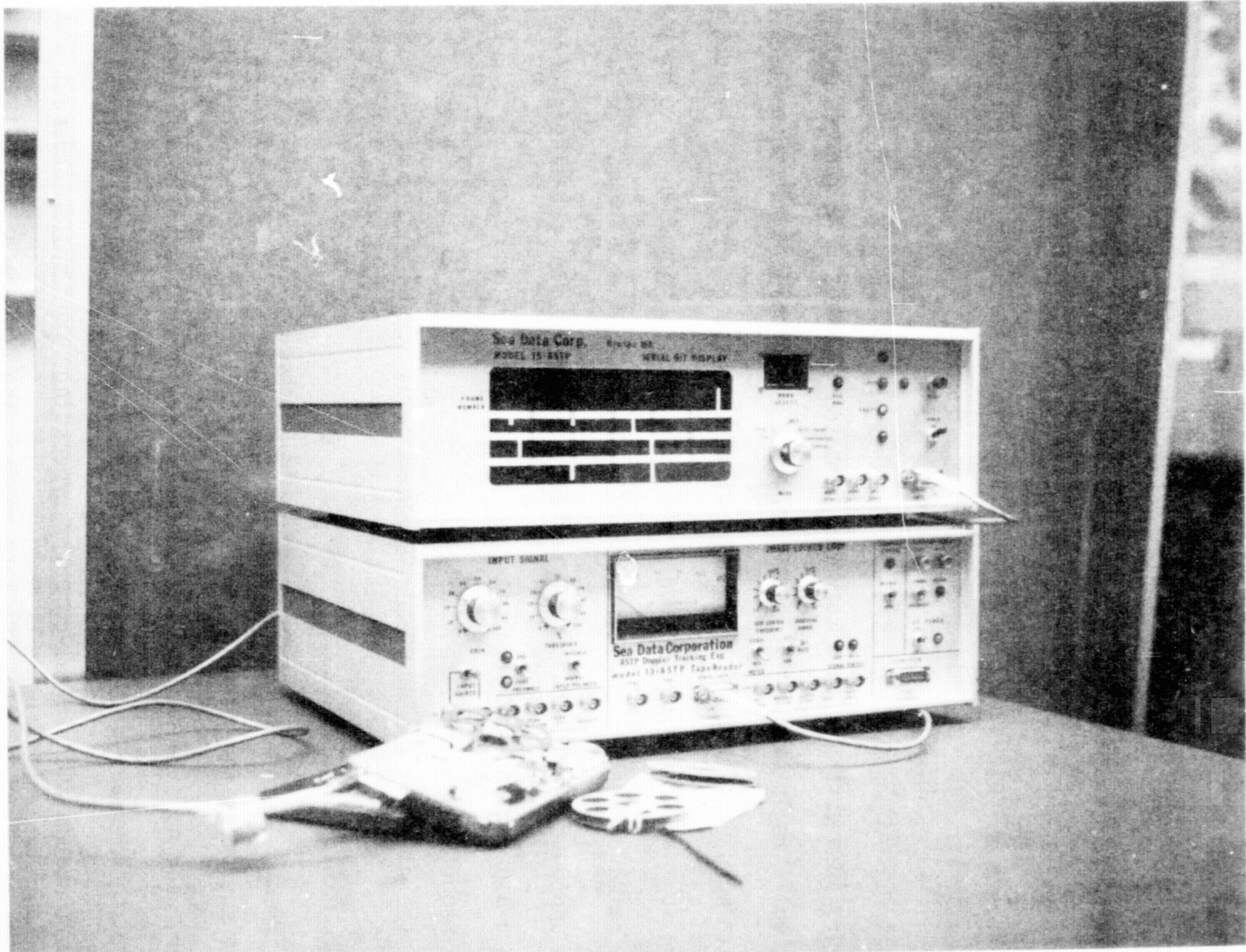
Figure 11.   Tape reader and serial display.

designed to accept input either from the recorder or directly from the drivers in the Doppler processor if needed during prelaunch testing.

The portability of the equipment made it possible to read tapes immediately during testing, both while the receiver was being built in Massachusetts and while the flight equipment was being installed in Florida.

The reading equipment was used again during postflight for a quick readout of the flight data tapes to verify that the data had in fact been recorded. The tapes were then hand-carried to SAO for analysis.

Typical flux and voltage waveforms from the recorder are shown in Figure 12. In practice, the flux did not have the sharp corners shown, since the tape acted as a low-pass filter.

The tape reader incorporated both flux- and phase-decoding circuits, plus logic circuits that provided power to the recorder for automatic frame advance under computer control. Additional features included threshold and gain control, a differential input preamplifier, a level meter, and a signal-monitor output. Transistor-to-transistor logic drivers simplified the interface with the computer.

Figure 13 is a block diagram of the essential components of the tape reader. The input signal V_s, the derivative of the flux, represents the voltage waveform from the recorder playback head. This signal was fed both to threshold
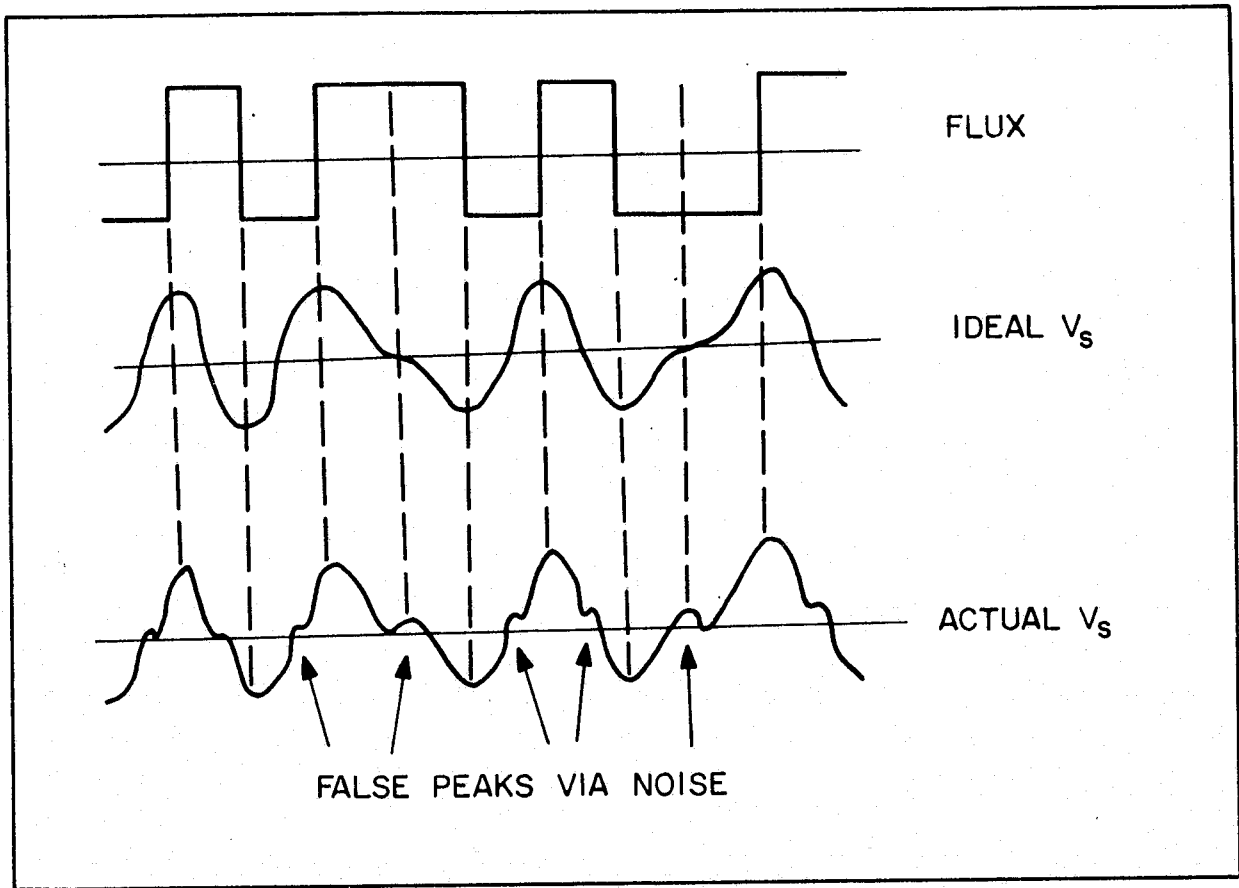
Figure 12. Typical flux and voltage waveforms from the recorder.
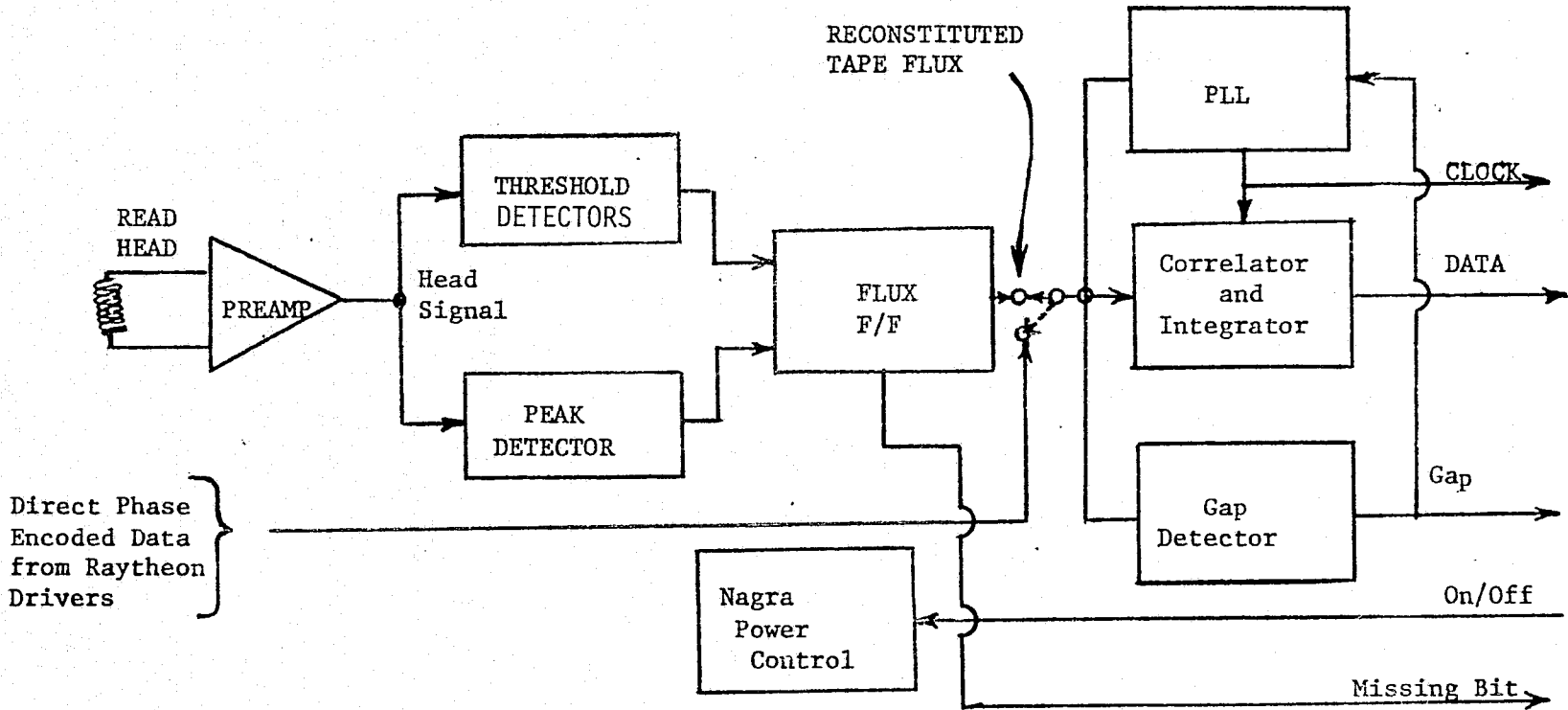
Figure 13. Block diagram of the tape reader.

detectors, which identified positive and negative flux transitions, and to a
peak detector, which pinpointed these transitions more precisely in time.

The threshold detectors rejected any noise that had the appearance of
intermediate peaks (see Figure 12). Since the detectors were biased at +V and
-V, respectively, as shown in Figure 14, both V_+ and V_- were zero when $|V_s|$ did
not exceed $|V|$. A positive peak of V_s exceeding +V in magnitude resulted in
a positive pulse in V_+, while a negative peak exceeding -V gave a pulse in V_-
(see Figure 15). Positive peaks in V_s occurred in the neighborhood of negative-
to-positive transitions of flux, and vice versa.

The peak detector utilized the fact that the first time derivative of V_s
was zero at its peaks. The signal V_s was input to a differentiator; its out-
put, V_d, was then fed into a zero-crossing detector, which resulted in the sig-
nal V_h. The transitions of V_h corresponded to the peaks of V_s. To locate
these transitions, V_h was input to an edge detector; the output, V_p, which was
zero except during transitions of V_h, was used as a clock pulse to set and re-
set the flux flipflop according to whether the output of the threshold detector
was positive or negative. The output of the flipflop thus became the recon-
structed tape flux. The logic has reproduced an electrical signal that has
duplicated the flux itself as closely as possible. Figures 14 and 15 show this
in more detail.

To transform the reconstituted flux into binary data, a clock signal de-
lineating each bit cell was generated from a phase-lock loop circuit with a VCO
and a phase detector. The detector produced a voltage proportional to the dif-
ference in phase of the flux and the VCO. A control on the phase-lock loop set
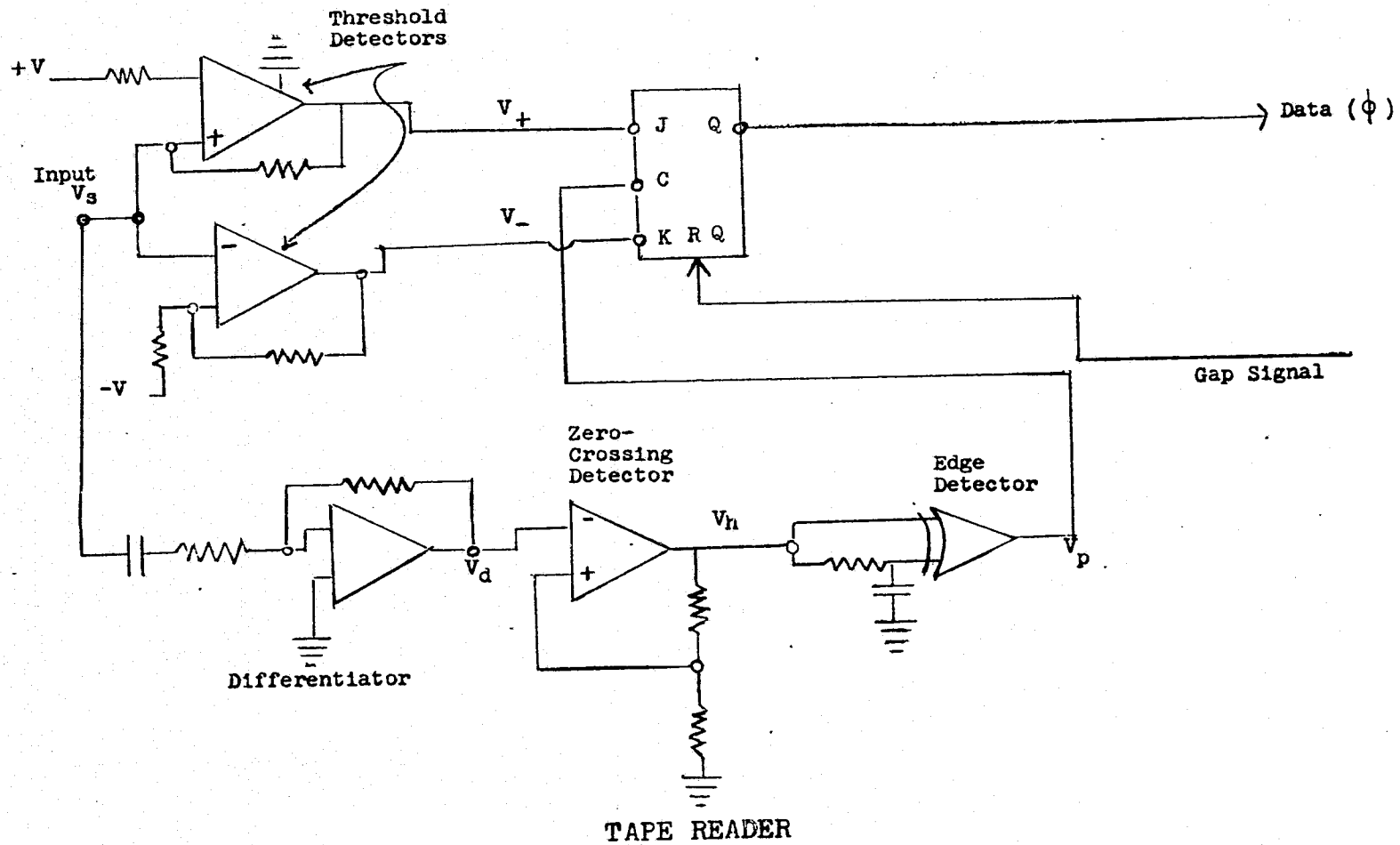
Figure 14. Partial schematic diagram of the tape reader.
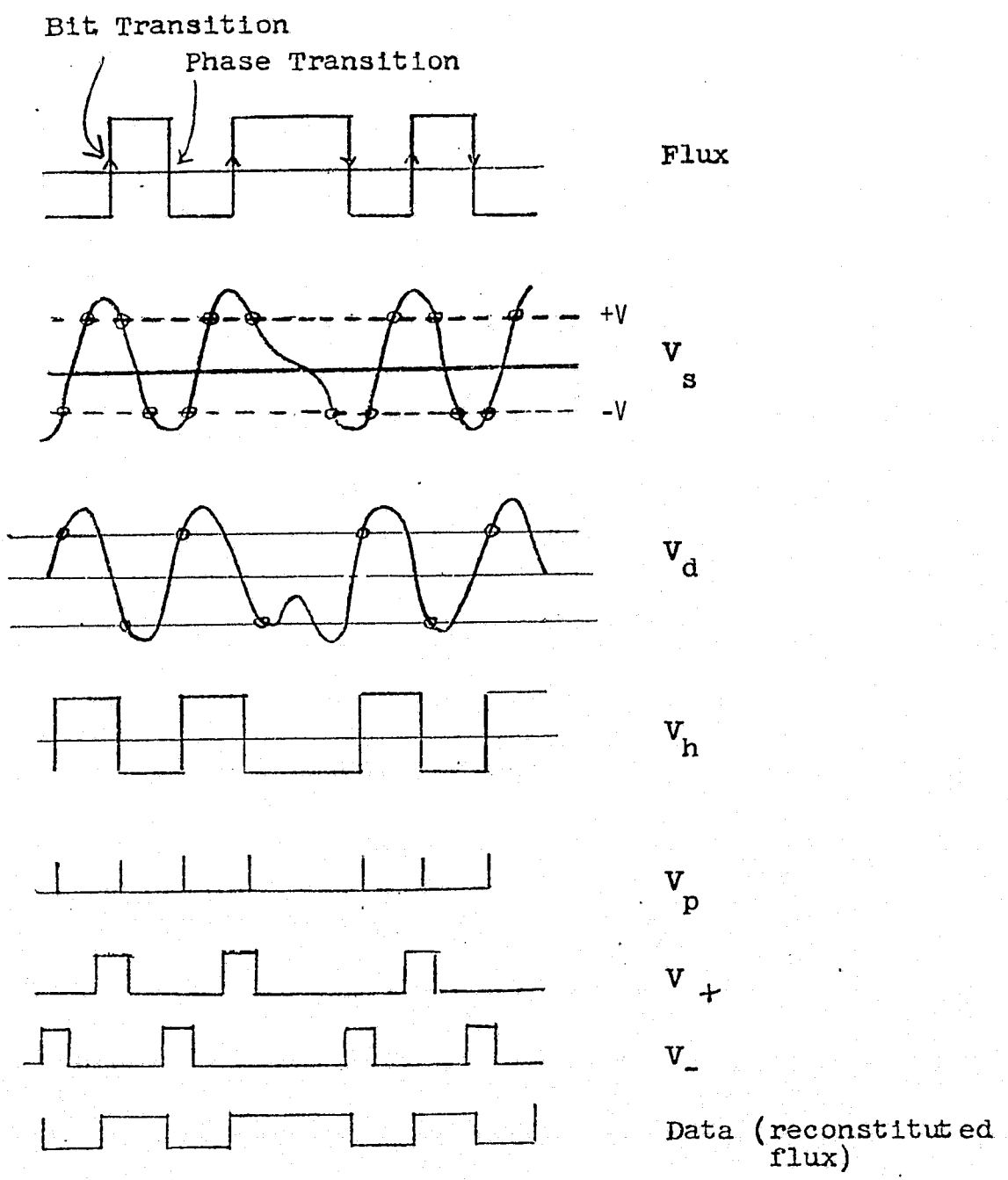
Figure 15. Flux and tape-reader signals.

the center frequency of the oscillator during gaps when no signal was present for the phase detector. Loop synchronization occurred at the beginning of each frame by detecting the most significant bit of the frame number (first out) and by using the signal to start the VCO divider. Throughout the remainder of the frame, the VCO tracked the frequency and phase of the flux signal. The phase-lock loop was designed not to lose sync if a bit was missing.

The negative-going transitions of the clock signal defined the individual bit cells. The flux and clock signals were exclusive-or'd together to get the output signal DATA. To improve the signal-to-noise ratio of this serial-bit stream, DATA was integrated separately over each bit cell, with positive values represented by 1's and negative values by 0's. These processes are indicated schematically in Figure 16. From these methods, data with a time jitter of up to 40% could be decoded. This information was used to load a buffer, whose contents were then clocked out to the computer interface or serial display unit at the appropriate time. The outputs of the tape reader were clock or interrupt signals, binary digits, and gap and missing-bit signals.

For on-line system checkout or a quick look at the data, the serial display unit was connected to the tape reader (Figure 17). On the serial display unit, an 8-bit unit showed the frame number, and an 87-bit unit served as a movable window for examining any selected word of the frame. The serial display unit was also equipped with logic to generate and check the cyclic redundancy check from the data stream.
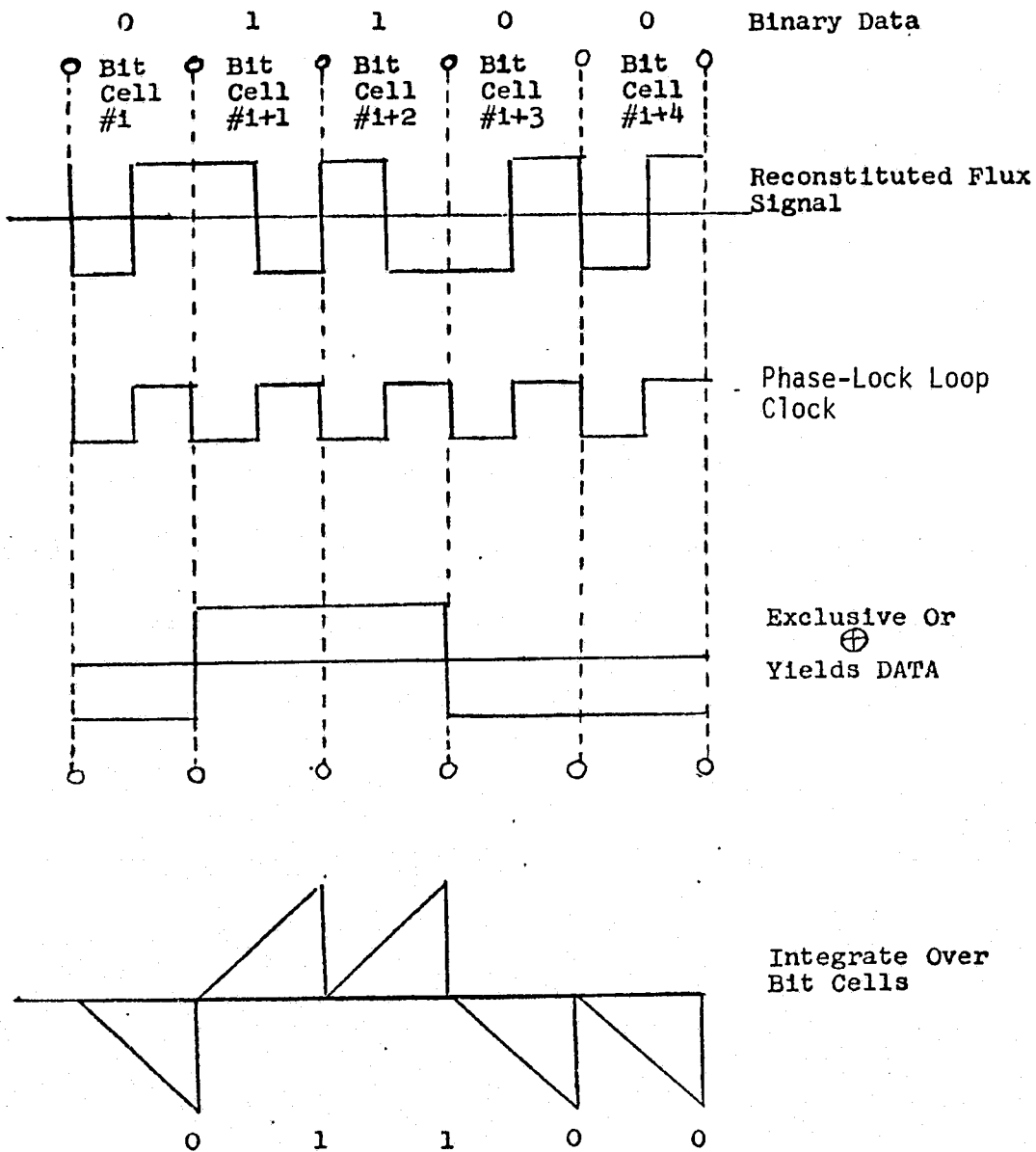
Figure 16. Converting reconstituted flux to data.
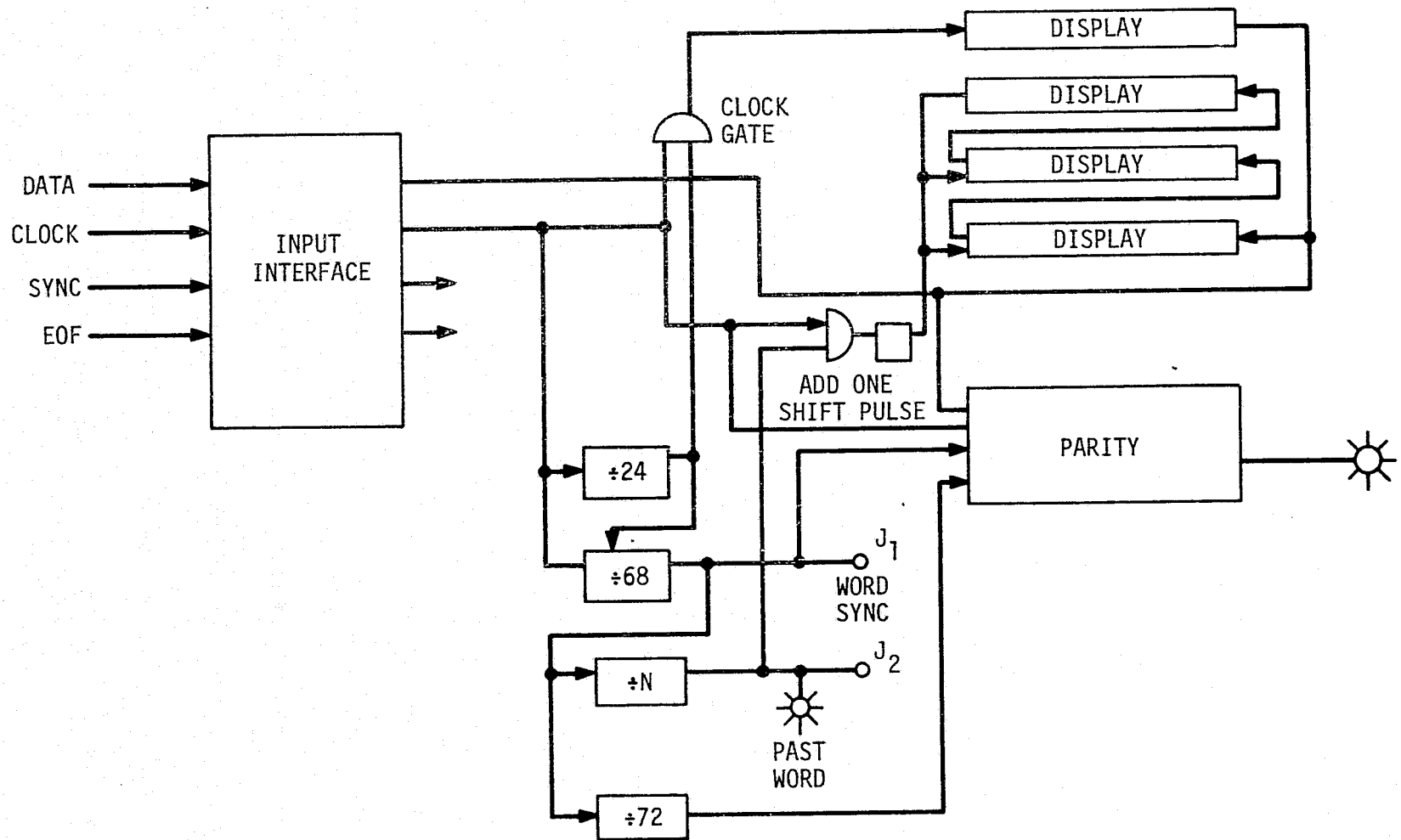
Figure 17. Block diagram of the serial display unit.

A Data General Nova 1200 minicomputer formated the data from the tape reader and stored it on an industry-compatible magnetic tape for use by SAO's CDC 6400 computer. This necessitated the interface between the tape reader and the minicomputer shown in Figure 18. The interface contained the usual interrupt logic, device-selection network, intermediate transfer registers, and input/output data lines.

3.5 Testing

The system was tested for oscillator stability and low noise before the flight by observing the 10-second integrated-frequency measurements produced by the signal processor. The interval during the flight between turn-on and DM jettison also provided a measurement of system performance. On the ground or when the two spacecraft were docked, neither Doppler shift nor ionospheric effects are possible. Thus, the time variation in the sequence of frequency measurements at each frequency measured the stability of the transmitter oscillator relative to that of the receiver oscillator. The difference between simultaneous 324- and 162-megahertz observations tested the balance of the circuitry.

Table 1 gives the root-mean-square (rms) scatter among a small sample of data points observed at factory acceptance testing, at Kennedy Space Center before the equipment was installed, on the launch pad, and finally in orbit. In the first two tests, the backup transmitter was used; the flight system noise in the pad test was attributed to the fact that insufficient time had been allowed for the oscillators' temperature-controlled crystals to stabilize.
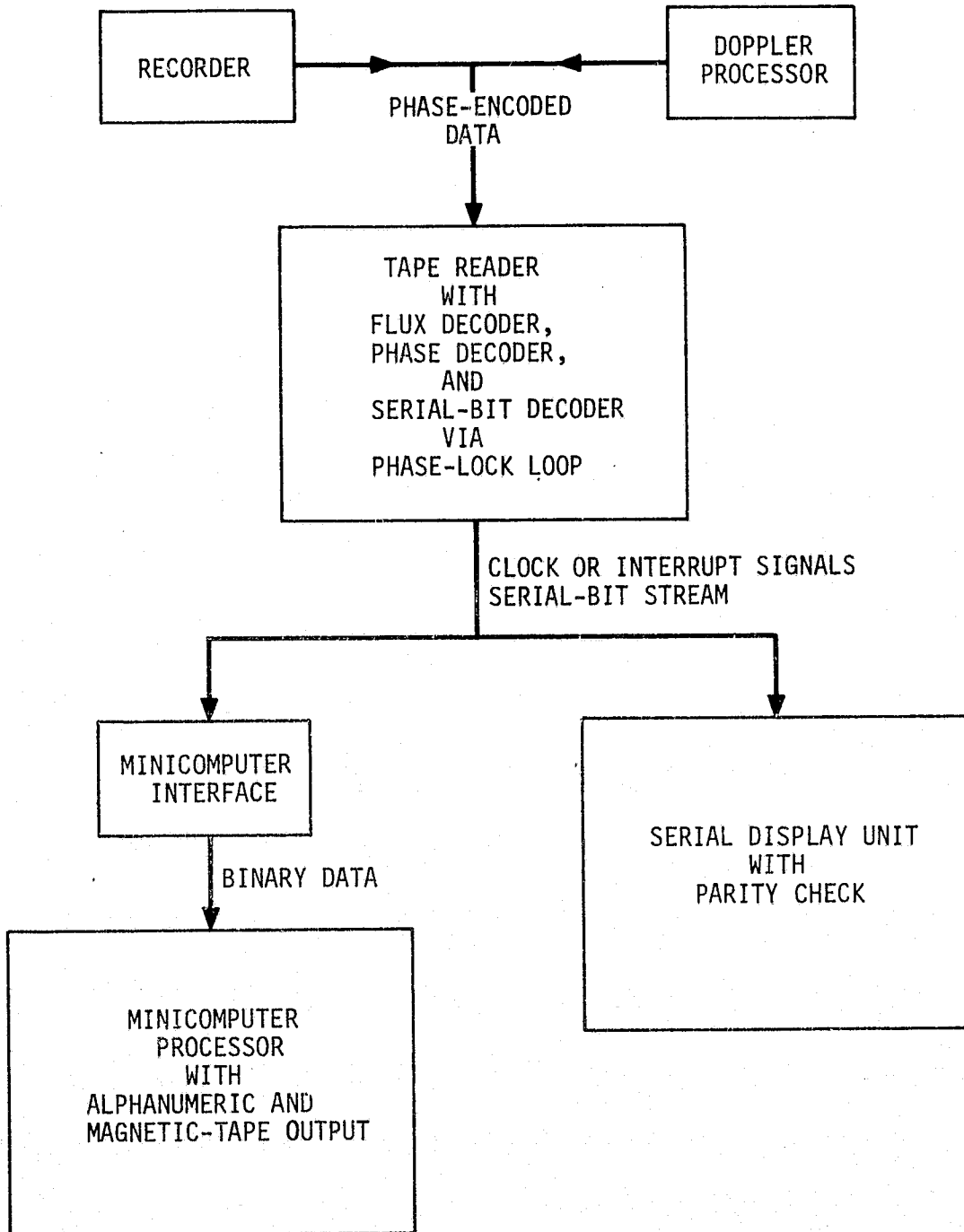
Figure 18. Interconnection diagram for tape reader, serial display unit, and minicomputer.

Table 1. Root-mean-square scatter during testing.

| | Scatter | |
	162 MHz (mm/sec)	324 MHz (mm/sec)
Test		
Acceptance	4.2	0.9
Preinstallation	1.0	1.2
Pad	3.7	3.5
Orbit	1.8	1.8

The rms calculated for the entire "orbit" data set differs somewhat from the tabulated value since it includes longer term fluctuations and the frequency shift induced by g-loading the crystals when the CSM and DM were rotated at $5°$/sec just before separation. The rms difference between channels during this time (based on a small sample) was 1.4 millihertz.

4. DATA

4.1 Introduction

The experiment utilized three prime sources of data: spacecraft-to-space-craft Doppler data and related information recorded in the command module; ground tracking data from NASA's unified S-band (USB) network, the Defense Mapping Agency's Tranet Doppler tracking network, and a number of geoceivers coordinated by the Applied Physics Laboratory; and telemetry from the CSM showing the start of each data frame and a receiver-lock indicator. These are described in more detail in the following sections.

In addition, the astronauts photographed the DM shortly after it was jettisoned from the CSM. Containing about 390 images of the DM taken at approximately 0.5-second intervals, the film was used to make a first estimate of the DM's rotational motion.

4.2 Tape-Recorded Data

The data recorded aboard the CSM were arranged in groups called words, 73 words constituting a frame. The first 8 bits in each frame gave its number, a sequential count that started when the receiver was turned on. The 73 data words followed the frame number; the first word was 87 bits long, and the rest were 69. The composition of the data words is shown in Figure 19. All data
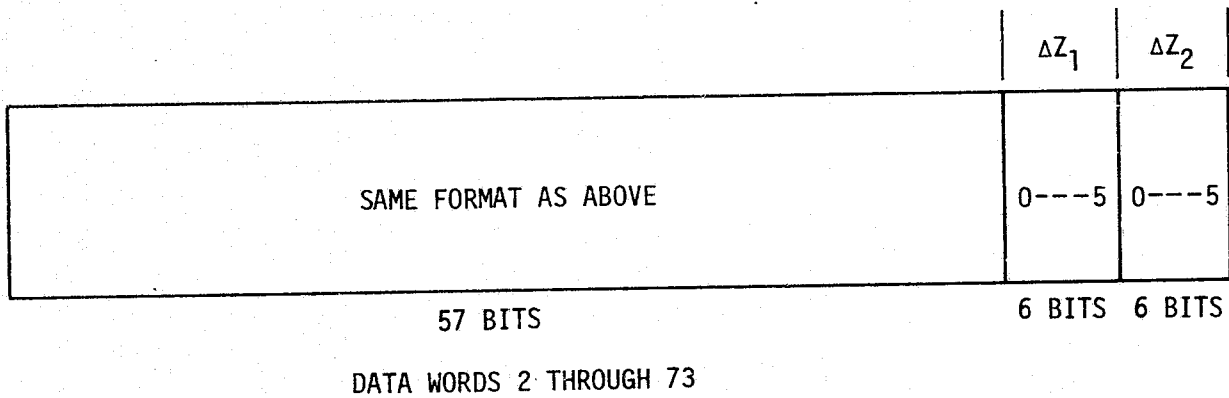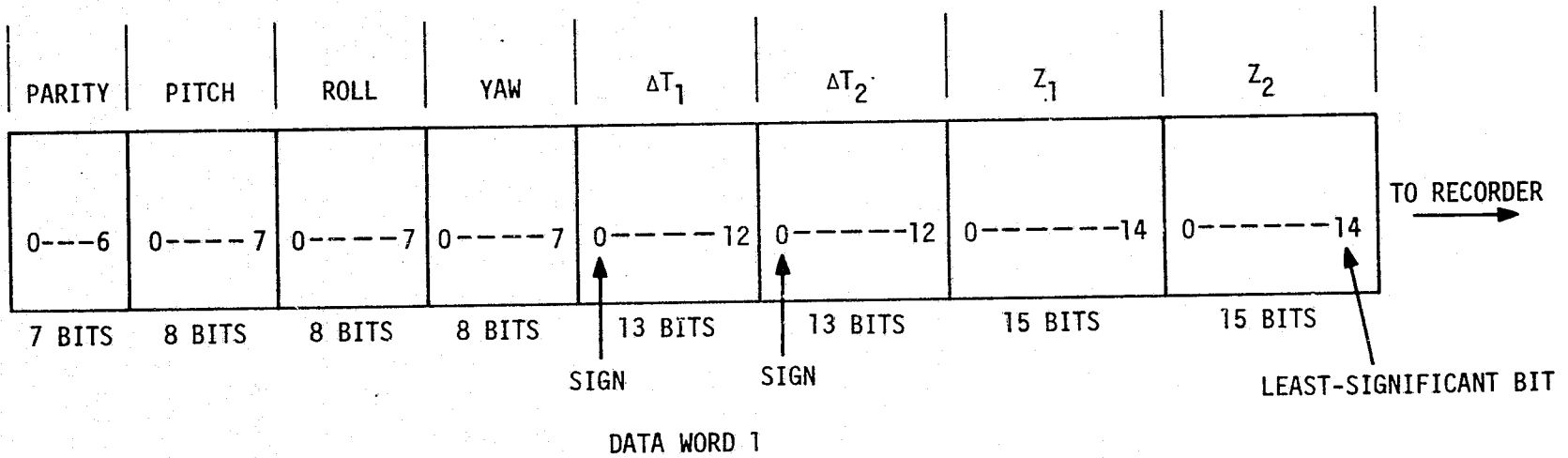
Figure 19. Composition of data words.

groups appeared with the least significant bit first, except for the frame number, which, for reader synchronization, had its most significant bit first, thereby ensuring 127 frames (nearly 26 hours of observing time) wherein the first bit was 0.

In a Manchester biphase code generated by the signal processor, the data were to have been recorded in the CSM on a parallel pair of slightly modified Nagra SN-S tape recorders. One recorder failed to run; postmission investigation revealed that the tape had become stuck to one of the heads. Fortunately, the other tape contained signals of high quality. There were no parity errors and no dropouts.

In all, 109 frames were recorded. Frame 0 contained no useful information and was generated by the signal processor only to ensure that the various registers were correctly set for the start of frame 1. Frames 1 through 15 contained data taken while the CSM and DM were connected and constituted the final test of the equipment. This is discussed further in Section 6. Frames 16 through 41 included the period during which the CSM was maneuvered to attain a position some 300 kilometers from the DM. The observational data began with frame 42, which started at 1:01:56 GMT on July 24, 1975 (204:41:56 GET), shortly after the start of orbital revolution 126. Since the receiver was turned off during frame 109, which was therefore not recorded, the data ended with frame 108, completed at 14:37:06 GMT on July 24, 1975.

The Doppler measurements were continuous except for two gaps due to loss of receiver lock. One occurred in frames 59 through 61, and the other in frames 101 through 103.

4.3 Ground-Based Observations

The CSM was tracked by NASA's USB. Participating stations are listed in Table 2. Eleven stations reported a total of 1754 observations made during 15 passes between 00:43:00 and 15:50:00 GMT. We rejected 832 observations that were made at low elevation angles, 5° being our limit for range measurements and 8° for range differences.

The DM was observed by the Tranet and geoceiver stations listed in Table 2. Between 00:00:00 and 24:00:00 GMT, 216 geoceiver observations were recorded on 46 passes and 928 Tranet observations from 64 passes. From these 1144 observations, 492 were rejected because of elevation angles less than 8°.

4.4 Telemetry Data

For all times when the CSM was within range of a receiving station, the telemetry stream included a signal from the receiver indicating whether or not it was locked onto an incoming signal. Every 12^m10^s, the start of a new frame and its number were indicated. These data, recorded on strip charts along with time signals generated at Johnson Space Center, formed the basis for correlating Doppler data and spacecraft position.

Table 2. Coordinates of participating stations.

Station	X (Mm)	Y (Mm)	Z (Mm)
	USB Stations		
Tananarive, Madagascar	4.0912980	4.4341770	-2.0659249
Rosman, North Carolina	0.6471828	-5.1783358	3.6561424
Fairbanks, Alaska	-2.2825164	-1.4533596	5.7567141
Merritt Island, Florida	0.9070589	-5.5352174	3.0260922
Bermuda, U.K.	2.3084607	-4.8743054	3.3934036
Canary Island	5.4391608	-1.5221214	2.9635383
Ascension Island, U.K.	6.1212275	-1.5633832	-0.8769201
Madrid, Spain	4.8478217	-0.3533416	4.1171222
Guam, M.I., USA	-5.0689162	3.5841270	1.4588852
Kauai, Hawaii	-5.5438459	-2.0545445	2.3877970
Goldstone, California	-2.3547824	-4.6467783	3.6693821
Goddard, Maryland	1.1297785	-4.8331641	3.9921981
Goddard, Maryland	1.1298526	-4.8331663	3.9921850
Goldstone, California	-2.3547314	-4.6467992	3.6693790
Merritt Island, Florida	0.9070634	-5.5352447	3.0260413
Santiago, Chile	1.7698617	-5.0444833	-3.4684266
Orroral Valley, Australia	-4.4474777	2.6768756	-3.6952974
Quito, Ecuador	1.2634111	-6.2550434	-0.0689495

Table 2. (Cont.)

Station	X (Mm)	Y (Mm)	Z (Mm)

<div align="center">Tranet Stations</div>

Station	X (Mm)	Y (Mm)	Z (Mm)
São Jose dos Campos, Brazil	4.0838761	-4.2097874	-2.4991236
Anchorage, Alaska	-2.6561759	-1.5443670	5.5706379
Thule, Greenland	0.5393997	-1.3883791	6.1810430
McMurdo, Antarctica	-1.3107122	0.3104676	-6.2133576
Mahé Island, Seychelle Islands, U.K.	3.6028809	5.2382153	-0.5159373
Las Cruces, New Mexico	-1.5562020	-5.1694430	3.3872475
Howard County, Maryland	1.1226496	-4.8230303	4.0064661
Smithfield, Australia	-3.9422356	3.4588526	-3.6081984
Barton Stacey	4.0050385	-0.0967153	4.9464123
Brussels, Belgium	4.0277388	0.3063822	4.9196078
San Miguel, Philippines	-3.0875510	5.3334541	1.6383241
Guam, M.I., USA	-5.0644095	3.5835906	1.4757010
Tafuna, Samoa Island	-6.0999245	-0.9970790	-1.5687434
Mizusawa, Japan	-3.8572265	3.1086861	4.0038115
Ottawa, Canada	1.1071106	-4.3486527	4.5173736
Pretoria, South Africa	5.0517148	2.7257574	-2.7747748
Austin, Texas	-0.7410434	-5.4569632	3.2071993
Shemya, Alaska	-3.8514456	0.3968759	5.0515397
Cambridge Bay, Canada	-0.5933216	-2.2143062	5.9819756

Table 2. (Cont.)

Station	X (Mm)	Y (Mm)	Z (Mm)
Geoceiver Stations			
Ascension Island, U.K.	6.1193795	-1.5714531	-0.8716983
Olympia, Washington	-2.3355078	-3.6673586	4.6509906
Chagos Archipelago	1.9118888	6.0306800	-0.8068672
Catania, Sicily	4.9013850	1.3075957	3.8533098
La Paz, Bolivia	2.2759558	-5.6811941	-1.8041705
Quito, Ecuador	1.2808306	-6.2509695	-0.0108181
Asuncion, Paraguay	3.0906206	-4.8725149	-2.7093123
Teheran, Iran	3.2349603	4.0503382	3.7062194
Kinshasa, Japan	6.1360700	1.6734471	-0.4828390
Cyprus	4.3499285	2.9043830	3.6380975
Nairobi, Kenya	5.1062448	3.8218350	-0.1469560
Honolulu, Hawaii	-5.5116188	-2.2269531	2.3038805
Calgary, Canada	-1.6596150	-3.6767227	4.9254923

5. DATA REDUCTION

5.1 Introduction

The data-processing phase consisted of a series of computerized steps to remove from the raw data a number of corrupting effects, leaving only random system noise and the "signatures" of gravity anomalies. Both theoretical models and filtering techniques were applied. The procedure involved four basic operations: 1) point-by-point calculation and removal of the ionospheric propagation effects; 2) separate determinations of the orbits of the CSM and DM so that a predicted range difference could be computed for each data point, thereby taking into account all orbital effects including gravitational perturbations (except small-scale anomalies); 3) point-by-point subtraction of the calculated range differences from the observations; and 4) reduction of the rms scatter of the residuals by calculating and subtracting the components arising from rotational motions of the spacecraft.

The ionospheric-correction technique is described fully in refs. 18 and 19 and is simply the classical two-frequency correction that recognizes the frequency-dependent phase shift imposed by the ionosphere. Figure 20 is a sample of the raw data as recorded aboard the CSM, while Figure 21 shows the differential Doppler signal due to the ionosphere. Removal of the ionospheric contributions left the data, as shown in Figure 22, with periodic excursions as large as 3 m/sec.
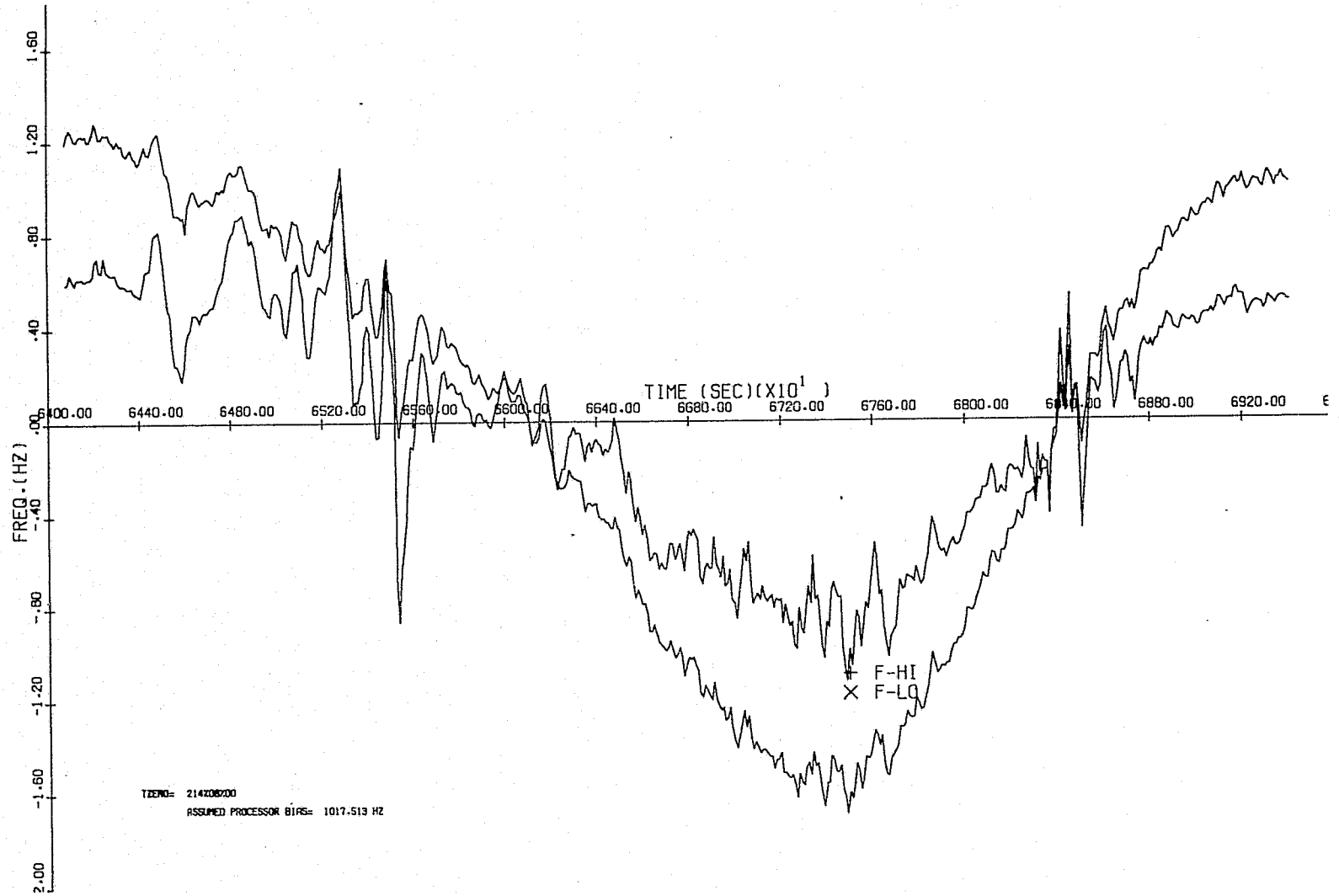
Figure 20. The raw Doppler signal as recorded aboard the CSM.
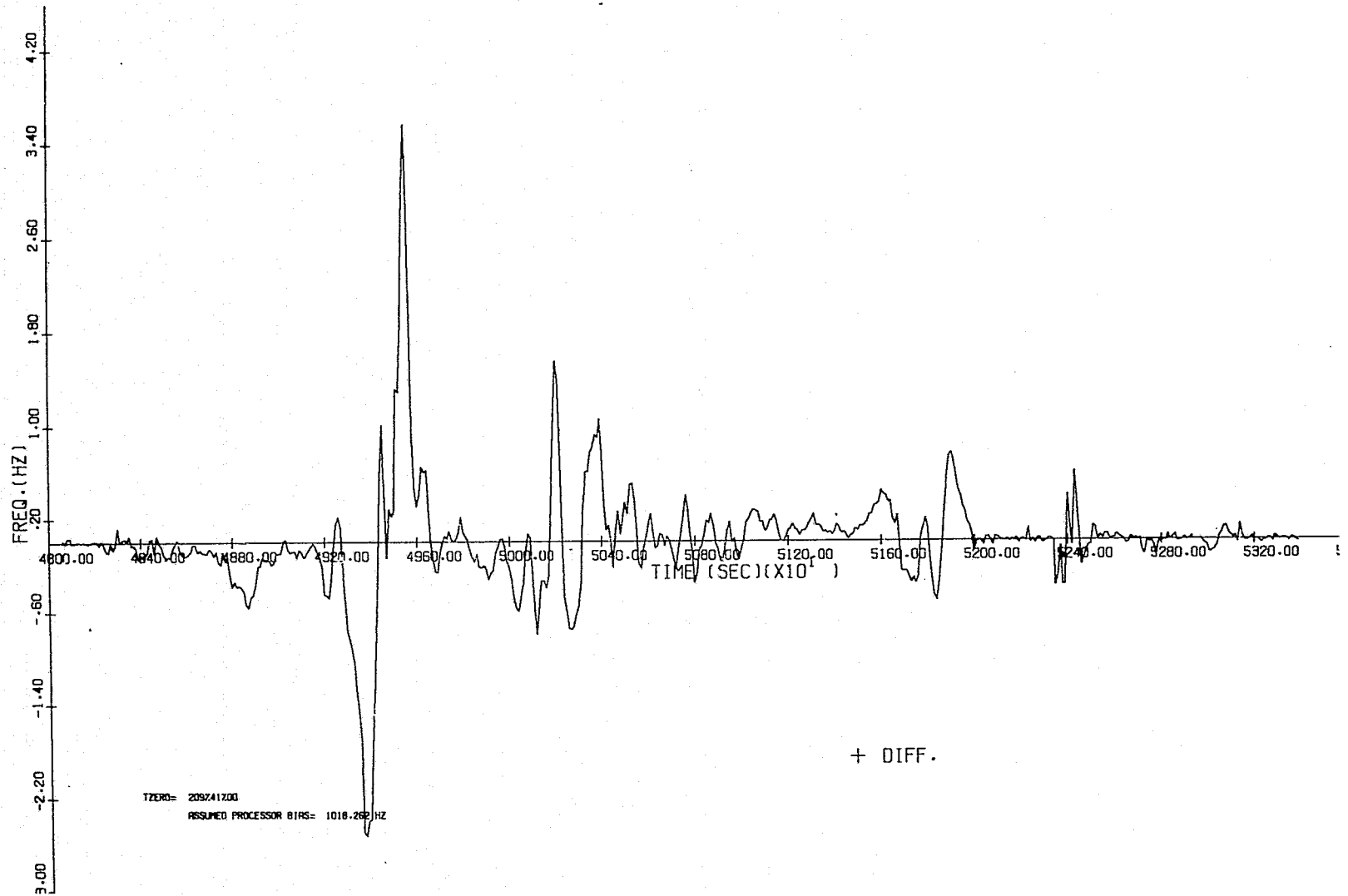
Figure 21. The differential Doppler signal due to the ionosphere.
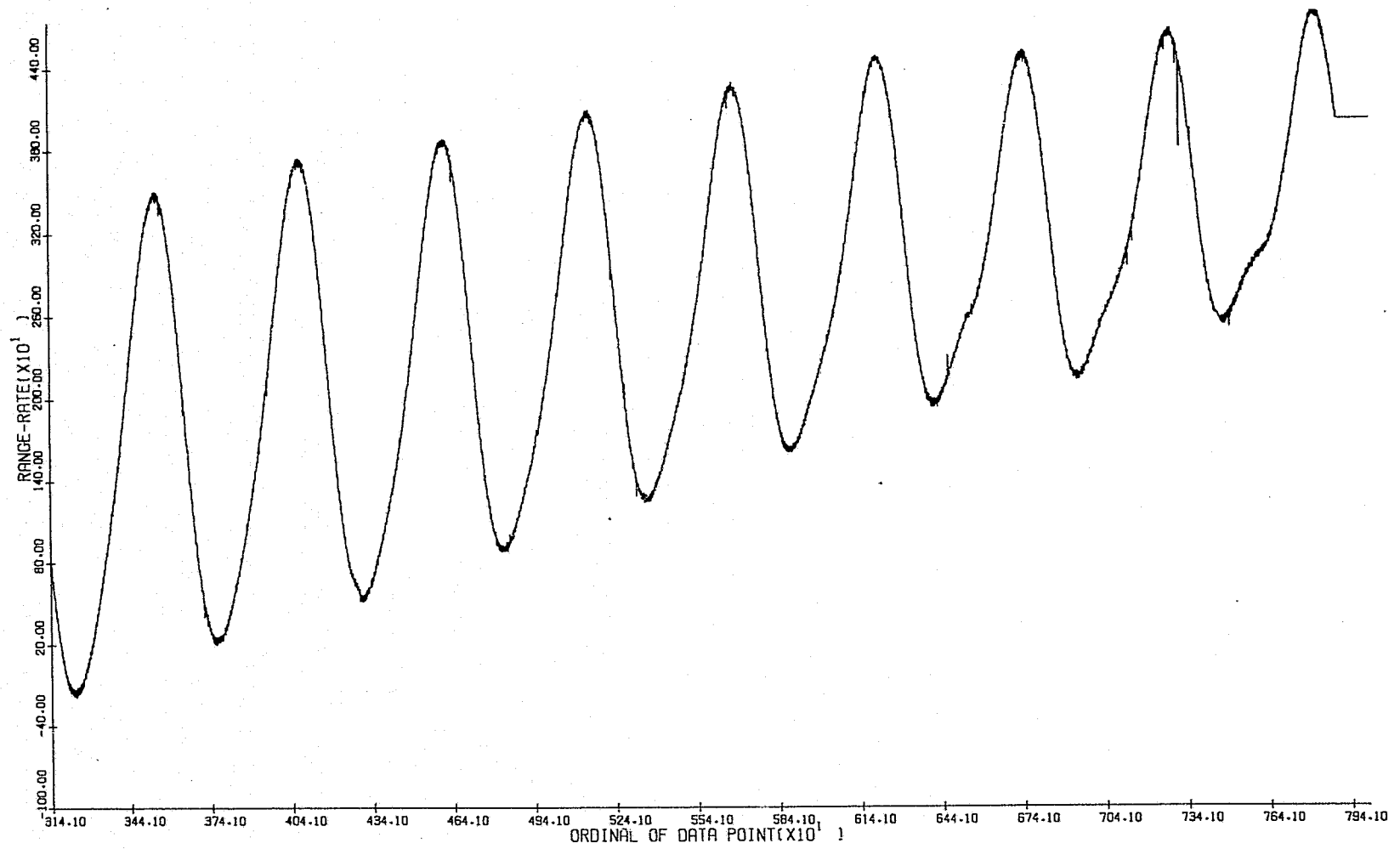
Figure 22. Doppler signal after removal of ionospheric contributions.

5.2 Orbit Determination

To suppress the large-scale variations shown in Figure 22, a range differ-
ence was calculated for each data point from high-precision orbits of the DM
and CSM and subtracted from the observed values. The orbits were determined
independently by directly integrating the equations of motion for each space-
craft and differentially correcting the initial conditions to optimize the fit
to ground-based observations (Tranet Doppler observations of the DM and USB
radar range and range-rate observations on the CSM).

SAO's primary orbit-determination program was used to compute approxi-
mate orbits, which formed the basis for the starting set of initial condi-
tions. To determine an appropriate set of initial conditions, it was first
necessary to eliminate pass-bias errors due to oscillator uncertainties from the
observed Tranet range-difference data. This was accomplished by means of a
series of orbit determinations within consecutive overlapping time intervals of
0.4 day spanning a total period of 2 days from MJD 42616.0 to 42618.2. Table 3
gives the resulting frequency biases recovered from these orbital arcs. A
graphical presentation of these data is given in Figure 23. A regression line
was subsequently fitted to this set of biases in order to calculate the apparent
frequency drift of the oscillator. The slope of the regression line was found
to indicate a frequency drift in 1 day of 0.417 hertz per 300 megahertz, while
the mean offset was found to be 18.4 hertz per 300 megahertz.

After we determined the biases, we corrected each Tranet observation and
employed the resulting set of data as input to the precision orbital integration
package.

Table 3. Frequency biases from Tranet observations.

Pass number	Station number	Epoch of first obs/pass	Pass bias (m/sec)
25	2105	42616.8643	19.711
29	2028	42616.9086	15.898
36	2028	42616.9722	18.412
48	2022	42617.0794	15.775
49	2027	42617.0831	18.419
53	2103	42617.0988	18.280
54	2192	42617.1002	13.968
61	2197	42617.1510	18.175
68	2105	42617.2539	18.032
84	2027	42617.4053	13.754
97	2021	42617.5187	14.290
103	2112	42617.6068	18.020
106	2016	42617.6461	17.681
107	2021	42617.6462	12.571
115	2111	42617.6999	18.770
118	2016	42617.7090	19.025
123	2103	42617.7599	17.920
130	2024	42617.8098	12.243
136	2105	42617.8495	19.139
141	2028	42617.8941	18.572
147	2028	42617.9578	16.411
148	2111	42617.9591	16.190

Table 3. (Cont.)

Pass number	Station number	Epoch of first obs/pass	Pass bias (m/sec)
156	2008	42618.0336	19.976
158	2022	42618.0634	16.659
162	2103	42618.0830	17.312
163	2192	42618.0854	11.836
169	2197	42618.1363	18.119
174	2197	42618.1999	17.277
176	2105	42618.2402	18.415
193	2008	42618.4249	17.911
205	2016	42618.6307	12.233
209	2028	42618.6854	17.596
211	2016	42618.6947	16.952
220	2028	42618.8151	17.063
223	2105	42618.8339	17.508
226	2028	42618.9425	16.171
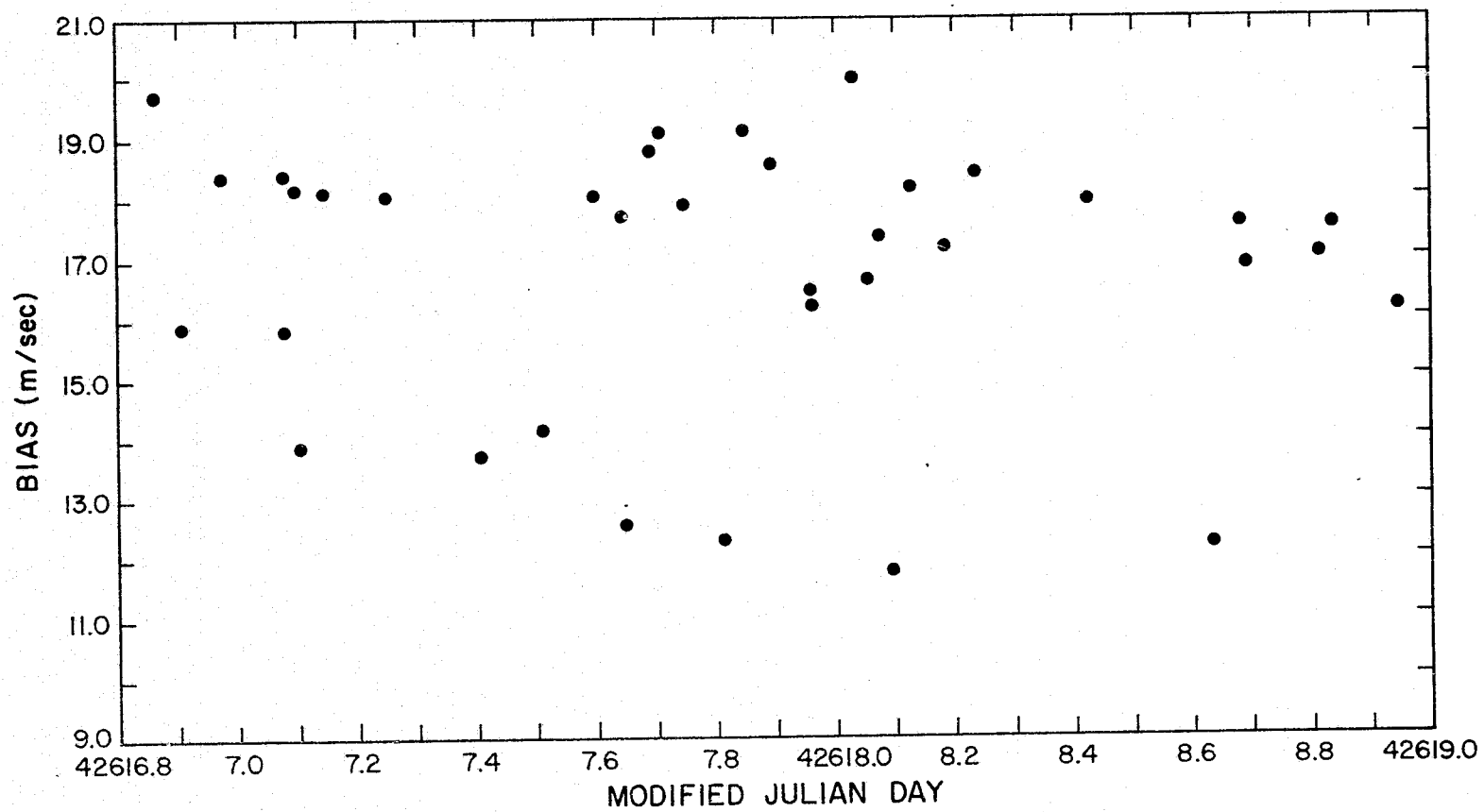
Figure 23.   Frequency biases from 0.4-day orbits (Tranet observations).

An additional parameter estimated from the set of 0.4-day arcs was the DM area-to-mass ratio, A/m. For a circular orbit (ref. 20), A/m is given by

$$\frac{A}{m} = \frac{\dot{P}}{3\pi a d C_D} \quad ,$$

where $\dot{P}$ is the rate of change of the orbital period, a is the semimajor axis, d is the atmospheric density, and C_D is the drag coefficient. Since the program provides the first and second time derivatives of the mean anomaly M, the value of $\dot{P}$ was obtained from

$$\dot{P} = - \frac{\ddot{M}}{2\dot{M}} \quad .$$

Assuming $C_D = 2.0$, $d = 10^{-13}$ g/cm^3, $a = 6.587 \times 10^8$ centimeters, $\dot{M} = 16.237$ rev/day, and $\ddot{M} = 9.932 \times 10^{-3}$ rev/day/day, we derived an area-to-mass ratio for the DM of 0.030 cm^2/g.

Once the pass biases, A/m, and orbital elements had all been estimated from the orbital processor, the final orbit determinations were performed by a precision numerical-integration package. This package consisted of a core integrator of the Adams-Moulton type developed at the Jet Propulsion Laboratory; step size and integration order were automatically chosen according to the desired accuracy. The gravity field came from the 1973 Smithsonian Standard Earth (III) (SE III) (ref. 21) and included spherical-harmonics coefficients through degree and order 12. To compute lunisolar forces, we derived positions of the Sun and Moon from the American Ephemeris and Nautical Almanac.

Atmospheric drag D was given by (ref. 20)

$$D = \frac{dV^2}{2} \frac{A}{m} C_D \quad ,$$

where V is the velocity of the satellite and $C_D = 2$. The atmospheric density variation over the orbit was represented by a polynomial in time fitted with 1% accuracy to 500 points per revolution along the nominal trajectory. The densities of these 500 points were calculated from Jacchia's static-diffusion model 39H.

The following paragraphs outline the principles of how the precision integration package operated in the final orbit determination.

The six initial conditions for each vehicle, X_0, $\dot{X}_0$, Y_0, $\dot{Y}_0$, Z_0, and $\dot{Z}_0$, were refined by a differential-correction and least-squares scheme. The system of equations consisted of the three differential equations of motion for the Cartesian coordinates of each vehicle, plus 18 additional second-order equations relating the partial derivatives of the instantaneous coordinates of the vehicle with respect to the initial coordinates. When these were integrated, we got partial derivatives of X, $\dot{X}$, Y, $\dot{Y}$, Z, and $\dot{Z}$ with respect to the initial conditions X_0, $\dot{X}_0$, Y_0, $\dot{Y}_0$, Z_0, and $\dot{Z}_0$, from which we formed

$$\frac{\partial \rho}{\partial X_0} = \frac{\partial \rho}{\partial X} \frac{\partial X}{\partial X_0} + \frac{\partial \rho}{\partial \dot{X}} \frac{\partial \dot{X}}{\partial X_0} + \ldots + \frac{\partial \rho}{\partial \dot{Z}} \frac{\partial \dot{Z}}{\partial X_0}$$

and, similarly for the remaining partial derivatives,

$$\frac{\partial \rho}{\partial \dot{X}_0} \quad , \quad \frac{\partial \rho}{\partial Y_0} \quad , \quad \frac{\partial \rho}{\partial \dot{Y}_0} \quad , \quad \frac{\partial \rho}{\partial Z_0} \quad , \quad \frac{\partial \rho}{\partial \dot{Z}_0} \quad .$$

To conserve computing time, we integrated this system of equations by evaluating analytically the partial derivatives of the components of the force with respect to those vehicle coordinates that entered the differential-correction process. We used a simplified gravity-field model consisting of the $1/r^2$ term and the J_2 terms of the SE III gravity field. We verified this approximation by using values of the partial derivatives obtained from integrating the system of equations with all the force derivatives evaluated from the full gravity field. The results agreed to within 1 to 2% over a 0.6-day integration period.

Once the partial derivatives of the observed quantities had been determined with respect to the initial conditions, we formed observation equations, such as the following:

$$(\rho_0 - \rho_c)_i = \left(\frac{\partial \rho_c}{\partial X_0}\right)_i \Delta X_0 + \left(\frac{\partial \rho_c}{\partial \dot{X}_0}\right)_i \Delta \dot{X}_0 + \ldots + \left(\frac{\partial \rho_c}{\partial \dot{Z}_0}\right)_i \Delta \dot{Z}_0 \quad ,$$

where ρ_0 is the observed value of the range or the range difference and ρ_c is the integrated (computed) value of the observation, both at time t_i. These equations are as numerous as the number of observations of the vehicle. The integrator proceeded through the specified time period, setting up an observation equation each time an observation was reached. When the final observation had been reached, the equations were solved in a least-squares sense for the small corrections to the initial conditions: ΔX_0, $\Delta \dot{X}_0$, ΔY_0, $\Delta \dot{Y}_0$, ΔZ_0, and $\Delta \dot{Z}_0$. These corrections were applied to the previous estimate of X_0, $\dot{X}_0$, Y_0, $\dot{Y}_0$, Z_0, and $\dot{Z}_0$, and the process was repeated until the standard error of the solution decreased by less than 1% from its previous value.

Because an accurate area-to-mass ratio was not known for either satellite, we selected the value of A/m that minimized the standard error of the calculated orbit. Starting with the estimate of 0.030, we varied A/m for the DM from 0.01 to 0.06. The standard error of the DM orbit exhibited a minimum of about 10 meters for A/m = 0.035 cm^2/g. The CSM area-to-mass ratio was taken as 0.002 cm^2/g, and varying it had little effect. The mean elements for the DM and the CSM are given in Table 4. Orbits for the DM were calculated every 0.2 day, and the orbital elements are plotted in Figure 24. Table 5 lists the initial condition used in the numerical-integration program.

5.3 Comparison of Calculated and Observed Range Differences

Once the initial conditions were established, an ephemeris for each spacecraft was calculated. This was the basis from which a predicted DM/CSM "Doppler signal" was computed for every 10-second interval throughout the lifetime of the experiment. When these calculated range differences were subtracted from the observations (which had been corrected for ionospheric effects), the residuals varied over a range of several hundred millimeters per second.

The residual scatter was further reduced by fitting the calculated values of $\dot{\rho}_c$ to the observed values of $\dot{\rho}_o$. Using the polynomial

$$\tilde{\rho} = \sum_{i=1}^{15} A_i t^{\ell_i} \dot{\rho}_c^{m_i} + B \cos \frac{2\pi t}{5000} + C \cos \frac{2\pi t}{2500} \quad ,$$

where $2\pi t$ is the orbital period and ℓ_i and m_i ranged from 1 to 4, A_i, B, and C were determined in an iterative manner by means of a least-squares estimator. This process was repeated eight times, using $\tilde{\rho}_c$ as a new value for $\dot{\rho}_c$ each time, reducing the scatter in the observed-minus-computed residuals to 20 mm/sec.

Table 4. Instantaneous elements for the DM and CSM
(epoch = 42617.008305567).

	DM	CSM
X (cm)	3.369937×10^8	3.478627×10^8
Y (cm)	4.567079×10^8	4.345419×10^8
Z (cm)	-3.352690×10^8	-3.531287×10^8
$\dot{X}$ (cm/sec)	-2.859357×10^5	-2.672850×10^5
$\dot{Y}$ (cm/sec)	5.536761×10^5	5.779922×10^5
$\dot{X}$ (cm/sec)	4.650151×10^5	4.461675×10^5
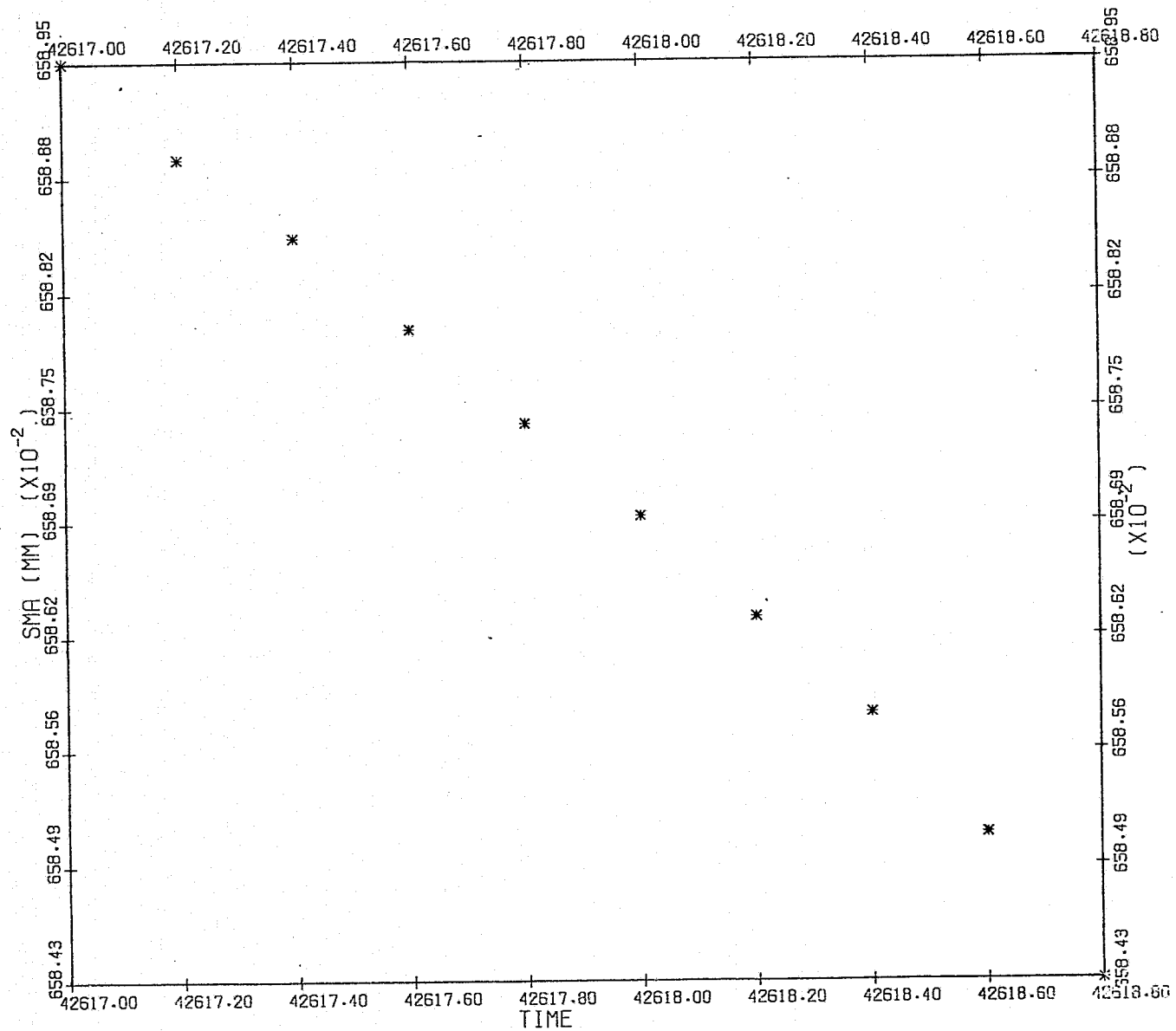
Figure 24. Orbital elements for the DM every 0.2 day.

102

Figure 24. (Cont.)

103

Figure 24. (Cont.)

104

Figure 24.   (Cont.)

105
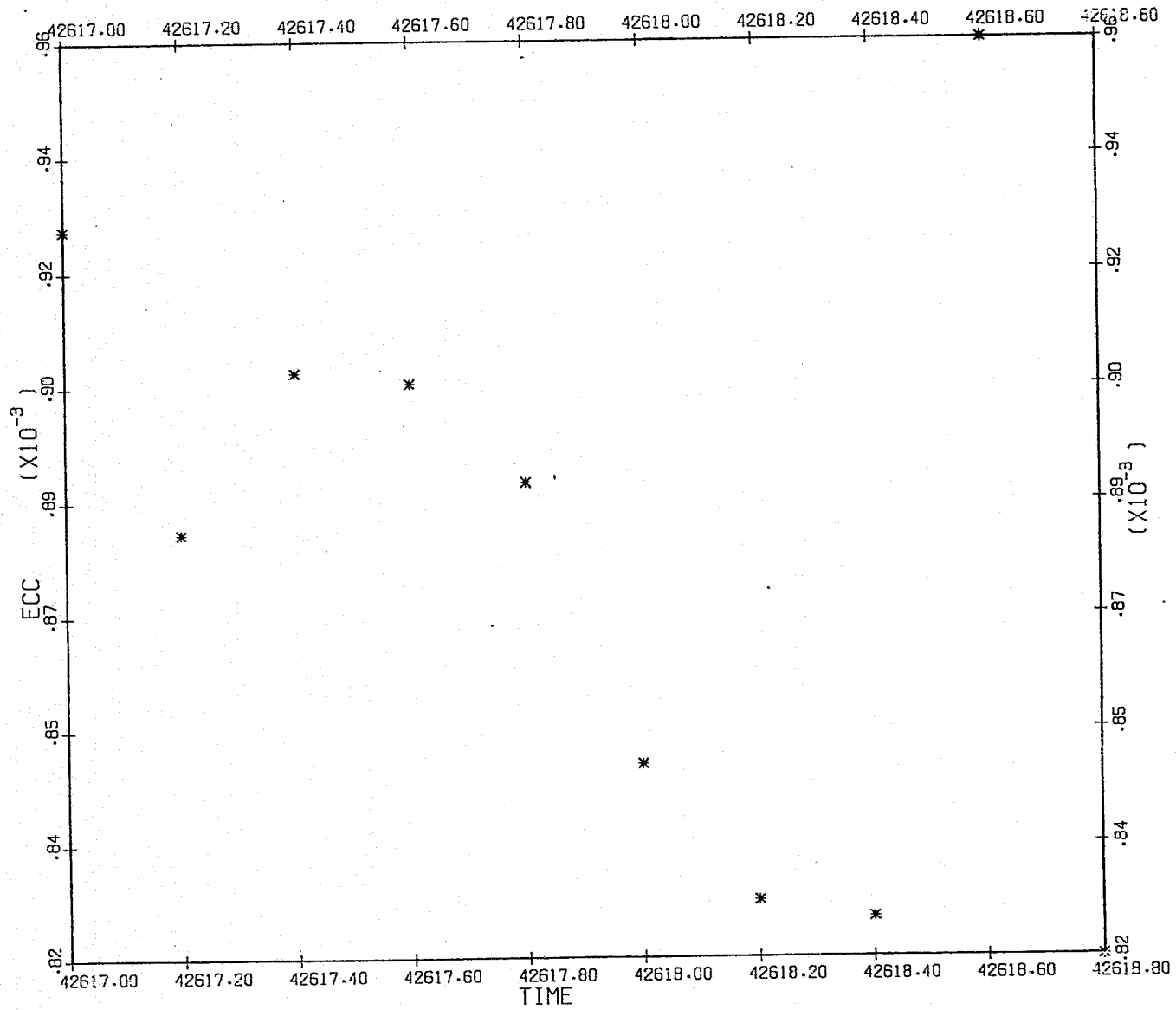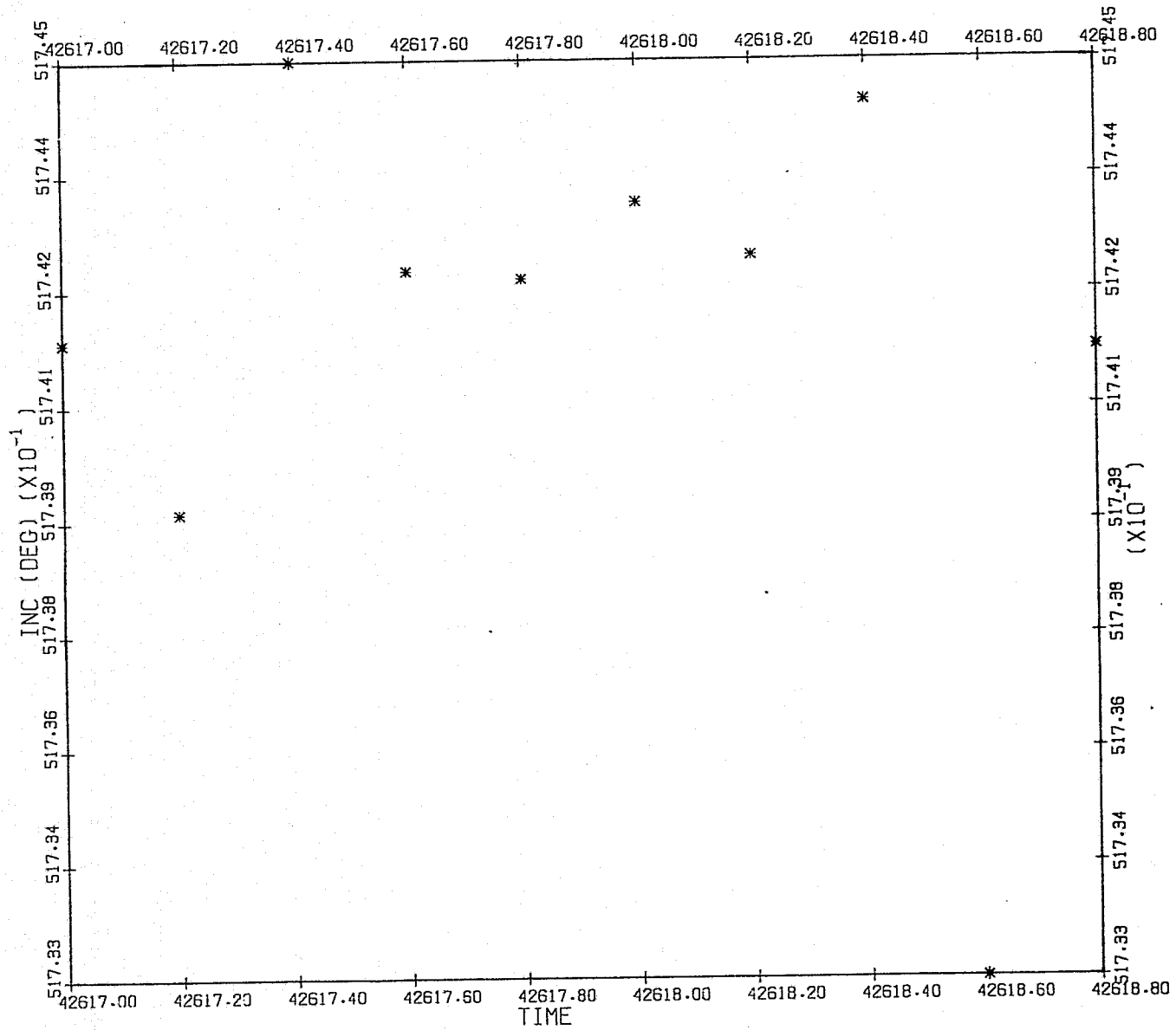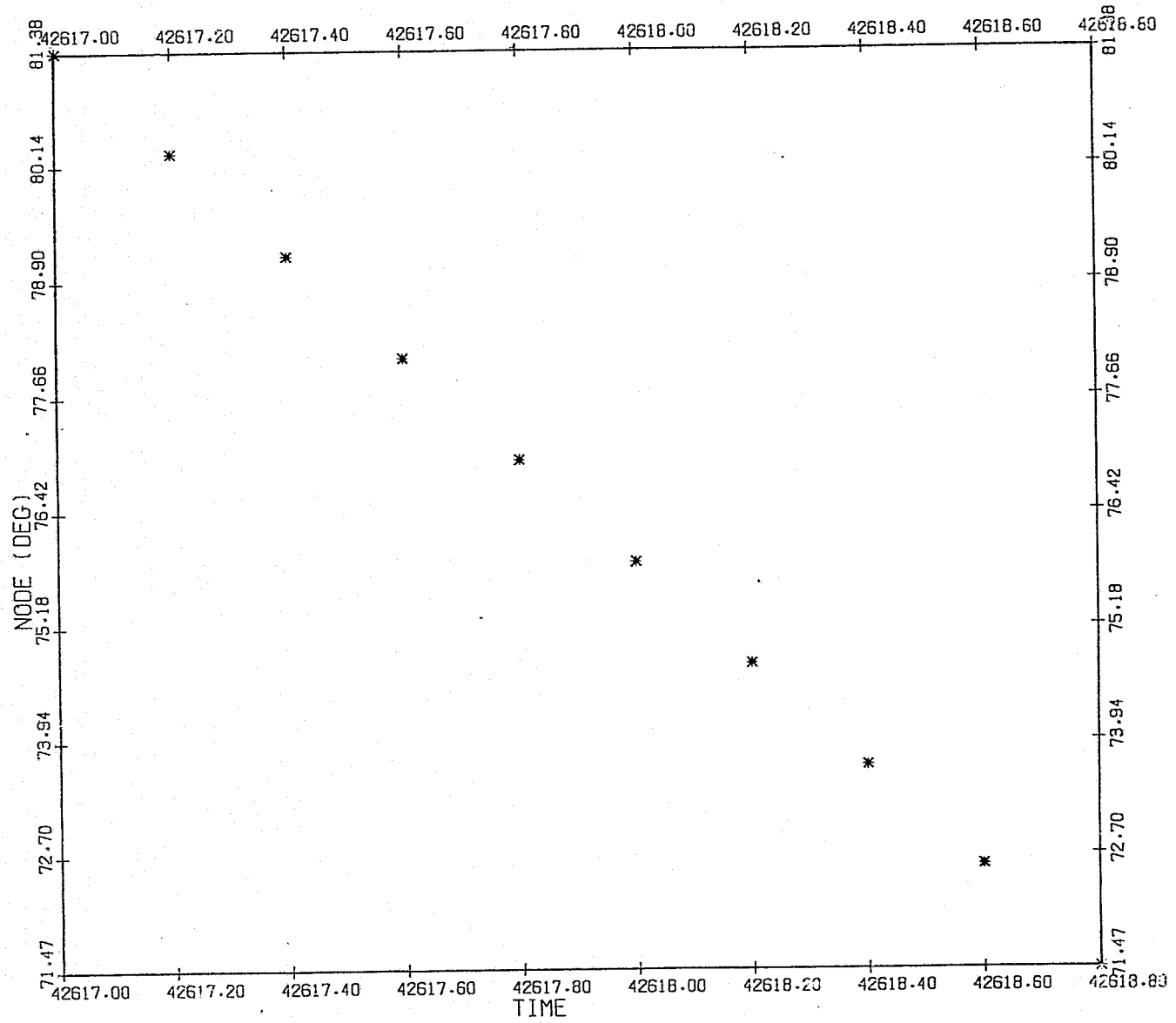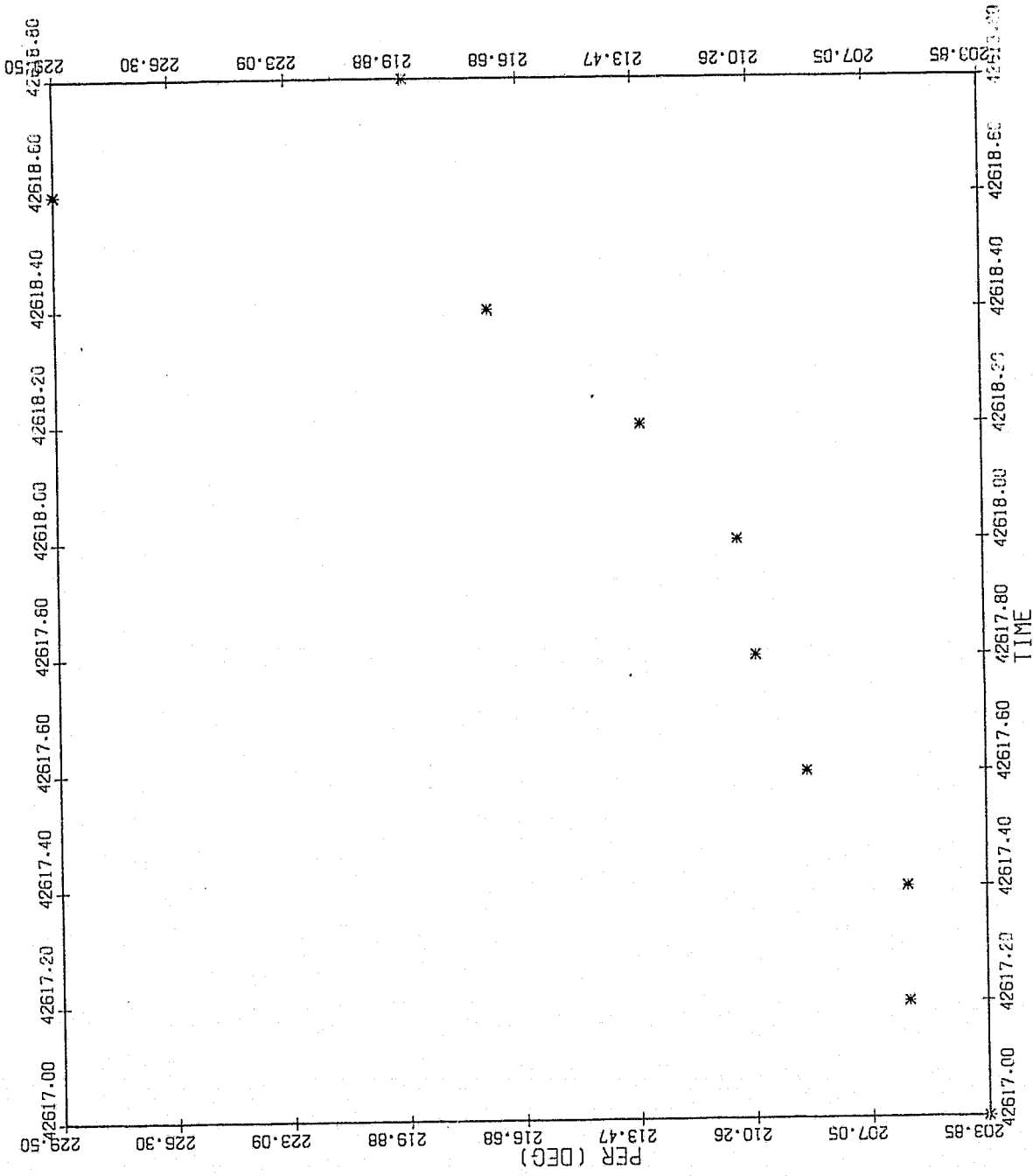
Figure 24. (Cont.)

Table 5. Orbital data for the DM and the CSM (epoch 42617.008305567 MJD).

Orbital element	DM	CSM
Semimajor axis	6590.818 km	6590.843 km
Eccentricity	0.001194	0.001237
Inclination	51°7704	51°7657
True anomaly	98°984865652	97°558757298
Longitude of the ascending node	81°3086	81°3114
Argument of perigee	220°5304	219°3008

The "corrections" Δv added to the range rate $\dot\rho_c$ calculated from the two orbits were then subjected to a Fourier analysis to ensure that the estimator had suppressed only the orbital component of the intervehicular range rate and had not introduced any "high-frequency" components (wavelengths shorter than about 1000 seconds) that might be mistaken for gravity anomalies.

5.4 CSM and DM Rotation

A significant contribution to the residual scatter arises from the fact that the observed range differences were from antenna to antenna, whereas the calculated differences were between the centers of mass of the CSM and the DM. Therefore, the next step was to model the motions of the antennas relative to the centers of mass so that their effects could be removed from the residuals.

Because the receiving antenna was so nearly on the line between the centers of mass of the two spacecraft, CSM rotational motions greater than $0°1/$ sec over 10-second intervals would be required to generate Doppler signals of 1 mm/sec. Fourier spectra of the rate gyro data were examined, along with the data themselves. Since no evidence of motions approaching $0°1/sec$ was found (except when the CSM was maneuvered to reacquire ATS-6 after the astronauts' sleep period), no further effort was devoted to modeling CSM motions.

The DM signature was determined by finding the periods of the dynamical motion for individual segments of the data-take interval. Segmentation boundaries were closed on the times of entry into and exit from the Sun-Earth

shadow (see Section 2.4.7). A nonlinear least-squares polynomial processor was developed and employed to determine the amplitudes, periods, and phases of the rotational range-rate components. The form of the polynomial was

$$\dot{\rho} = A_1 \cos \frac{2\pi t}{P + p} + A_2 \cos \frac{2\pi t}{P - p} + A_3 \cos \frac{2\pi t}{P} + A_4 \cos \frac{2\pi t}{P/2}$$

$$+ A_5 \cos \frac{2\pi t}{P/3} + A_1 \sin \frac{2\pi t}{P + p} + A_2 \sin \frac{2\pi t}{P - p} + A_3 \sin \frac{2\pi t}{P}$$

$$+ A_4 \sin \frac{2\pi t}{P/2} + A_5 \sin \frac{2\pi t}{P/3} \quad ,$$

where P is the period of rotation and p is the period of nutation, or coning. The DM rotational period was close to 72 seconds, but both periods increased with time. We assumed a linear increase, calculated $\dot{\rho}_{DM}$ for each data point, and removed it from the residuals. These steps reduced the scatter by a factor of 2.

5.5 Conclusions

Finally, the baseline was flattened by a 40-point averaging technique, and a filter to remove periods shorter than 50 seconds was applied. This left the residuals with an rms amplitude of 6.5 mm/sec.

A sample of the reduced data is shown in Figure 25. A Fourier spectrum of the entire data run is shown in Figure 26.
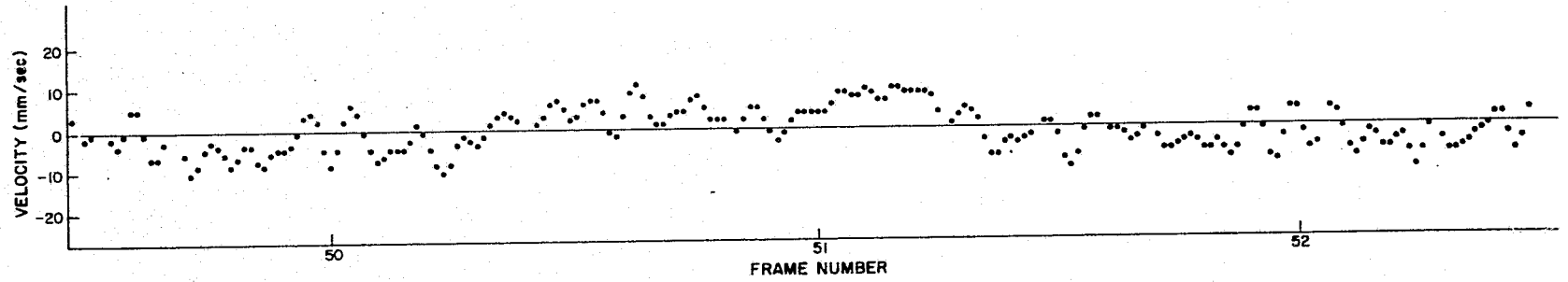
Figure 25. Sample of reduced Doppler data.
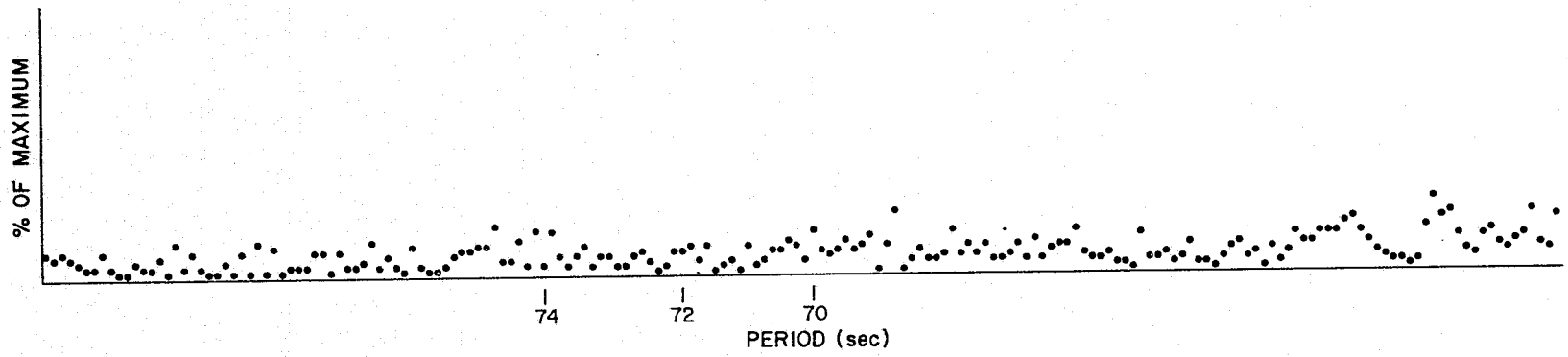
Figure 25. Fourier spectrum of reduced Doppler data.

6. RESULTS

6.1 Introduction

The results of this rather involved analysis are discussed in two main parts. The first refers to the ionospheric observations, highly successful though not completely analyzed. The second part describes the inconclusive search for gravity signatures in the satellite-to-satellite velocity data.

The experiment design anticipated a signal-to-noise ratio near 1. With data from other sources — the Goddard geodynamics experiment (MA-128), surface-gravity measurements, or Geos-3 altimetry, for example — or with a longer data take, unambiguous identification of gravitationally induced velocity variations would be possible, thereby demonstrating the feasibility of this technique. Unfortunately, noise levels more than twice that expected precluded such positive identifications.

6.2 Early Results from the Ionospheric Experiment

Differential Doppler data were collected in both DM-to-CSM and DM-to-Earth paths by using the links shown schematically in Figure 27. The goals of the ionospheric experiment were as follows (refs. 18, 19, 22, and 23):
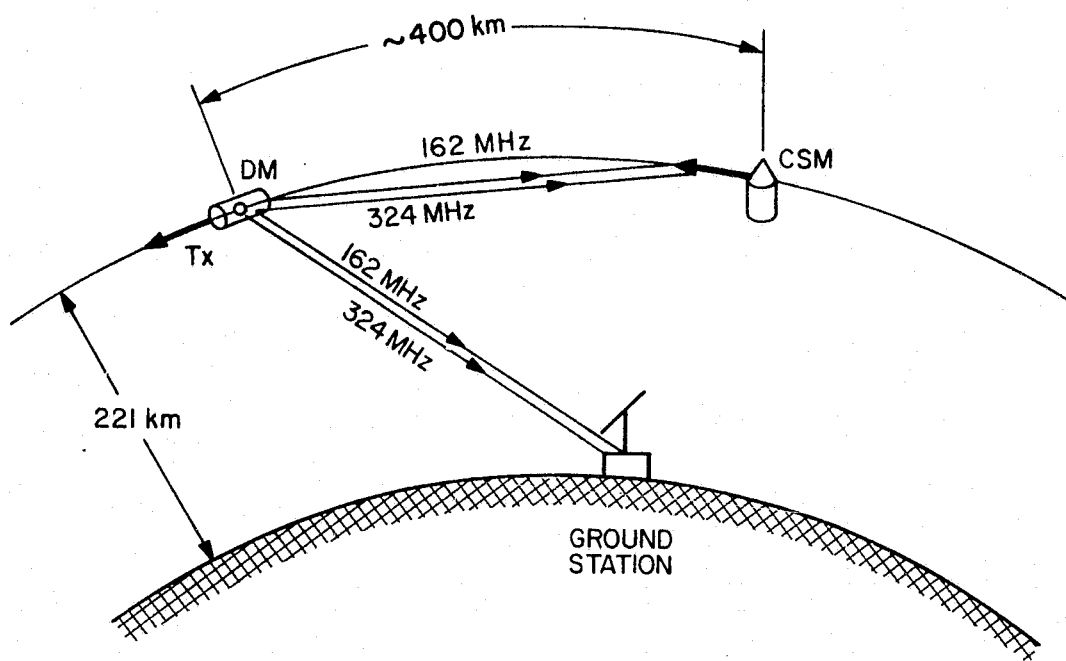
Figure 27.   Schematic diagram of Doppler links.

113

1. To measure the time changes of the columnar electron content between the two spacecraft, from which horizontal gradients of electron density at the height of 220 kilometers (along the orbital path of the DM/CSM pair) could be derived.

2. To measure the time changes of the spacecraft-to-ground columnar electron content, from which an averaged columnar content and the electron density at the DM could be derived under some simplifying assumptions. Because horizontal gradients at orbital heights were measured simultaneously, a secondary goal was to investigate the increase in accuracy obtained by performing these inversions.

3. To observe traveling ionospheric disturbances with both the DM-to-CSM and the DM-to-Earth links.

4. To detect boundaries of turbulent regions of the ionosphere, such as the aurora oval and the equatorial region.

The data-collection phase of the experiment was highly successful. The DM-to-CSM link collected samples of differential Doppler data over a period of nearly 14 hours from nine orbital revolutions on July 24. Through the courtesy of the Defense Mapping Agency, DM dual-frequency emissions were recorded on Earth by eight Tranet and Geoceiver tracking stations on 235 passes. Table 5 provides orbital data for both the DM and the CSM.

The resolution in the Doppler measurements was $1\sigma \approx 3$ millihertz in 10-second integration time, consistent with preflight expectations. The oscillators of the Doppler links performed as specified, with a stability of a few parts in 10^{12} over a 10- to 100-second integration interval.

Block diagrams of the instrumentation can be found in ref. 22. Figures 28 and 29 provide a schematic representation of the raw data utilized by the experiment and of the data-reduction and processing flow adopted.

Let us define $\delta\dot\phi = \dot\phi_1 - (f_1/f_2)\dot\phi_2$, where $\dot\phi_1$ and $\dot\phi_2$ are the Doppler shifts at the higher (f_1) and lower (f_2) frequencies of the link. In our case, $f_1 = 324$ megahertz and $f_2 = 162$ megahertz; therefore,

$$\delta\dot\phi = \dot\phi_1 - 2\dot\phi_2 \quad .$$

In the path from the DM to the CSM, the following relationship applies:

$$\delta\dot\phi = (40.3/2\lambda_1) \, [(1/f_2^2) - (1/f_1^2)] \; d/dt \int_{DM}^{CSM} N \; ds \quad ,$$

where $\lambda_1 = c/f_1$, c being the velocity of light in free space.

Under the assumptions that the two terminals of the link were in nearly coincident circular orbits and that the temporal variations of the ionosphere could be disregarded while the Doppler samples were being taken, the differential Doppler shift $\delta\dot\phi$ is a measure of the electron-density gradients at the ASTP orbital altitude averaged over the DM-to-CSM separation Δx:

$$\overline{\frac{\partial N}{\partial x}} = \frac{\lambda_1 f_1^2 f_2^2}{40.3(f_2^2 - f_1^2)} \; \frac{\delta\dot\phi}{v_0 \, \Delta x} \quad , \tag{96}$$

where v_0 is the common orbital velocity of the two terminals.

```
┌──────────────┐      ┌──────────────────┐                                              ┌──────────────┐
│ CSM/DM       │      │ DATA RECORDED    │                                              │ DATA RECORDED│
│ PREFLIGHT    │      │ ON BOARD CSM     │                                              │ ON THE GROUND│
│ DATA         │      │ DURING ASTP FLIGHT│                                             └──────────────┘
└──────────────┘      └──────────────────┘
```

┌──────────────────┐
│ MASS GEOMETRY   │
├──────────────────┤
│ INERTIA TERM   │
└──────────────────┘

┌──────────────────┐
│ OUTER SHAPE   │
│ AND OPTICAL   │
│ PROPERTIES   │
└──────────────────┘

┌──────────────────┐
│ MAGNETIC   │
│ DATA   │
└──────────────────┘

┌──────────────────┐
│ ANTENNA DATA   │
├──────────────────┤
│ POSITION OF CENTER│
│ OF PHASE AND   │
│ RADIATION PATTERN│
│ DATA   │
└──────────────────┘

┌──────────────────────┐
│ DATA ON   │
│ VARIABLE MASSES   │
│ (FUEL CONSUMPTION,   │
│ LEAKAGES, MOTION   │
│ OF ASTRONAUTS, ETC.) │
└──────────────────────┘

┌──────────────────────┐
│ PHOTOGRAPHIC DATA   │
│ ON DM MOTION   │
│ AFTER SEPARATION   │
│ FROM CSM   │
└──────────────────────┘

┌──────────────────┐
│ CSM RATE   │
│ GYRO DATA   │
└──────────────────┘

┌──────────────────┐
│ ROTATIONAL   │
│ MOTION OF   │
│ CSM   │
└──────────────────┘

┌──────────────────┐
│ DM-TO-CSM   │
│ DOPPLER DATA   │
└──────────────────┘

┌──────────────────┐
│ DIFFERENTIAL   │
│ VELOCITY FOR   │
│ IONOSPHERIC   │
│ CORRECTION   │
└──────────────────┘

┌──────────────────────┐
│ RELATIVE VELOCITY   │
│ DM ANTENNA CENTER   │
│ TO CSM ANTENNA   │
│ CENTER (UNCORRECTED │
│ FROM IONO. ERRORS)   │
└──────────────────────┘

┌──────────────────┐
│ DM-TO-CSM   │
│ SIGNAL AMPLITUDE │
│ DATA   │
└──────────────────┘

┌──────────────────┐
│ NASA STADAN   │
│ NETWORK   │
│ (FOR CSM)   │
└──────────────────┘

┌──────────────────┐
│ CSM TELEMETRY   │
└──────────────────┘

┌──────────────────┐
│ ATTITUDE DATA   │
│ (CSM GIMBAL   │
│ DATA)   │
└──────────────────┘

┌──────────────────┐
│ CSM RATE GYRO   │
│ DATA WITH BETTER │
│ ACCURACY   │
└──────────────────┘

┌──────────────────┐
│ ROTATIONAL   │
│ MOTION OF CSM   │
└──────────────────┘

┌──────────────────┐
│ CSM UNIFIED   │
│ S-BAND TRACKING │
└──────────────────┘

┌──────────────────┐
│ ORBITAL MOTION   │
│ OF CSM CENTER   │
│ S-BAND ANTENNA   │
└──────────────────┘

┌──────────────────────┐
│ ORBITAL MOTION   │
│ OF CSM CENTER   │
│ OF MASS   │
│ (POSITION ERROR   │
│ (σ = 200m)   │
└──────────────────────┘

┌──────────────────┐
│ TRANET   │
│ NETWORK   │
│ (FOR DM)   │
└──────────────────┘

┌──────────────────┐
│ DOPPLER TRACKING │
│ OF DM   │
└──────────────────┘

┌──────────────────────┐
│ MOTION OF   │
│ DM ANTENNA   │
│ CENTER RELATIVE   │
│ TO GROUND   │
│ STATION   │
└──────────────────────┘

┌──────────────────┐
│ SIGNAL   │
│ AMPLITUDE   │
└──────────────────┘

┌──────────────────┐
│ DM ATTITUDE   │
│ FROM NON-   │
│ ISOTROPIC   │
│ RADIATION   │
│ PATTERN OF   │
│ DM ANTENNA   │
└──────────────────┘

┌──────────────────────┐
│ OPTICAL TRACKING   │
│ (SAO - BAKER NUNN   │
│ NETWORK)   │
│ (FOR DM)   │
└──────────────────────┘

┌──────────────────┐
│ ORBITAL   │
│ MOTION OF   │
│ DM'S   │
│ CENTRAL   │
│ MASS   │
└──────────────────┘

┌──────────────────┐
│ INFORMATION   │
│ ON DM   │
│ ATTITUDE   │
└──────────────────┘

┌──────────────────┐
│ AUXILIARY   │
│ GEOPHYSICAL   │
│ DATA   │
└──────────────────┘

┌──────────────────┐
│ SOLAR   │
│ RADIATION   │
│ DATA   │
└──────────────────┘

┌──────────────────┐
│ ATMOSPHERIC   │
│ DENSITY   │
│ DATA   │
│ (ATMO. DRAG)   │
└──────────────────┘

┌──────────────────┐
│ IONOSPHERIC   │
│ SOUNDING   │
│ DATA   │
└──────────────────┘

┌──────────────────┐
│ GRAVITY FIELD   │
│ DATA FROM   │
│ GROUND SURVEY   │
│ AND SATELLITE   │
│ TRACKING   │
└──────────────────┘

┌──────────────────┐
│ ACCURATE   │
│ TIME   │
└──────────────────┘

Figure 28.   Block diagram of the raw data.

117

```
                              ┌─────────────────┐
                              │ PRELIMINARY ORBIT│
                              └─────────────────┘

┌──────────────────────┐                    ┌──────────────┐   ┌──────────────────┐
│ DATA FROM TRANET,    │                    │ ANTENNA      │   │ CSM ACCELEROMETER│
│ USB, BAKER-NUNN,     │                    │ RADIATION    │   │ DATA             │
│ DM-TO-CSM DOPPLER    │                    │ PATTERNS     │   └──────────────────┘
│ TRACKING             │                    │ (AMPLITUDE AND│
└──────────────────────┘                    │  PHASE)      │   ┌──────────────────┐
                                            └──────────────┘   │ PHOTOGRAPHS      │
┌──────────────────────┐                                       │ OF DM/CSM        │
│ GRAVITY-FIELD DATA   │                                       │ SEPARATION       │
│ COORDINATES OF TRACKING STATIONS │                           └──────────────────┘
│ DETAILED MAPS OF ANOMALIES │
│ 10.7-CM FLUX         │                                       ┌──────────────────┐
│ GEOMAGNETIC INDEX    │                                       │ PREFLIGHT DATA   │
│ ORIENTATION OF BOTH DM AND CSM │                             └──────────────────┘
│ SHAPE                │
└──────────────────────┘                                       ┌──────────────────┐
                                                               │ CSM RATE GYRO    │
┌──────────────────────┐          ┌──────────────────┐         │ AND GIMBAL       │
│ TEMPERATURE          │          │ PROGRAM FOR      │         │ INFORMATION      │
│ PRESSURE             │          │ REFRACTION CORRECTION │     └──────────────────┘
│ RELATIVE HUMIDITY    │          │ AND TIME-SYSTEM  │
└──────────────────────┘          │ CORRECTIONS      │         ┌──────────────────┐
                                  └──────────────────┘         │ CONSTRUCT ROTATIONAL │
┌──────────────────────┐          ┌──────────────────┐         │ MOTION OF DM AND CSM │
│ TIME CORRECTIONS     │          │ PRECISION ORBIT  │         └──────────────────┘
└──────────────────────┘          │ COMPUTATION USING│
                                  │ REDUCED DATA FROM│
┌──────────────────────┐          │ TRANET, USB, AND DM-TO- │
│ NOAA GROUND-         │          │ CSM DOPPLER TRACKING │
│ BASED NETWORK        │          └──────────────────┘
└──────────────────────┘                                       ┌──────────────────┐
                                  ┌──────────────────┐         │ COMPUTE CORRECTIONS │
┌──────────────────────┐          │ ACCELERATION     │         │ DM-TO-CSM DOPPLER ERRORS │
│ IONOSPHERIC          │          │ OF CSM CENTER    │         │ DUE TO ROTATIONS OF CSM │
│ SOUNDINGS            │          │ OF MASS DUE TO   │         │ AND DM           │
└──────────────────────┘          │ ASTRONAUT MOTION,│         └──────────────────┘
                                  │ GAS JET FIRINGS, │
┌──────────────────────┐          │ OUTGASSING, ETC. │
│ PROGRAM TO           │          └──────────────────┘
│ OBTAIN               │
│ IONOSPHERIC          │          ┌──────────────────┐
│ PROFILES             │          │ ORBITS OF DM AND CSM │
└──────────────────────┘          └──────────────────┘

┌──────────────────────┐   ┌──────────────────┐
│ DIFFERENTIAL DOPPLER │   │ PROFILE INVERSION│
└──────────────────────┘   │ OF DM-TO-CSM     │
                           │ REFRACTIVITY DATA│
                           └──────────────────┘

                           ┌──────────────────┐   ┌──────────────────────────┐
                           │ IONOSPHERIC      │   │ ANOMALOUS ACCELERATIONS  │
                           │ PROFILE FROM     │   │ AS A FUNCTION OF POSITION │
                           │ DM-TO-CSM        │   └──────────────────────────┘
                           │ DOPPLER TRACKING │
                           └──────────────────┘
```
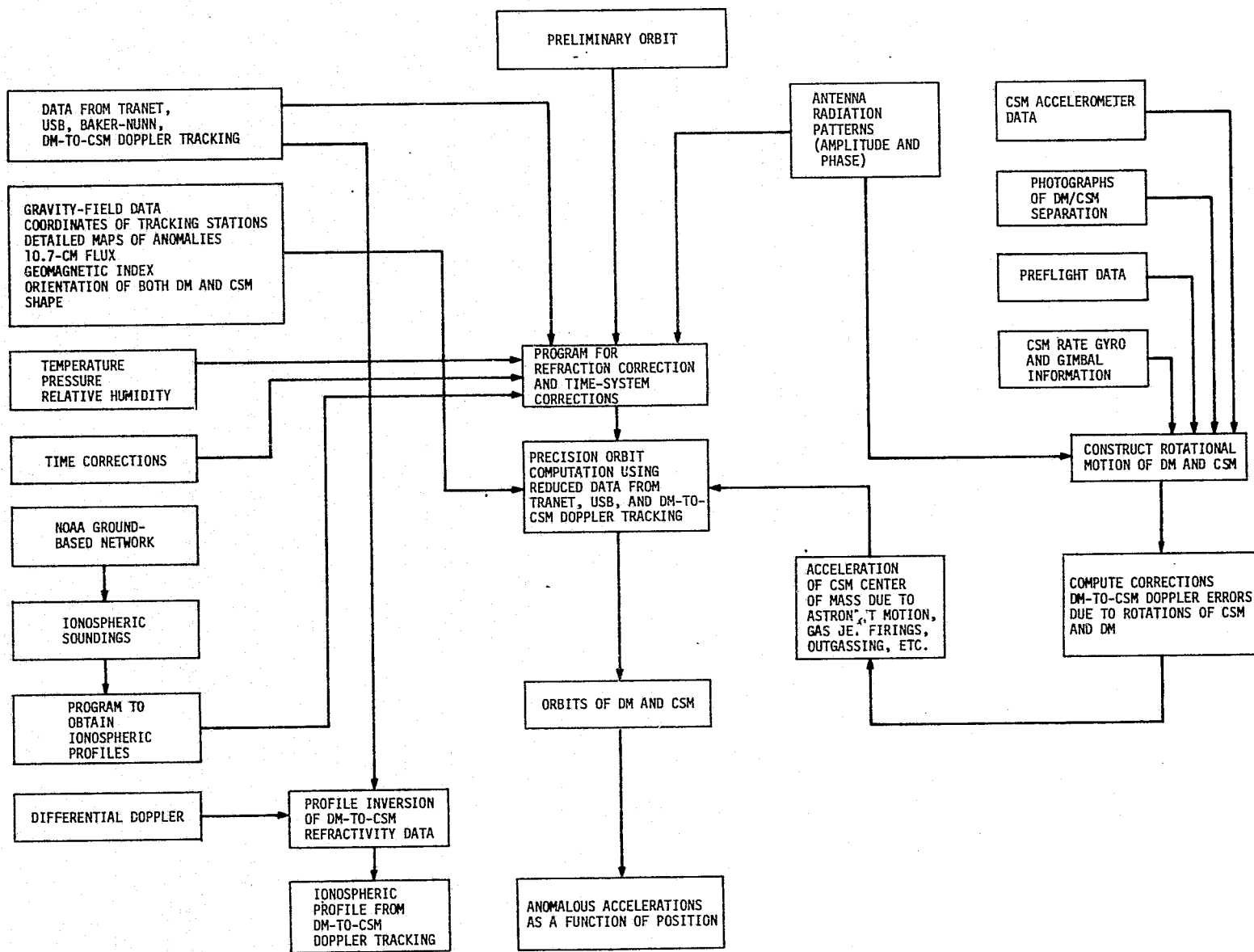
Figure 29. Simplified scheme of data reduction and processing.

In DM-to-Earth paths, equation (9) applies (see Figure 2 and ref. 24) if horizontal gradients are neglected. When horizontal gradients are taken into account, equation (15) is used instead (ref. 24).

Figures 30 and 31 reproduce the DM-to-CSM differential Doppler records obtained from revolutions 127 and 131. Table 6 gives the starting time of each orbit and the serial number of the frame-word recorded when the DM crossed the meridian containing the subsolar point (SSP). Each frame has 73 words, each 10 seconds long, so that, for example, the start of revolution 126 corresponds to (47 × 73 + 31) × 10 = 34,620 seconds from reference time zero, which was set at the beginning of the link operation.

It can be seen that sharp horizontal gradients of electron density have been detected. From equation (96), we have $\overline{\partial N/\partial x} = 2.62 \times 10^5 \times \dot{\delta\phi}$ (el/m^3/m). The figures show that gradients up to $\sim 10^6$ el/m^3/m are not uncommon for a day such as July 24, which was magnetically quiet and was characterized by an electron density at 220-kilometer height that varied from $\sim 3 \times 10^9$ el/m^3 (night side) to $\sim 5 \times 10^{11}$ el/m^3 (day side). Most of the gradients are encountered at the equatorial crossings and are most likely related to the equatorial F-layer irregularities.

The nine-cycle waveform shown in Figure 30 is suggestive of a day-side traveling ionospheric disturbance characterized by the following parameters (preliminary model):
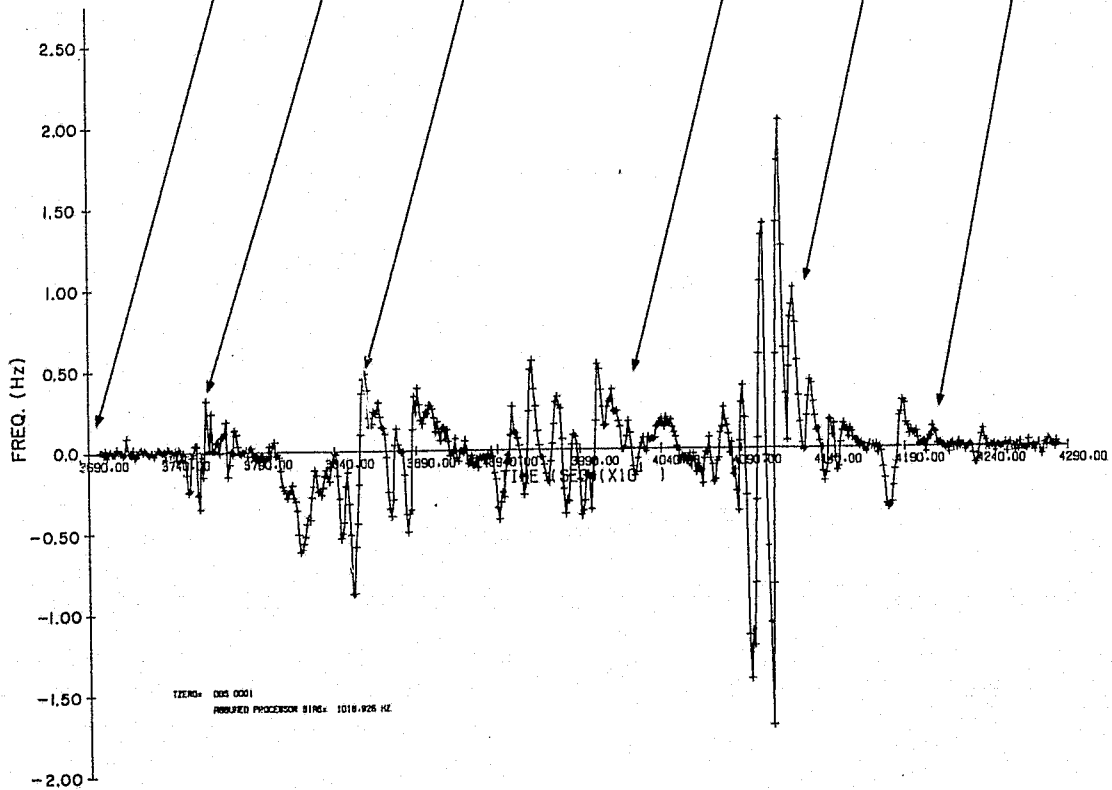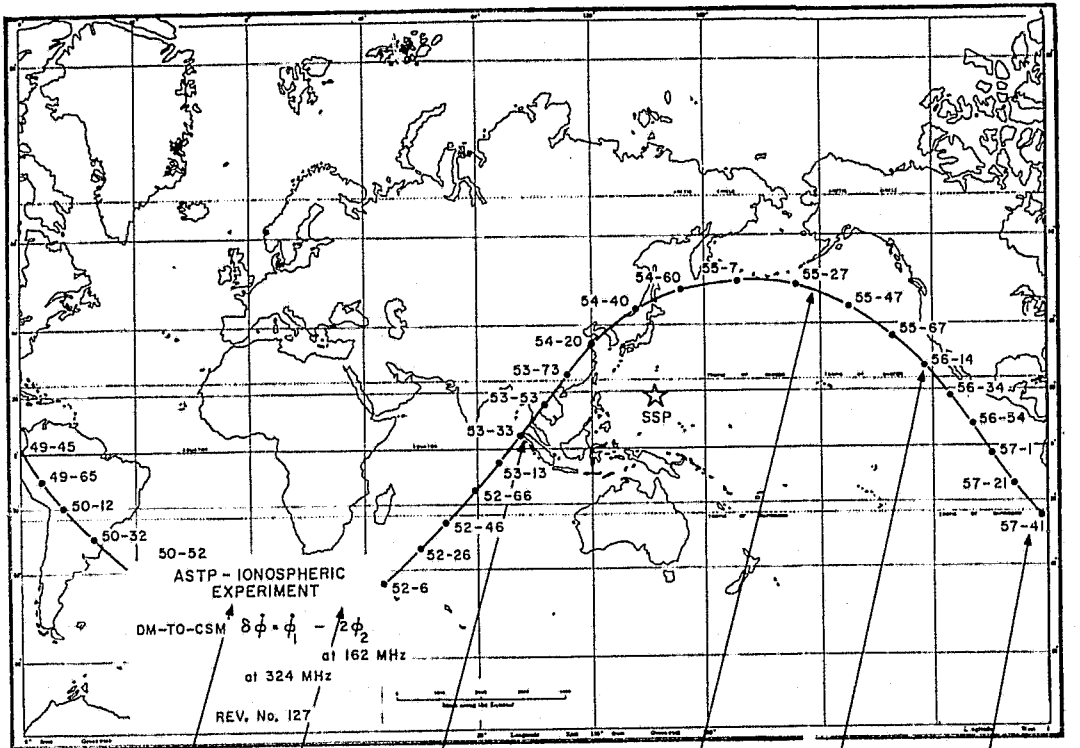
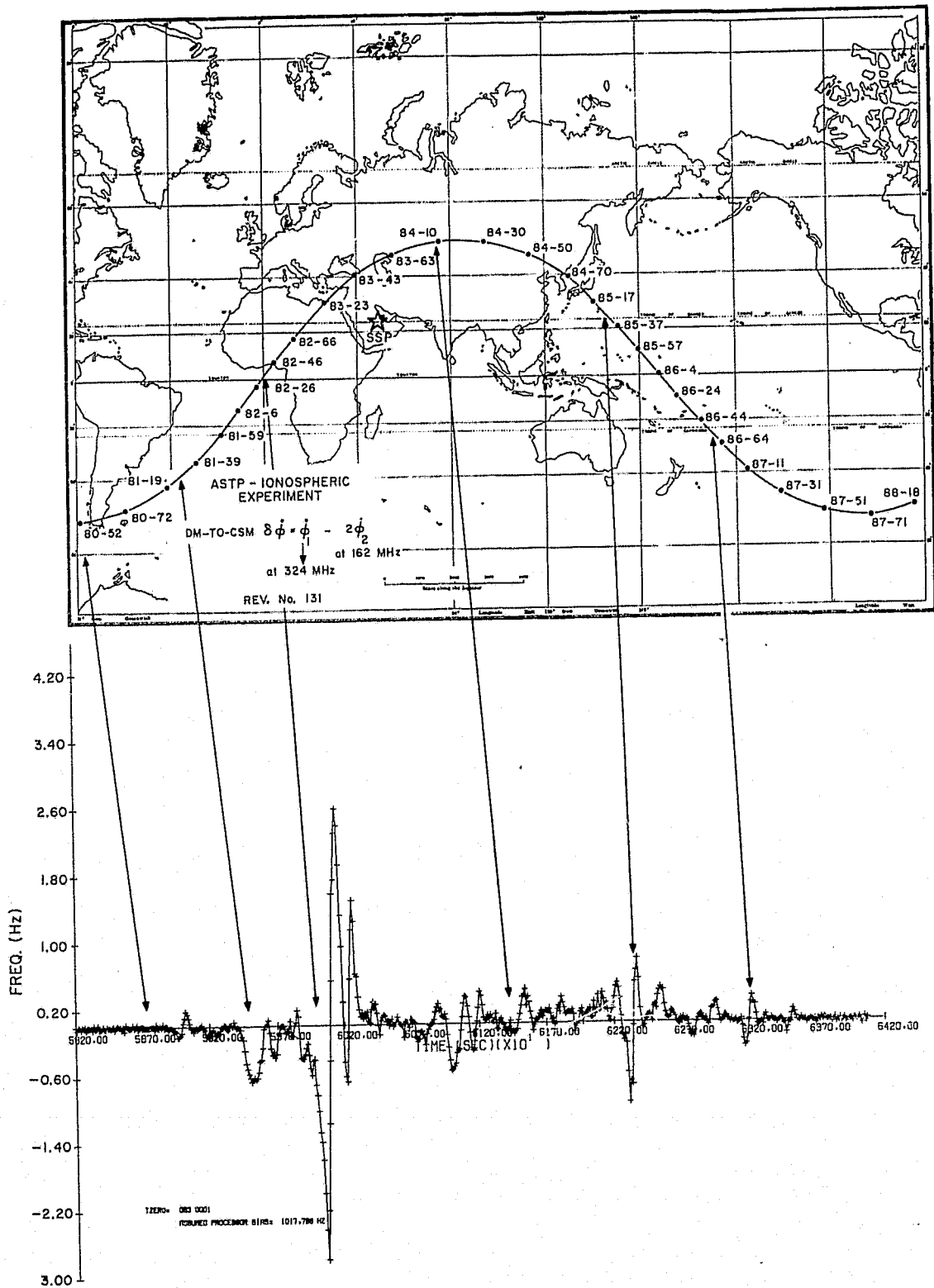Figure 30. Map of revolution 127 with differential Doppler plot.

119

Figure 31. Map of revolution 131 with differential Doppler plot.

120

Table 6. Times of data take, July 24.

Revolution number	Revolution start time (GMT)	Frame-word at meridian crossing
126	$0^h 56^m$	47-31
127	2 34	54-50
128	4 12	61-69
129	5 47	69-15
130	7 20	76-34
131	8 52	83-56
132	10 24	91-03
133	11 58	98-22
134	13 34	105-41

Apparent spatial wavelength along
the orbital track at 220-kilometer
height: ∿800 kilometers

Estimate of the spatial wavelength
as it would be observed from the
ground: 690 kilometers

Spatial extent along the orbital
track at 220-kilometer height: ∿7200 kilometers

Estimate of peak-to-peak electron-
density perturbation: 35%

Estimate of velocity: ∿700 m/sec

Estimate of the period as it would
be observed from the ground: 16 minutes

The ionospheric experiment on board the ASTP performed the first spacecraft-to-spacecraft horizontal sounding of the ionosphere at a height of 220 kilometers and acquired data that are expected to add new and useful information to the literature on ionospheric electron-density structures at a height that is important and that had never been probed before.

Data analysis still continues at this time, both for the data collected with the DM-to-CSM link and for the space-to-ground data collected by the ground-based network of stations that participated in the experiment.

In addition, it is expected that the experiment will contribute to a better understanding of how horizontal gradients of electron density influence the accuracy of ionospheric columnar measurements performed by transmitting radio emissions from satellites to the Earth.

6.3 Results from the Gravimetric Experiment

Among the effects controlling the satellite-to-satellite relative velocity are local variations in gravity. The MA-089 experiment was designed to detect anomalous gravity, i.e., those gravity-field variations with wavelengths between 250 and 1000 kilometers. The observed Doppler shift, or velocity difference, also contains other large variations due to the gross relative orbital motion and to the relative motion of the transmitting and receiving antennas with respect to the centers of mass of the CSM and the DM. Additional contributors to the observed relative velocity are the radiation patterns of the antennas and other accelerations on the vehicles, such as air drag, radiation pressure, and astronaut motion. As the analysis proceeded, each of these effects was eliminated, leaving a cleaned Doppler signal that was free of all extraneous effects and contained the Doppler shift due to anomalous gravity.

6.3.1 Estimated gravity signal

In Section 2.2, general considerations were used to estimate the gravity signal we expected to detect with the MA-089 experiment. More detailed simulations were carried out during the data-analysis phase of the experiment, in

which we used the actual satellite configuration and physical characteristics, such as the area-to-mass ratio, and environmental factors, such as the atmospheric density. From these simulations, for example, for a satellite spacing of 310 kilometers, a satellite height of 210 kilometers, and a gravity anomaly of 100 milligals in a 100-kilometer by 100-kilometer block, we should be able to obtain a peak-to-peak variation of 1.00 mm/sec as the satellite pair flew directly over an anomaly. Such anomalies are common: 69 anomalies greater than 150 milligals have been observed in terrestrial data and 14 100-kilometer by 100-kilometer anomalies greater than 200 milligals have been found. For a 300-kilometer by 300-kilometer 100-milligal anomaly, the peak-to-peak variation would be 7.05 mm/sec; no anomalies of this size and magnitude have been observed. Although detailed calculation of the peak-to-peak variation in velocity requires use of numerical-integration programs, it can be approximated by

$$\Delta v \propto \frac{L^2}{2} \overline{\Delta g_0} \frac{x \; \Delta x}{r^3} \qquad ,$$

where L is the half-width of the mean gravity anomaly $\overline{\Delta g_0}$, x is the down-track distance, r is the distance of the midpoint of the two satellites from the anomaly, and Δx is the spacing of the spacecraft. Therefore, the signal is roughly proportional to the gravity anomaly and the spacecraft spacing and is proportional to the square of the anomaly size.

The above estimate is a measure of the effect of a single gravity anomaly. Because experiment MA-089 was sensitive to many anomalies, a granularity was produced in the observed Doppler signal. The root mean square of this granularity

was calculated for a number of orbital tracks from a fine-grained gravity model based on the observed 1° by 1° anomalies. The additional short-wavelength signal has an rms of 2.1 mm/sec.

6.3.2 Error budget

When the 11,000-second duration of data take (while the CSM and the DM were still connected) was adopted as the integration time, we found an rms level of noise of 2.26 mm/sec. When an integration time of 10 to 100 seconds was used, we got a noise level of 1.8 mm/sec. This is consistent with the expected behavior of the oscillator at the two integration times considered. The Fourier transform of the 11,000-second-long sample has little structure, with a mild maximum near 300 seconds. A typical subsection of the data, with a minimum-to-maximum excursion of 12 mm/sec, is shown in Figure 32. Since the signal strength during this data-take interval was very large, the noise levels indicated above can be interpreted as oscillator stability.

A worst-case signal-to-noise ratio for the data with the CSM antenna mis-aligned by 35° with respect to the DM and with no multipath is as follows:

Separation	162 MHz	324 MHz
350 kilometers	37 decibels	31 decibels
500 kilometers	33 decibels	27 decibels

System design required as a minimum a 22-decibel signal-to-noise ratio. For a worst-case 500-kilometer separation, the contribution is 2.32 mm/sec.
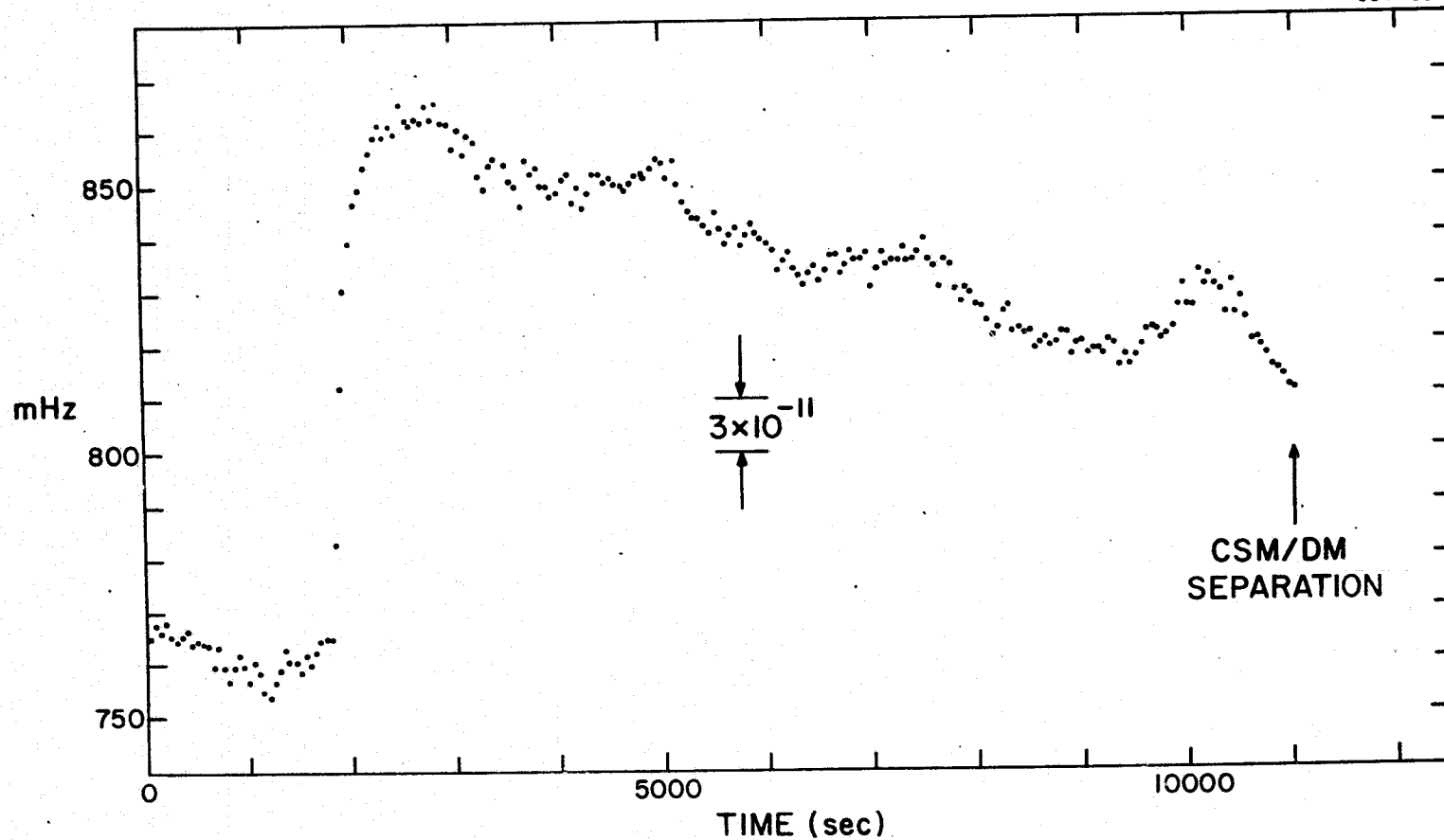
Figure 32. Initial 11,000 seconds of 324-megahertz Doppler data. Vertical scale shows the output of the receiver Doppler processor with a 1020-hertz instrument bias subtracted.

The multipath effects are variegated; first of all, they influence the signal-to-noise ratio as follows:

Separation	162 MHz	324 MHz
350 kilometers	29 decibels	23 decibels
500 kilometers	23 decibels	17 decibels

In addition, there is a multipath-induced error due to the erratic behavior of a phase-lock loop if several carriers are present within its bandwidth. Multipath, if present, would boost the total error to 3.50 mm/sec. However, multipath can occur only over the ocean, which is a good reflecting surface for VHF frequencies. No discernible difference appeared between the noise level over land and that over oceans, so multipath was ruled out.

Therefore, with an expected signal of 2.1 mm/sec for a 100-milligal anomaly and an expected noise of 2.32 mm/sec, we have a (signal + noise)/noise ratio of only 1.26 in a 100-second integration time. Consequently, the MA-089 experiment can be expected to reveal reliably only gravity signatures larger than 100 milligals, and those are, unfortunately, not expected to be numerous.

6.3.3 Data analysis

The Doppler signal observed after ionospheric effects had been removed is given in Figure 22. The data spanned 48,910 seconds with 4891 data points, and 83 individual points were eliminated. The equipment lost lock twice. The relative velocity of the two spacecraft is quite evident in the figure, demonstrating to zeroth order that the experiment obtained good data.

Data processing was done in a series of steps, detailed in Section 5. The first level subtracted the gross orbital data (Sections 5.2 and 5.3), leaving an rms Doppler signal of 1.5 m/sec, consistent with the accuracy of the orbits derived from ground tracking data. These residuals are given in Figure 33a. The long-period orbital effects were further reduced by means of polynomial smoothing, in which the orbital velocity determined from ground tracking data was used as the argument. This effectively eliminated all observable orbital effects, leaving an rms of 49 mm/sec, shown in Figure 33b.

The second level of processing removed the Doppler shift due to the rotation of the DM antenna about the center of mass and to the antenna pattern. The theory and analysis of the DM rotation is given in Section 2.4. A high-pass filter, designed to pass all frequencies in the Fourier transform with periods shorter than 400 seconds, was applied to all the data. This corresponds, roughly, to eliminating gravity signatures 3000 kilometers and longer. When the DM dynamics analysis was repeated by using unfiltered data, the same results were found. The Fourier transform of these filtered data is given in Figure 34, wherein the spectral lines associated with the DM rotation are easily identified. The width of the lines is, in part, attributable to the facts that the rotational period of the DM continually increased during data take and that the period changed discontinuously as the satellite passed from sunlight to Earth shadow.

Because of these two effects regarding the rotational period, the velocity data were analyzed in sections. The orbit was divided into 17 intervals,
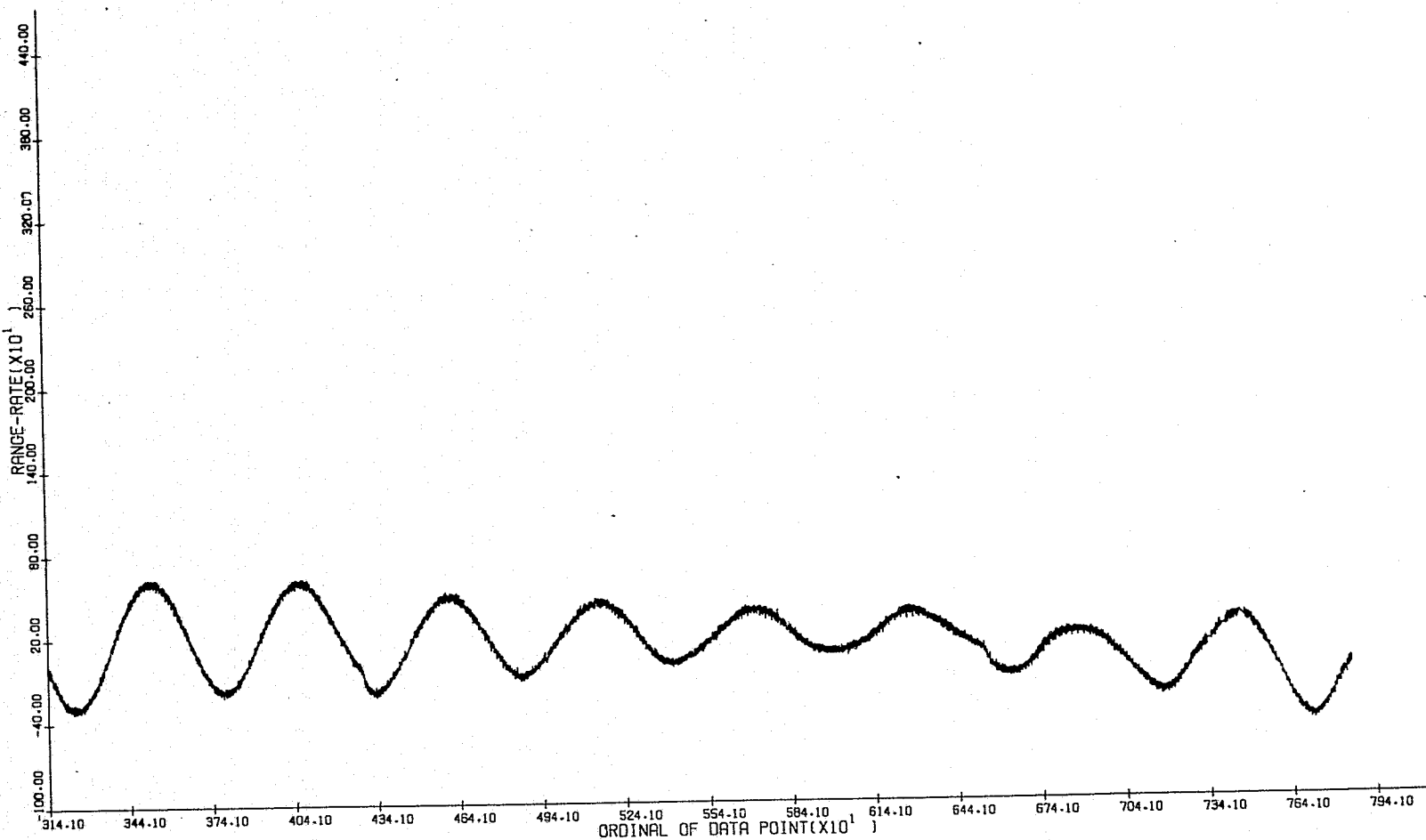
Figure 33a. Relative velocity after removal of ionospheric and orbital effects (before polynomial smoothing).
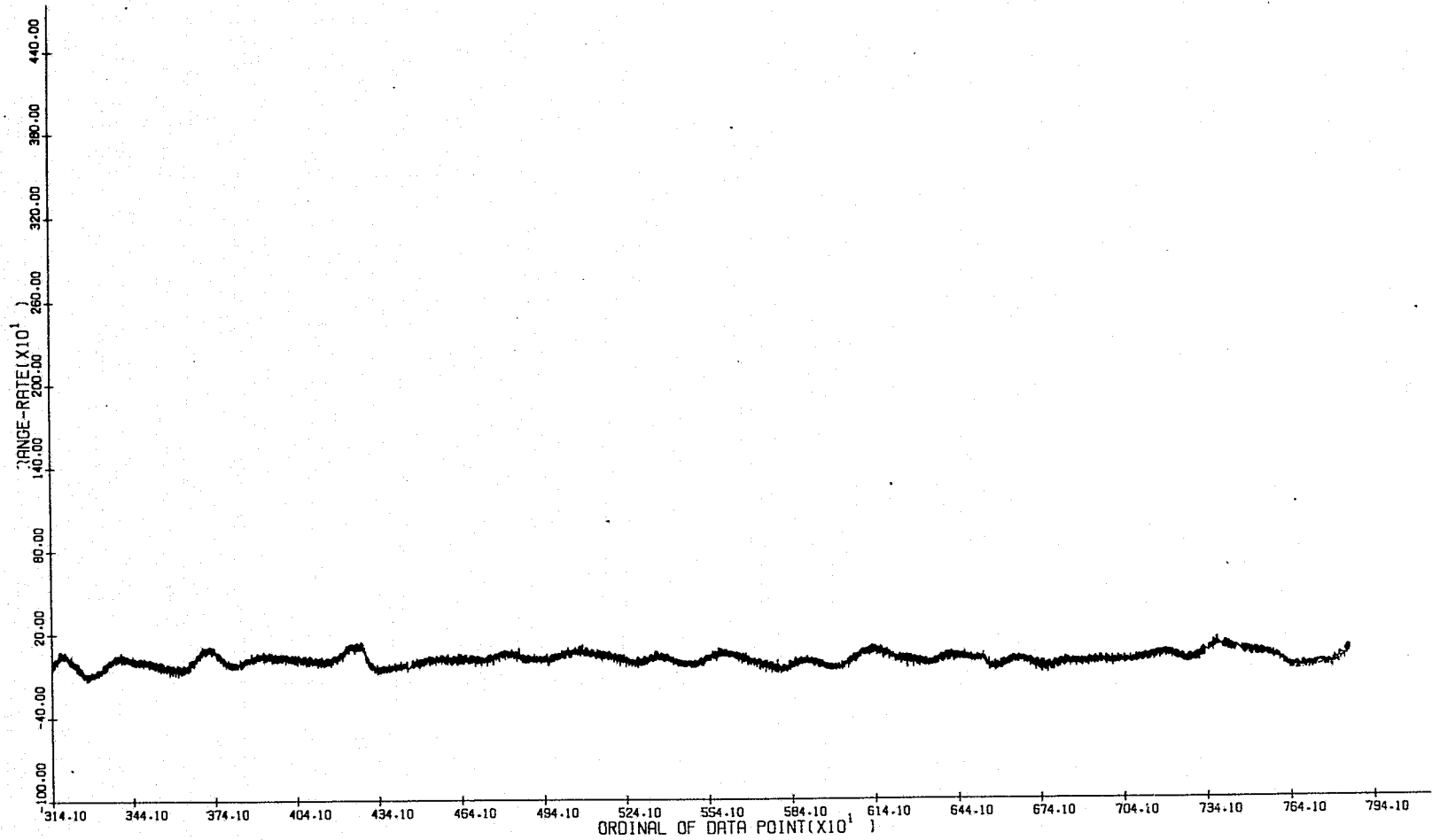
Figure 33b. Relative velocity after removal of ionospheric and orbital effects (after polynomial smoothing).
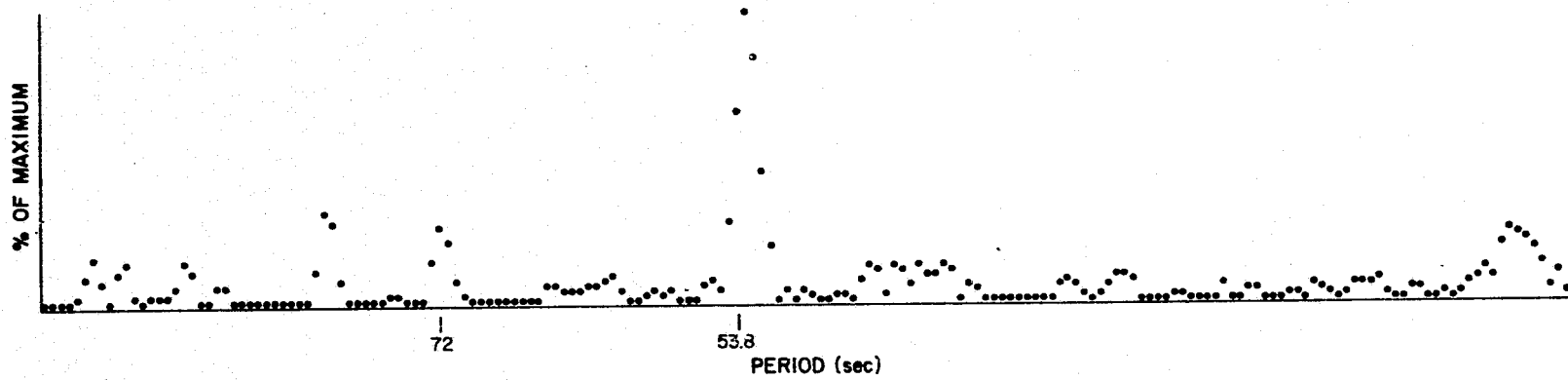
Figure 34. Fourier spectrum of smoothed data showing the effects of DM rotation.

nine of complete Sun illumination and eight of complete shadow. By using the periods and their rate of change determined by a Fourier transform of the data, we computed the periodic velocity variations and subtracted them from the data. Table 7 shows the periods of rotation for each Sun-shadow interval. Amplitudes of the components are given in Table 8. The phase of each component is not given, since it refers to an arbitrary origin. The internal consistency of the amplitudes and the periods strongly suggests that our understanding of the dynamics of the DM rotation and the antenna radiation pattern was correct. Figure 26 is a typical Fourier transform of one section of the reduced data. Table 9 also includes the rms for each subset of data, which range from 9.41 to 11.80 mm/sec.

During data take, the CSM was three-axis stabilized, rolling 360° per orbital revolution to keep the receiver antenna pointed toward the DM. A sample of rate gyro data is shown in Figure 35. Pitch and yaw were typically similar, seldom exceeding 0°05/sec. Roll remained close to 0°06/sec, the orbital rate.

Since the center of the receiving antenna was 475 millimeters from the center of gravity, measured along the longitudinal axis, a pitch rotation of 0°05/sec would result in a line-of-sight motion of the antenna of only 0.4 mm/sec. Simultaneous pitch and yaw could raise this to about 0.6 mm/sec because the antenna was close to midway between the y and z axes. Considering the small amplitude of these motions, we decided not to model them.

132

Table 7. DM rotational periods.

Time (MJD)	Interval	Period (sec)					
		53	24	72	36	109	
42617.0699	1	53.0969	23.7846	71.6027	35.9225	108.2871	Sun
.1060	2	53.2198	23.8036	71.6715	35.5003	108.3911	Shadow
.1315	3	53.3328	23.9064	71.9267	36.0955	108.7772	Sun
.1677	4	53.4834	23.9127	71.8710	35.6443	108.6928	Shadow
.1931	5	53.5451	24.0099	72.1862	36.2561	109.1696	Sun
.2293	6	53.7032	24.0420	72.0983	35.8381	109.0367	Shadow
.2548	7	53.7841	24.1026	72.3735	36.4661	109.4529	Sun
.2909	8	53.8657	24.0952	72.3468	35.9450	109.4125	Shadow
.3164	9	53.9531	24.1875	72.5618	36.5708	109.7376	Sun
.3525	10	54.0588	24.1745	72.4936	36.0693	109.6345	Shadow
.3780	11	54.1390	24.2630	73.0112	36.7885	110.4173	Sun
.4142	12	54.2479	24.2622	73.0896	36.1537	110.5358	Shadow
.4396	13	54.3513	24.3860	73.3826	36.8687	110.9790	Sun
.4758	14	54.3825	24.4080	73.0811	36.2555	110.5230	Shadow
.5012	15	54.6292	24.4638	73.5674	37.0513	111.2585	Sun
.5374	16	54.6055	24.4600	72.7246	36.5123	109.9838	Shadow
.5629	17	54.8617	24.5664	73.8443	37.1281	111.6772	Sun

133

Table 8. Amplitudes of the DM rotational components
at periods of 108, 72, 53, 36, and 24 seconds.

Time (MJD)	Interval	Amplitude (mm/sec)				
		108 sec	72 sec	53 sec	36 sec	24 sec
42617.0699	1	6.33	4.82	19.62	5.74	6.73
.1060	2	5.76	5.13	19.98	6.68	6.05
.1315	3	5.58	5.00	.19.91	5.58	7.33
.1677	4	5.50	4.19	20.59	5.39	6.58
.1931	5	5.90	5.54	18.80	5.60	7.55
.2293	6	5.62	5.14	20.16	6.14	6.58
.2548	7	6.14	5.08	18.88	5.36	7.70
.2909	8	5.38	4.72	19.73	6.47	6.81
.3164	9	5.29	5.45	19.73	5.90	8.00
.3525	10	5.24	5.38	20.63	7.24	7.85
.3780	11	5.24	5.15	19.59	5.78	8.30
.4142	12	5.00	5.20	20.96	7.39	8.75
.4396	13	5.82	5.50	20.00	6.32	6.66
.4758	14	5.20	6.26	17.93	7.41	8.23
.5012	15	4.55	6.09	18.73	5.69	6.73
.5374	16	3.98	3.15	15.84	5.13	7.10
.5629	17	5.20	6.07	17.50	8.80	8.45

Table 9. Root mean square of $\dot{\rho}$ residuals after
multiple filtering (values in mm/sec).

|	Number of filter applications				
Interval	0	1	4	6	8
1	9.41	6.03	5.26	5.11	5.01
2	10.27	6.61	6.11	6.03	5.98
3	9.56	6.05	5.15	4.98	4.86
4	11.80	9.41	9.03	8.96	8.91
5	10.09	7.17	6.38	6.16	6.01
6	10.20	6.30	5.40	5.22	5.12
7	11.27	8.38	7.65	7.46	7.34
8	10.20	5.96	5.04	4.83	4.69
9	10.03	6.29	5.41	5.21	5.08
10	9.80	5.38	4.52	4.35	4.24
11	10.15	6.49	5.57	5.37	5.24
12	9.97	5.67	4.77	4.56	4.42
13	9.99	6.99	6.07	5.86	5.72
14	9.84	5.42	4.53	4.40	4.33
15	10.13	7.54	6.43	6.08	5.85
16	9.94	8.76	7.45	7.09	6.84
17	9.73	5.90	4.92	4.74	4.64
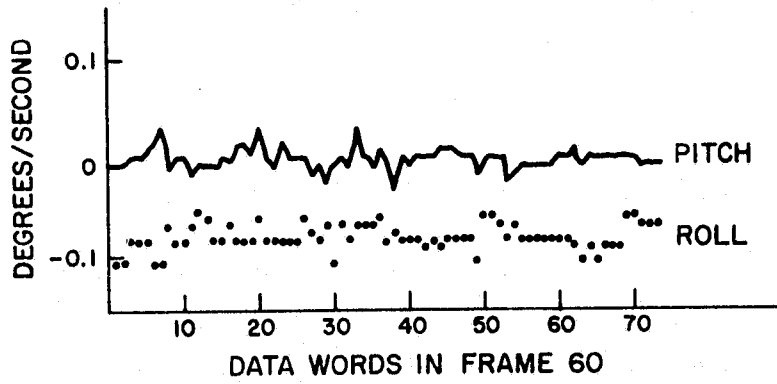
Figure 35. Pitch and roll data from frame 60.

The primary contribution from atmospheric density to the Doppler signal was at the orbital period. This information was completely removed during orbit computation, polynomial smoothing, and high-pass filtering. To contribute to the observed noise spectrum, any remaining local variations in atmospheric density would have to be of the order of the density with 100-kilometer wavelength. Gravity waves or microstructures of this magnitude and wavelength are extremely unlikely at these altitudes.

From the Fourier spectra shown in Figures 26 and 34, significant energy remains in the frequency band around 1/24 per second. This energy could be residual noise from the 24-second signal generated by the third harmonic of the DM antenna radiation pattern or aliasing of periods shorter than $1/f_n$, the reciprocal Nyquist frequency. A high-frequency signal at this level is not anticipated to be due to the Earth's gravity field. In any event, this spectral energy was eliminated.

To remove the high-frequency noise, a filter, centered on 24 seconds, was constructed to subtract periods less than 30 seconds. This filter was applied n times to give an rms approaching $(2.1^2 + 2.82^2)^{1/2} = 3.6$ mm/sec, corresponding to expectations. Table 9 shows the resulting changes in the rms scatter.

A typical time history of the filtered data is given in Figure 25, where no obvious structure that could be interpreted as a gravity signal can be seen. As a further test on the validity of the observations, a predicted Doppler shift was generated from surface-gravity observations, and a cross-correlation

function, based on a single anomaly, was calculated. The result is a cross correlation not significantly different from zero; in other words, the predicted velocity would correlate equally well with many subsets of the data.

A summary of the data analysis appears in Table 10, which gives the rms left after each step of the reduction. The noise remaining in the data is too large to draw any firm conclusion about the Earth's gravity field.

Table 10. Root mean square of the data after each analysis step.

Step	Process	rms (mm/sec)
1	Removal of gross orbital motion	48
2	High-pass filter	18
3	Removal of DM rotation	7 to 12[*]
4	Low pass filter (4 applications)	3.6
	Anticipated value	3.6

[*]After step 3, the noise level was too high for any signal to be seen. Presumably step 4, in addition to eliminating the high-frequency noise, also removed too much of the desired signal.

7. CONCLUSIONS

The Doppler Tracking Experiment MA-089 had two goals: 1) to perform a feasibility test of the low-low satellite-to-satellite method as a scheme capable of measuring gravity-field anomalies, and 2) to perform satellite-to-satellite horizontal sounding of the ionosphere.

The ionospheric data collected by the experiment are of excellent quality. The differential Doppler noise was as low as expected, and we performed valuable satellite-to-satellite observations, never carried out before, of wave phenomena occurring in the ionosphere at the ASTP orbital height.

The gravity data were, on the contrary, corrupted by a level of single-frequency Doppler noise higher than expected. Until now, no good explanation for this occurrence has been found, but whatever its origin, this high level of noise has thus far prevented any reliable identification of gravity-anomaly signatures in the data.

7.1 Ionospheric Experiment

The results of the experiment are as follows:

1. Changes in the columnar electron content between the two spacecraft were accurately measured. From these, horizontal gradients of electron density at the height of 220 kilometers were derived. Gradients as high as 10^6 el/m^3/m were

repeatedly observed both in the day-side ionosphere (typical density of approximately 5×10^{11} el/m^3) and in the night-side ionosphere (typical density of approximately 3×10^9 el/m^3). Most of these gradients were encountered at the equatorial crossings and are most likely related to equatorial F-layer irregularities.

2. Traveling ionospheric disturbances (TID) were detected. Most noticeable was a nine-cycle ionospheric wave found off the coast of California in revolution 127 (frame 56-14, July 23, 1975, 18:54:36 PDT), characterized by a peak-to-peak electron-density perturbation of 35%, by a wavelength of 690 kilometers (as the TID would be observed from the ground), and by a spatial extent of approximately 7200 kilometers along the ASTP orbital track.

3. Spacecraft-to-ground differential Doppler data were collected for SAO by the Defense Mapping Agency from 235 passes of the docking module, covering the entire surface of the Earth. Although the processing of the data has not yet been completed, we are confident that this part of the ASTP ionospheric experiment will contribute to the understanding of how horizontal gradients of electron density influence the accuracy of ionospheric columnar measurements performed by using radio emissions from satellites to the Earth. The results of this part of the experiment will be published in the technical literature.

7.2 Gravity Experiment

The gravity-experiment results are summarized as follows:

1. Detailed computations verified that a 100-milligal 1° by 1° gravity anomaly would give rise to a 1.00-mm/sec peak-to-peak differential velocity for the two spacecraft.

2. The satellite-to-satellite range-rate measurement was made. The equipment revealed gross orbital motion, which was verified at a 1-m/sec level with orbits determined independently from unified S-band and Doppler data. After the gross long-period effects had been eliminated with these independent orbits, the satellite-to-satellite data had an rms (signal plus noise) of 48 mm/sec.

3. The differential Doppler signal due to the motion of the CSM about its center of mass was always within 1 mm/sec, as specified.

4. The tumbling motion of the DM about its center of mass was very clearly discernible in the Doppler observations. The Fourier transform of the data is given in Figure 34. The principal periods were as follows:

Period	Phenomenon
72 seconds	spin rate around the CSM
208 seconds	period of precession
54 seconds	harmonics combination of 72- and 208-second periods
36 seconds	second harmonic of 72-second period due to the tesseral harmonics of the antenna radiation pattern
24 seconds	third harmonic of the 72-second period due to tesseral harmonics of the antenna radiation pattern

Detailed analysis of the Fourier spectra revealed a significant lengthening of the period over the lifetime of the mission and a significant change in the rotational period of the DM as it passed from shadow to sunlight and vice versa. Figure 36 is the mean period for each complete sunlight and shadow portion. The consequence of this large variation is that the phase of the motion and, to a lesser extent, the amplitude are not preserved throughout the mission, requiring analysis of each orbital segment separately.

5. Once the periodic motions were removed, the total system noise was found to be between 9.41 and 11.80 mm/sec for each subset taken separately.

6. The Doppler residuals for a sample of the data set are given in Figure 25. The remaining noise level, both from a scan of the figure and from the Fourier statistics, precludes an unambiguous detection of specific gravity anomalies. This is true for filtered and smoothed data as well.

7. One candidate for the high noise level is the degradation of the satellite oscillator. As discussed in Section 5.2, frequency offsets were recovered from the ground tracking data. Although a relatively high rejection rate of passes did occur, the stability of the oscillator was measured to be within specification.

8. The main conclusion is that the total system noise level was too large to allow detection of gravity anomalies. As we inquired into the source of the
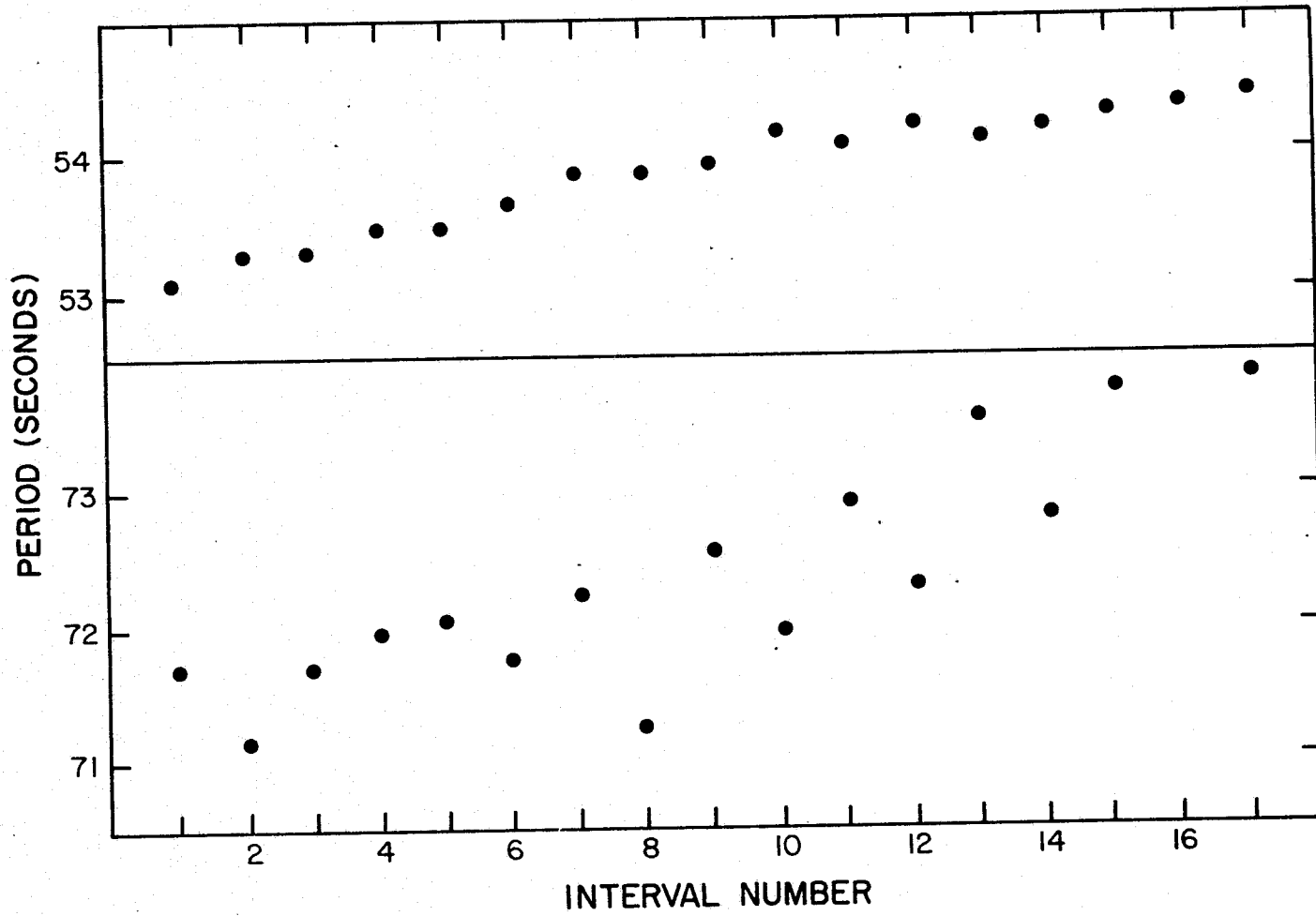
Figure 36. Mean period for each sunlight and shadow portion of the DM rotation.

noise level, no good suggestions were apparent. The Fourier spectra of the residuals revealed no significant energy density, showing only clustered broadband noise. The DM motion about its center of gravity has been completely understood, to the point of determining its physical parameters (moments of inertia, antenna position, spin rate, and antenna radiation patterns). Therefore, thus far we have been unable to identify a plausible explanation for this high noise level. What we can conclude is that, with the spatial wavelength implied by the CSM/DM separation, gravity anomalies at the ASTP orbital height produce intervehicular range rates less than 2.32 mm/sec. This undesirably high threshold sensitivity is, in part, determined by the fact that the stability of the oscillator (see Figure 7) worsens as the integration time increases beyond 100 seconds.

8. REFERENCES

1. Isacks, B.; Oliver, J.; and Sykes, L. R. : Seismology and the New Global Tectonics. J. Geophys. Res., vol. 73, 1968, pp. 5855-5899.

2. Muller, P. M.; and Sjogren, W. L.: Mascons: Lunar Mass Concentrations. Science, vol. 161, 1968, pp. 680-684.

3. Schwarz, C. R.: Gravity Field Refinement by Satellite-to-Satellite Doppler Tracking. Dept. Geodetic Sci., Ohio State Univ. Res. Found. Rep. No. 147, December 1970, 141 pp.

4. Wolf, M.: Direct Measurements of the Earth's Gravitational Potential Using a Satellite Pair. J. Geophys. Res., vol. 74, 1969, pp. 5295-5300.

5. Comfort, G. C.: Direct Mapping of Gravity Anomalies by Using Doppler Tracking Between a Satellite Pair. J. Geophys. Res., vol. 78, 1973, pp. 6845-6851.

6. Vonbun, F. O.: The ATS-F/Nimbus-E Tracking Experiment. In _Rotation of the Earth_, Proceedings of the International Astronomical Union Symposium No. 48, P. Melchior and S. Yumi, editors, Sasaki Printing and Publishing Co. (Sendai, Japan), 1972, pp. 112-120.

7. Jackson, J. E.; and Seddon, J. C.: Ionosphere Electron Density Measurements with the Navy Aerobee Hi Rocket. J. Geophys. Res., vol. 63, 1958, pp. 197-208.

8. Seddon, J. C.: Propagation Measurements in the Ionosphere with the Aid of Rockets. J. Geophys. Res., vol. 58, 1953, pp. 323-335.

9. Al'pert, Ya. L.: A Method for Investigating the Ionosphere with Artificial Satellites. Uspekhi Fiz. Nauk, vol. 64, 1958, p. 3.

10. Al'pert, Ya. L.: On the Results of Ionosphere Investigations with the Help of Coherent Radio Waves Emitted by Satellites. In _Space Research V_, D. S. King-Hele, P. Muller, and G. Righini, eds., North-Holland Publishing Co. (Amsterdam), 1965, pp. 652-686.

11. Al'pert, Ya. L.: _Radio Wave Propagation in the Ionosphere_, Vol. 1, _The Ionosphere_. 2nd ed., Consultants Bureau (New York), 1973, pp. 61-77.

12. Al'pert, Ya. L.: On Radio Methods of Ionospheric Investigations by Means of Coherent Radio Waves Emitted by Satellites. Presented at the COSPAR/URSI Symposium on Beacon Satellite Investigations of the Ionosphere Structure and ATS-6 Data, Moscow, November 1974.

13. Garriott, O. K.: The Determination of Ionospheric Electron Content and Distribution from Satellite Observations, Part 1, Theory of the Analysis. J. Geophys. Res., vol. 65, 1960, 1139-1150.

14. Garriott, O. K.: The Determination of Ionospheric Electron Content and Distribution from Satellite Observations, Part 2, Results of the Analysis. J. Geophys. Res., vol. 65, 1960, pp. 1151-1157.

15. de Mendoza, F.: Ionospheric Studies with the Differential Doppler Technique. In _Radio Astronomical and Satellite Studies of the Atmosphere_, J. Aarons, ed., North-Holland Publishing Co. (Amsterdam), 1963, pp. 289-312.

16. Misyura, V. A.; Solodovnikov, G. K.; and Migunov, V. M.: Gradients of the Integral Electron Content in the Ionosphere. Geomagn. i Aeronomiya, vol. 4, 1964, pp. 1124-1126; transl. in Geomagn. and Aeron., vol. 4, pp. 872-874.

17. Tyagy, T. R.: Determination of Total Electron Content from Differential Doppler Records. J. Atmos. Terr. Phys., vol. 36, 1974, pp. 1157-1164.

18. Grossi, M. D.; and Gay, R. H.: Doppler Measurements of the Ionosphere on the Occasion of the Apollo-Soyuz Test Project. Part I: Computer Simulation of Ionospheric-Induced Doppler Shifts. Smithsonian Astrophys. Obs. Spec. Rep. No. 366, 1975, 54 pp. plus appendix.

19. Gay, R. H.; and Grossi, M. D.: Doppler Measurements of the Ionosphere on the Occasion of the Apollo-Soyuz Test Project. Part II: Inversion of Differential and Rotating Doppler Shifts. Smithsonian Astrophys. Obs. Spec. Rep. No. 367, 1975, 37 pp.

20. King-Hele, D.: Theory of Satellite Orbits in an Atmosphere. Butterworths (London), 1964, 165 pp.

21. Gaposchkin, E. M., editor: 1973 Smithsonian Standard Earth (III). Smithsonian Astrophys. Obs. Spec. Rep. No. 353, 1973, 388 pp.

22. Grossi, M. D.: Spacecraft-to-Spacecraft Ionospheric Measurements on Occasion of the Apollo-Soyuz Test Project. In Proceedings of the Beacon Satellite Investigations of the Ionosphere Structure and ATS-6 Data, Acad. Sci. USSR (Moscow), vol. 1, 1975, pp. 84-91.

23. Gay, R. H.; and Grossi, M. D.: The Ionospheric Experiment of the Apollo-Soyuz Test Project. Presented at the American Geophysical Union Meeting, Madison, Wisconsin, September 1975.

24. Al'pert, Ya. L.: On Ionospheric Investigations by Coherent Radiowaves Emitted from Artificial Earth Satellites. Space Sci. Rev., vol. 18, 1976, pp. 551-602.

9. PUBLICATIONS RESULTING FROM THIS RESEARCH

Gay, R. H.; and Grossi, M. D.: Doppler Measurements of the Ionosphere on
the Occasion of the Apollo-Soyuz Test Project. Part II: Inversion of
Differential and Rotating Doppler Shifts. Smithsonian Astrophys. Obs.
Spec. Rep. No. 367, 1975, 37 pp.

Gay, R. H.; and Grossi, M. D.: The Ionospheric Experiment of the Apollo-
Soyuz Test Project. Presented at the American Geophysical Union Meeting,
Madison, Wisconsin, September 1975.

Gay, R. H.; and Grossi, M. D.: The Inversion of Differential and Rotating
Doppler Data Collected by the Ionospheric Experiment of the Apollo-Soyuz
Test Project. Presented at the 1975 USNC/URSI-IEEE Meeting, Boulder,
Colorado, October 1975.

Grossi, M. D.: Spacecraft-to-Spacecraft Ionospheric Measurements on Occasion
of the Apollo-Soyuz Test Project. Presented at the Conference on Beacon
Satellite Investigations of the Ionosphere Structure and ATS-6 Data,
Acad. Sci. USSR, Moscow, November 1974.

Grossi, M. D.; and Gay, R. H.: Doppler Measurements of the Ionosphere on
the Occasion of the Apollo-Soyuz Test Project. Part I: Computer Simulation
of Ionospheric-Induced Doppler Shifts. Smithsonian Astrophys. Obs. Spec.
Rep. No. 366, 1975, 54 pp. plus appendix.

Grossi, M. D.; and Gay, R. H.: Computer Simulation of the Ionospheric Experiment
of the Apollo-Soyuz Test Project. Presented at the 1975 USNC/URSI-IEEE
Meeting, Boulder, Colorado, October 1975.

Grossi, M. D.; and Gay, R. H.: Early Results of the Ionospheric Experiment
of the Apollo-Soyuz Test Project. Presented at the COSPAR Beacon Satellite
Symposium, Boston, Massachusetts, June 1976 (also available as Center for
Astrophysics Preprint No. 565).